Combustion Dynamics in Multi-Nozzle Combustors Operating on High-Hydrogen Fuels

FINAL REPORT

Performance Period: 10/01/2008 to 9/30/2013

Principal Authors: Dom Santavicca and Tim Lieuwen

Report Date: October 2014

DOE Project DE-FC26-08NT05054

Lead University: The Pennsylvania State University
University Park, PA 16802

Subcontracting University: Georgia Institute of Technology
Atlanta, GA 30332

Abstract

Actual gas turbine combustors for power generation applications employ multi-nozzle combustor configurations. Researchers at Penn State and Georgia Tech have extended previous work on the flame response in single-nozzle combustors to the more realistic case of multi-nozzle combustors. Research at Georgia Tech has shown that asymmetry of both the flow field and the acoustic forcing can have a significant effect on flame response and that such behavior is important in multi-flame configurations. As a result, the structure of the flame and its response to forcing is three-dimensional. Research at Penn State has led to the development of a three-dimensional chemiluminescence flame imaging technique that can be used to characterize the unforced (steady) and forced (unsteady) flame structure of multi-nozzle combustors. Important aspects of the flame response in multi-nozzle combustors which are being studied include flame-flame and flame-wall interactions. Research at Penn State using the recently developed three-dimensional flame imaging technique has shown that spatial variations in local flame confinement must be accounted for to accurately predict global flame response in a multi-nozzle can combustor.

Table of Contents

Executive Summary

Actual gas turbine combustors for power generation applications employ multi-nozzle combustor configurations. Researchers at Penn State and Georgia Tech have extended previous work on the flame response in single-nozzle combustors to the more realistic case of multi-nozzle combustors. Research at Georgia Tech has shown that asymmetry of both the flow field and the acoustic forcing can have a significant effect on flame response and that such behavior is important in multi-flame configurations. As a result, the structure of the flame and its response to forcing is three-dimensional. Research at Penn State has led to the development of a three-dimensional chemiluminescence flame imaging technique that can be used to characterize the unforced (steady) and forced (unsteady) flame structure of multi-nozzle combustors. The three-dimensional flame imaging technique has made it possible to study important aspects of multi-nozzle flames including flame-flame and flame-wall interactions.

From the work at Penn State it was shown that an analysis of 3-D flame images of an unforced multi-nozzle flame yielded a range of metrics that can be used to characterize aspects of the flame structure that play an important role in flame response. Around the circumference of the flame, flame length increases in the direction of swirl and does not seem to depend on confinement indicating that the swirling flow field in the combustor affects the flame structure in addition to confinement. Using known information of the location of flow structures with respect to the flame position, approximate locations of shear layers and outer recirculation zones can be determined. The area of the outer recirculation zone shows an inverse dependence on confinement i.e. the smallest outer recirculation zone is observed at highest confinement case.

The global flame transfer function data of the multi-nozzle flame is qualitatively similar to that observed in single-nozzle combustors employing the same injector. Flame transfer functions of isolated 3-D regions show out of phase behavior between regions at gain minimum conditions. This indicates that destructive interference between fluctuations in these regions leads to reduced flame transfer function gain. Isolating 2-D image slices of the outer half of a single outer flame shows that the frequency of minimum gain of each image slice is dependent on confinement i.e. the highest gain minimum frequency occurred at the highest confienement ratio case. Furthermore, the flame transfer function data cannot be generalized with Strouhal number, indicating that more than one convective mechanism is responsible for the response of the mult-nozzle flame.

The spatially-resolved heat release rate fluctuations in the forced flame images can be identified by obtaining RMS magnitude and phase images at each forcing frequency. The RMS magnitude images show that the regions of highest heat release rate fluctuation do not correspond to the center of heat release which indicates that analyses based on a single point metric that describes flame structure (such as flame length) may be inaccurate as they do not capture the regions of highest heat release rate fluctuation. The phase images show a variation in phase within the flame brush indicating that instead of the flame responding in bulk, a shorter wavelength convective disturbance propagating along the flame sheet produces local oscillations in heat release rate.

The variation of mean flame position of the flame slices of the outer half of a single outer flame in the forced flame case was investigated. The results showed that the maximum fluctuation of the flame base occurs at the gain minimum frequency which is consistent with previous research. In addition, there is a noticeable decrease in the magnitude of the fluctuation of the mean flame position as the confinement increases.

The work done at Georgia Tech has yielded some important and significant results regarding the dynamics of harmonically forced premixed flames. A key finding from this work was that helical modes influence the flame transfer function of axisymmetric and non-axisymmetric mean flames differently. In the case of axisymmetric mean flames, only the axisymmetric contribution of the flame wrinkling behavior contributes to the global fluctuating area. This implies that even if the dominant wrinkling flame response mode is non-axisymmetric, it does not contribute to the global unsteady heat release of axisymmetric flames. Thus significantly different sensitivities may be observed in single and multi-nozzle flames in otherwise identical hardware, due to the near axisymmetry in one case and the strong non-axisymmetry in the other.

In order to answer this question, analytical results were derived for weak asymmetries and a numerical solver was used for strong asymmetries in the mean flame/flow. Two example cases were considered: (i) Elliptic cross-section and (ii) Square cross-section. In both these cases, results showed that for a linear analysis, the asymmetry modes in the mean flame/flow interact with the same but opposite modes in the flow disturbance to lead to a finite global flame response. This effect is compounded especially when non-compact flames are considered, wherein, the global unsteady heat release is not considered. In this case, the Rayleigh criterion requires the local unsteady heat release to be multiplied with the local unsteady pressure before the Rayleigh Index is calculated.

In addition, the slope of the regression line between consumption and displacement speed was determined, which allows us to relate the turbulent displacement speed directly to the consumption speed. This allows us to determine the computational, ensemble averaged heat release. This may then be extended to determine a computational flame transfer function. It was determined that a correction factor was necessary to account for the fact that the flame tip moves periodically. In systems where the flame position function is not oriented parallel to the wall, this flame movement causes the limit of integration to change when determining the spatially integrated heat release. Whereas, in systems with the flame position function oriented parallel to the wall, and normal to the direction of integration, integration to the wall accounts for flame tip fluctuations. One key result is the significance of the integration limit when evaluating global flame transfer function's – very different answers are obtained for different assumptions on the integration surface.

Regarding the dynamics of harmonically forced premixed flames and their vortex breakdown bubble flow dynamics, a theoretical model was proposed to explain the interesting behavior and difference between the instantaneous and time averaged stagnation point behavior.

Lastly, work was presented on velocity field measurements and analysis for a transversely forced, swirl stabilized combustor. The analysis compared single nozzle and multi-nozzle configurations. Previous studies of multiple jet flows indicate that neighboring jets experience a mutual interaction, upstream of the direct shear layer interaction, which can alter both the time averaged and dynamical flowfields. Therefore, this experimental study has probed the velocity field near the dump plane to see if such mutual interactions exist. Results show minor differences in the time averaged flows when switching from single nozzle to multi-nozzle flows. The most notable difference is a non-axisymmetric elongation of the jet cross section. The major axis of the elongation "tilts" to align itself away from the nearby combustor walls and nozzles. The direction of this tilting appears to be prescribed by the swirl direction of the neighboring nozzles.

Milestone Status Report

Task/ Subtask #	Project Milestone Description	Project Duration - Start: 10-1-2008 End: 9-30-2013																				Planned Start Date:	Planned End Date:	Actual Start Date:	Actual End Date:	Comments
		Proj Yr (PY) 1				PY2				PY3				PY4				PY5				Quarter				
		Q 1	Q 2	Q 3	Q 4	Q 5	Q 6	Q 7	Q 8	Q 9	Q 10	Q 11	Q 12	Q 13	Q 14	Q 15	Q 16	Q 17	Q 18	Q 19	Q 20					
2.1	Design and fabricate SS nozzle.	x	x																			1	2	1	1	Completed
3.1	Design multi-nozzle test rig with transverse forcing.	x																				1	1	1	1	Completed
3.2	Fabricate and construct multi-nozzle test rig with transverse forcing.	x																				1	1	1	1	Completed
3.3	Transverse forced response tests with SS nozzle.		x	x	x	x																2	5	2	5	Completed
4.1	Design multi-nozzle test rig with longitudinal forcing.	x	x	x																		1	2	1	3	Completed
4.2	Fabricate and construct multi-nozzle test rig with longitudinal forcing.		x	x	x	x	x	x														2	4	2	7	Completed
4.3	Longitudinal forced response tests with SS nozzle.								x	x	x	x										4	7	8	11	Completed
5.1	Formulate flame response model for transverse forcing.			x	x	x	x	x	x													3	8	4	9	Completed
5.2	Compare transverse flame response model predictions to single- and multi-nozzle measurements.									x	x	x										9	11	9	12	Completed
6.1	Formulate flame response model for longitudinal forcing.		x	x	x	x																2	5	2	5	Completed
6.2	Compare longitudinal flame response model predictions to single- and multi-nozzle measurements.						x	x	x	x												6	9	6	9	Completed

Milestone Status Report (continued)

Task/ Subtask #	Project Milestone Description	Project Duration - Start: 10-1-2008 End: 9-30-2013																				Planned Start Date:	Planned End Date:	Actual Start Date:	Actual End Date:	Comments
		Proj Yr (PY) 1				PY2				PY3				PY4				PY5								
		Q 1	Q 2	Q 3	Q 4	Q 5	Q 6	Q 7	Q 8	Q 9	Q 10	Q 11	Q 12	Q 13	Q 14	Q 15	Q 16	Q 17	Q 18	Q 19	Q 20	Quarter				
7.1	Implement high speed intensified camera for phase-synchronized 3-D chemiluminescence imaging													x	x							13	14	13	14	Completed
7.2	Develop improved software for processing and display of 3-D chemiluminescence data													x	x	x						13	15	13	15	Completed
8.1	Use phase-synchronized 3-D chemiluminescence flame images to differentiate between the velocity-forced flame response of the center flame, the outer flames and the interaction region.															x	x	x	x			15	18	15	20	Completed
8.2	Investigate methodologies for using single-nozzle flame transfer function data to predict multi-nozzle flame transfer function.																x	x	x	x		16	20	16	20	Completed
8.3	Use phase-synchronized 3-D chemiluminescence flame images to investigate the sensitivity of the overall flame response to nozzle-to-nozzle differences, for example equivalence ratio.																		x	x	x	18	20	18	20	Completed

Milestone Status Report (continued)

Task/ Subtask #	Project Milestone Description	Project Duration - Start: 10-1-2008 End: 9-30-2013																				Planned Start Date:	Planned End Date:	Actual Start Date:	Actual End Date:	Comments
		Proj Yr (PY) 1				PY2				PY3				PY4				PY5				Quarter				
		Q 1	Q 2	Q 3	Q 4	Q 5	Q 6	Q 7	Q 8	Q 9	Q 10	Q 11	Q 12	Q 13	Q 14	Q 15	Q 16	Q 17	Q 18	Q 19	Q 20					
9.1	Extend current models of flame response to axisymmeteric disturbances to include flame excitation by helical disturbances which are excited during transverse instabilities.										x	x	x	x	x							9	12	10	14	Completed
9.2	Develop models of stagnation point stabilized flames to velocity forcing.											x	x	x	x	x						11	15	11	15	Completed
10.1	Analyze radial slices from high-speed PIV images to determine azimuthal modes excited by transverse forcing.			x	x	x	x	x	x													3	8	3	8	Completed
10.2	Relate azimuthal modes excited by flow forcing to hydrodynamic flow stability theory of swirling jets.									x	x	x	x									8	11	9	12	Completed
11.1	Perform simultaneous 10 kHz PIV and OH PLIF imaging of transversely forced flames.		x	x	x	x																2	5	2	5	Completed
11.2	Extend forced analysis to traveling wave configurations to generalize current understanding obtained from velocity node and velocity anti-node forcing.						x	x	x	x												5	8	6	9	Completed
12.1	Submit Quarterly Report	x	x	x	x	x	x	x	x	x	x	x	x	x	x	x	x	x	x	x	x	1	20	1	20	Completed
12.2	Submit Annual Report				x				x				x				x				x	4	20	5	20	Completed
12.3	Submit Final Report																				x	19	20	19	20	Completed

Cost Plan/Status

Baseline Reporting Quarter		Year 1 Start: 10/1/2008 End: 9/30/2009				Year 2 Start: 10/1/2009 End: 9/30/2010				Year 3 Start: 10/1/2010 End: 9/30/2011				Year 4 Start: 10/1/2011 End: 9/30/2012				Year 5 Start: 10/1/2012 End: 9/30/2013				Total
		Q1	Q2	Q3	Q4	Q1	Q2	Q3	Q4	Q1	Q2	Q3	Q4	Q1	Q2	Q3	Q4	Q1	Q2	Q3	Q4	
Baseline Cost Plan (from SF-424A)	Federal Share	$34,305	$34,305	$34,305	$34,305	$33,336	$33,336	$33,336	$33,336	$32,359	$32,359	$32,359	$32,359	$42,349	$42,349	$42,349	$42,349	$32,651	$32,651	$32,651	$32,651	$700,000
	Non-Federal Share	$17,675	$17,675	$17,675	$17,675	$4,925	$4,925	$4,925	$4,925	$2,401	$2,401	$2,401	$2,401	$34,375	$34,375	$34,375	$34,375	$31,250	$31,250	$31,250	$31,250	$362,500
	Total Planned (Federal and Non-Federal)	$51,980	$51,980	$51,980	$51,980	$38,260	$38,260	$38,260	$38,260	$34,760	$34,760	$34,760	$34,760	$76,724	$76,724	$76,724	$76,724	$63,901	$63,901	$63,901	$63,901	$1,062,500
	Cumulative Baseline Costs	$51,980	$51,980	$51,980	$51,980	$38,260	$38,260	$38,260	$38,260	$34,760	$34,760	$34,760	$34,760	$76,724	$76,724	$76,724	$76,724	$63,901	$63,901	$63,901	$63,901	$1,062,500
Actual Incurred Costs	Federal Share	$14,993	$78,040	$54,330	$5,330	$6,756	$0	$41,813	$27,769	$29,552	$26,342	$9,626	$8,282	$22,400	$20,443	$22,242	$48,940	$14,505	$63,188	$60,546	$144,903	$700,000
	Non-Federal Share	$1,876	$9,764	$25,201	$1,332	$1,689	$0	$10,453	$6,942	$7,388	$6,586	$2,407	$2,071	$5,600	$5,111	$5,561	$12,235	$3,626	$20,007	$76,816	$157,836	$362,500
	Total Incurred Costs-Quarterly (Federal and Non-Federal)	$16,869	$87,804	$79,531	$6,662	$8,445	$0	$52,266	$34,712	$36,940	$32,928	$12,033	$10,353	$28,000	$25,554	$27,803	$61,175	$18,131	$83,195	$137,362	$302,739	$1,062,500
	Cumulative Incurred Costs	$16,869	$87,804	$79,531	$6,662	$8,445	$0	$52,266	$34,712	$36,940	$32,928	$12,033	$10,353	$28,000	$25,554	$27,803	$61,175	$18,131	$83,195	$137,362	$302,739	$1,062,500
Variance	Federal Share	$19,312	-$43,735	-$20,025	$28,975	$26,580	$33,336	-$8,477	$5,566	$2,808	$6,017	$22,733	$24,077	$19,949	$21,906	$20,107	-$6,591	$18,146	-$30,537	-$27,895	-$112,252	$0
	Non-Federal Share	$15,799	$7,911	-$7,527	$16,342	$3,235	$4,925	-$5,529	-$2,018	-$4,987	-$4,185	-$6	$331	$28,775	$29,264	$28,814	$22,140	$27,624	$11,243	-$45,566	-$126,586	$0
	Total Variance-Quarterly (Federal and Non-Federal)	$35,111	-$35,825	-$27,552	$45,318	$29,815	$38,260	-$14,006	$3,549	-$2,179	$1,832	$22,727	$24,408	$48,724	$51,170	$48,921	$15,549	$45,770	-$19,294	-$73,461	-$238,838	$0
	Cumulative Variance	$35,111	-$35,825	-$27,552	$45,318	$29,815	$38,260	-$14,006	$3,549	-$2,179	$1,832	$22,727	$24,408	$48,724	$51,170	$48,921	$15,549	$45,770	-$19,294	-$73,461	-$238,838	$0

Technical Details – The Pennsylvania State University

1.0 Introduction

1.1. Gas Turbine Engines and Combustors

In 1939, the world's first successful electric power generating gas turbine engine went into operation in the municipal power station in Neuchâtel, Switzerland. It comprised a 23 stage axial compressor, a single can combustor, a 7 stage axial turbine and a generator that synchronously operated on the same shaft and had a power output of 4 MW at an efficiency of 17.4% [4]. Since then, gas turbine technology has made immense progress and modern engines have power outputs upwards of 200 MW with efficiencies higher than 30% [5]. Today, gas turbine engines are one of the most widely used technologies for power generation.

A component that has been the subject of significant research and development effort in the gas turbine community is the combustor which must satisfy a wide range of requirements including: high combustion efficiency, wide flame stability ranges, low pressure loss, outlet temperature distributions tailored to maximize the lives of downstream components, low emissions of smoke and pollutant species, durability, maintainability and avoidance of combustion instabilities [1]. Early combustors employed diffusion flame combustion where the fuel and air enter the combustor in an unmixed state. Mixing and combustion take place simultaneously in the reaction zone. Combustion occurs at near-stoichiometric fuel-air ratios at high temperatures. While higher combustion temperature increases performance, it promotes the formation of thermal NO_x. Increasingly stringent regulations to reduce NO_x emissions led to the development of lean premixed (LPM) combustors. Here, fuel and air is mixed upstream of the combustion chamber and combustion takes place at fuel lean conditions. Combustion occurs at lower temperatures and the NO_x concentration in the exhaust of LPM combustors is typically less than 25 ppmv (parts per million by volume) [5]. While LPM combustors successfully reduce the formation of thermal NO_x, they face a serious drawback in that they are susceptible to combustion instabilities. This is due to two main reasons: First, operating at lean conditions increases the system's susceptibility to instabilities because of its closer proximity to the lean blowout limit [7]. Second, a substantial amount of air enters through the combustor liner in diffusion combustors which serves to damp pressure oscillations in the combustor as well as reduce the temperature of the combustion products entering the turbine section. Lean-premixed combustors have lower combustion temperatures and therefore do not use nearly as much dilution air and therefore have much less acoustic damping [8].

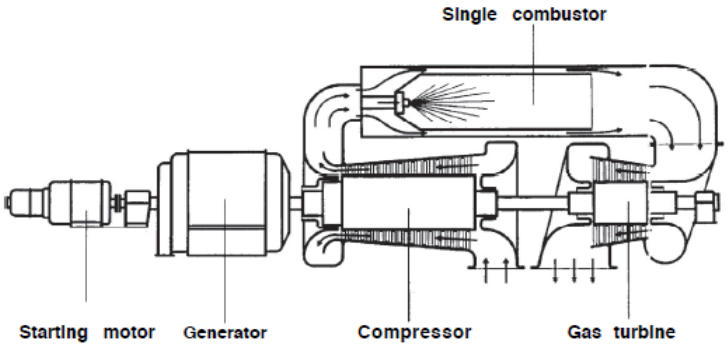

Figure 1.1. Neuchâtel gas turbine engine [4].

1.2. Flow Field and Flame Structure in Swirl Stabilized Combustors

An important requirement of a gas turbine combustor is to maintain flame stability at a wide range of operating conditions. In a combustion system, a stable flame is one that is anchored at a desired location and is resistant to blowoff, flashback and liftoff over the operating range of the combustor. A flame is locally stabilized when the local flame speed matches the local mean velocity [9]. These local flame stabilization locations (which depend on the flow field in the combustor) govern flame structure.

In lean premixed gas turbine engines, a common practice is to use a bluff centerbody and an induced swirl component of the incoming air-fuel mixture to aid in flame stabilization. Swirl can be induced in the flow using either an axial or radial type swirler. Both swirler geometries produce high levels of turbulence and enhanced mixing rates. The nozzles used in the multi-nozzle can combustor in this study have axial type swirlers.

Figure 1.1. Two main types of swirlers [1]

When the amount of swirl induced in the flow exceeds a critical value, a recirculation zone is formed in the core region. The size and shape of this recirculation zone is dependent on the swirler geometry [10]. Beer and Chigier [11] introduced a metric to characterize the amount of rotation imparted to an axial flow. The swirl number (S) is defined as the ratio of the axial flux of the tangential momentum to the product of the axial momentum flux and a characteristic radius. Here, u is the axial velocity component, v is the tangential velocity component and R is the nozzle radius.

$$S = \frac{\int_0^R \rho u v 2\pi r^2 dr}{R \int_0^R \rho u^2 2\pi r^2 dr} \tag{1.1}$$

For axial swirlers with flat vanes, a swirl number based on geometry can be defined (assuming uniform velocities and thin vanes). Here, R_n is the nozzle radius, R_h is the centerbody radius and ϕ is the swirl vane angle.

$$S = \frac{2}{3}\left[\frac{1 - (R_h/R_n)^3}{1 - (R_h/R_n)^2}\right]\tan\varphi \tag{1.2}$$

When the swirl number exceeds a critical value, flow recirculation is achieved [12]. The recirculating flow transports hot combustion products back to mix with the incoming flow of reactants. This establishes a mechanism of continuous ignition of the fresh gases and results in a stable, compact flame over a wide range of conditions. As the swirl is increased, the recirculation vortex becomes stronger, which leads to enhanced mixing of reactants and as a result, the flame becomes shorter.

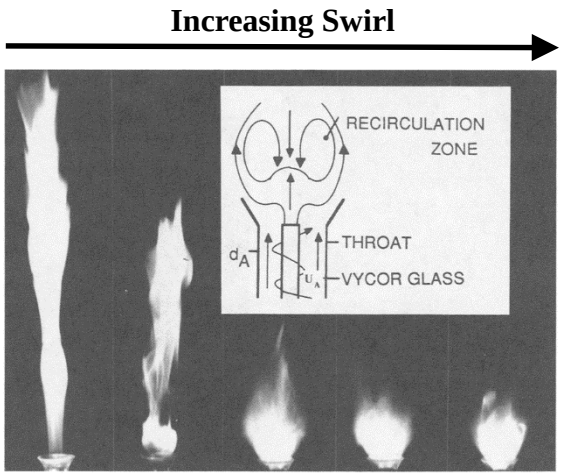

Figure 1.2. Effect of increasing swirl on flame structure [11]

Flow field measurements and simulations of swirling flows with a centerbody [13], a common geometry for commercial low NO_x combustor hardware [1] have identified four main fluid mechanic features (Figure 1.3):

(1) An outer recirculation zone (ORZ)
(2) An inner recirculation zone (IRZ or vortex breakdown bubble)
(3) A high velocity, annular fluid jet that divides these regions
(4) Two annular shear layers that divide the ORZ and annular jet (outer shear layer, OSL) and the IRZ and annular jet (inner shear layer, ISL).

The outer recirculation zone (ORZ) is a toroidal recirculating regime generated by a rapid expansion of the nozzle into the combustor. It acts to recirculate hot combustion products to the root of the flame. The size and shape of the ORZ depends on inlet flow conditions (Reynolds number and Swirl number) and the confinement by the walls. The length of the ORZ is shorter for high swirl-number cases because of the stronger expansion of the main flow resulting from the higher centrifugal force. The ORZ is less efficient for flame stabilization purposes due to high rates of heat transfer to the walls and therefore, the inner recirculation zone is of greater interest to combustion engineers as a flame stabilization mechanism [14].

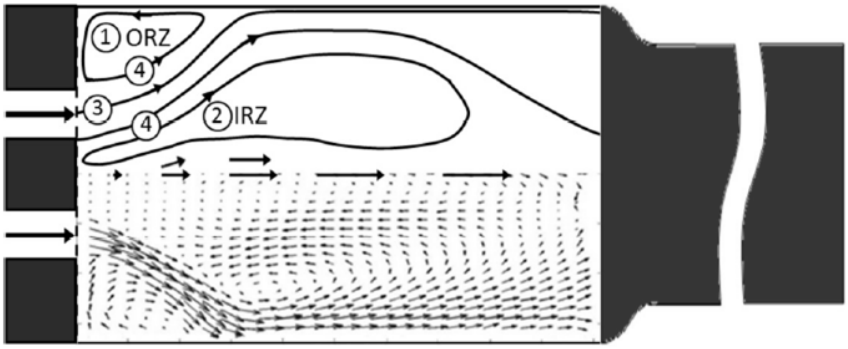

Figure 1.3. Time averaged fluid mechanic features in swirling flows with a centerbody [12]

The inner recirculation zone (IRZ) is a toroidal recirculation zone generated due to vortex breakdown accompanying the swirling flow and the bluff body wake. The formation of a toroidal vortex-type recirculation zones in the central region of swirling jets have been extensively investigated. Comprehensive reviews on this subject are presented by Syred & Beer [14], Lucca-Negro & O'Doherty [15], and Huang & Yang [16]. As the swirl of the inlet flow is increased, a strong azimuthal flow component is induced. This creates a strong pressure gradient in the radial direction to balance the centrifugal force due to the azimuthal flow.

$$\frac{\partial p}{\partial r} = \frac{\rho U_\theta^2}{r} \tag{1.3}$$

As the flow propagates downstream, it rapidly expands and the azimuthal velocity decays. This causes an abrupt change in flow structure known as vortex breakdown [15, 17]. At this downstream location, the pressure is recovered i.e. the radial pressure gradient is minimum. This creates a positive (adverse) pressure gradient along the central axis and flow recirculation occurs (Figure 1.4). Sarpkaya [18] observed three types of vortex breakdown: bubble, spiral and double helix. The structure and location of vortex breakdown was shown to depend on the type of vortex tube used and the Reynolds and circulation (swirl) numbers of the flow. For high swirl number turbulent flows observed in most practical gas turbine combustors, the vortex breakdown is of a bubble type.

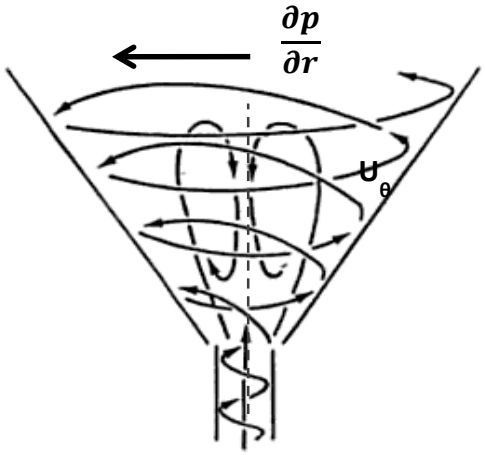

Figure 1.4. Formation of vortex breakdown bubble (modified from Lefebvre and Ballal [4])

The bluff centerbody also introduces a wake flow. For small centerbody diameters and/or weak swirl, the centerbody wake closes upstream of the upstream stagnation point of the vortex breakdown region, and thus two distinct flow structures (centerbody wake and vortex breakdown bubble) are observed. For larger centerbodies (and/or strong swirl), the wake and vortex breakdown bubble merge into a single, interacting structure [19] as illustrated in Figure 1.5. The existence of distinct or merged IRZ structure has also been shown to depend on swirl number [20] as well as Reynolds number and exhaust contraction ratio [21].

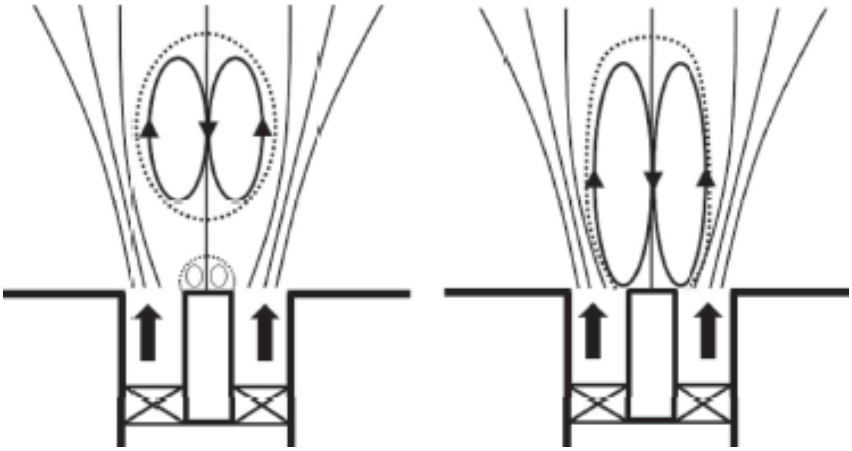

Figure 1.5. Effect of centerbody wake on inner recirculation zone [18]

Two shear layers develop from the injector exit due to the velocity difference between the jet flow and the flow in the recirculation zones: an outer shear layer (OSL) that originates from the nozzle edge and an inner shear layer (ISL) that originates from the centerbody edge. . The unsteady nature of these shear layers allow large-scale coherent structures to be generated and shed downstream sequentially due to Kelvin–Helmholtz (K–H) instabilities. These vortical structures influence the combustion process by modulating the mixing among fuel, air, and hot combustion products [16].

In addition to the four main regions described by Chterev et al. [13], a three-dimensional unsteady asymmetric flow structure known as a precessing vortex core (PVC) has often been reported in turbulent swirl combustion devices [22, 23, 24, 25, 26, 27]. A precessing vortex core develops when a central vortex core starts to precess around the axis of symmetry at a well-defined frequency. This phenomenon is usually linked to vortex breakdown and the associated recirculation zone in a high Reynolds number flow. The occurrence of the PVC is a function of swirl number, mode of fuel entry, combustor configuration and equivalence ratio [22] and strongly affects the flow and flame structure in combustion systems. The precession of the vortex core squeezes the flow field at one side against the chamber wall, and causes a considerable increase in the tangential velocity in the squeezed flow region due to the conservation of angular momentum [16]. The presence of a PVC may improve combustion efficiency by enhancing turbulence intensity and mixing, but it could be a potentially undesirable characteristic due to the possibility of resonant coupling with the acoustics of the combustor.

In swirling flows with a centerbody, there exist three possible low velocity locations where a flame can stabilize: The inner shear layer, outer shear layer and upper or lower stagnation points of the vortex breakdown bubble. The location and spatial distribution of the flame has important consequences on combustor operability, durability and emissions. The flame structure can affect the heat loading on the combustor hardware. For example, the heat transfer to the centerbody is fundamentally different in a lifted flame versus a flame that anchors on the centerbody and a longer flame has more interaction with the combustor wall thus affecting combustor liner heat transfer. Blowoff limits are affected by local extinction events caused by the switching of flame stabilization locations. Combustion instability boundaries are affected as the delay time between when a flow perturbation is initiated and when it reaches the flame varies with flame structure [13].

For flow conditions (turbulent high swirl number flows) and geometries (relatively large centerbodies) in realistic gas turbine configurations, the flames stabilize at the inner shear layer (known as a V-flame) or at both the inner and outer shear layers (known as an M-flame). Sketches and photographs of V- and M-shaped flames observed in an experimental study are illustrated in Figure 1.6.

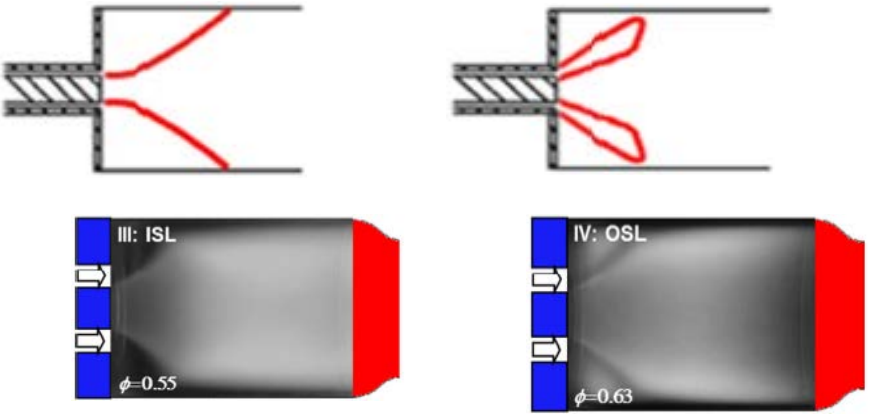

Figure 1.6. V-flame (left) and M-flame (right) [12]

Flames in most practical combustion systems experience some interaction with the surrounding hardware. In a gas turbine, the flame is confined so that the hot products generated by combustion can be transported to the turbine and therefore experiences a great deal of interaction with the combustor wall. The effects of a wall on flame quenching [28, 29] and heat transfer [28, 30] have been investigated both numerically and experimentally. More recent studies have focused on the effects of flame-wall interaction and confinement on the flow field and flame structure [31, 32, 33]. A DNS study by Gruber et al. [32] observed that the flame undergoes a change in combustion regime from a ‘thin flamelet’ regime near the flow centerline to a ‘thickened wrinkled’ regime close to the wall.

The idea of flame confinement is used to describe the space available for a flame to propagate before experiencing flame-wall interaction. In a single-nozzle combustor, the boundary conditions imposed on the flame are usually solid combustor walls and equal around its circumference. In multi-nozzle combustors however, the wall interaction experienced is generally not circumferentially equal. Therefore, the level of confinement experienced by the each flame in a multi-nozzle combustor would be an important factor that governs the overall flame structure. Flame confinement is often quantified in terms of a confinement ratio [34] which generally refers to a ratio of characteristic length scales e.g. the ratio of injector diameter to the combustor diameter. A confinement ratio has not yet been defined in a multi-nozzle combustor and will be defined in Section 3. The term dump ratio, which usually refers to the area of the dump plane divided by the open nozzle area, is also commonly used in industry to quantify confinement in a combustor.

LDV measurements of the flow field of a turbulent swirling flow in square ducts with varying degrees of confinement obtained by Fu et al [33] show that the flow field is highly affected by the level of confinement. As expected, all confined cases exhibit an outer recirculation zone, the size of which depends on the step size. Two distinct inner recirculation zones exist in the core of large ducts (low confinement), while only one inner recirculation zone exists in the core of small ducts (high confinement).

Nogenmyr et al. [31] used experiments to validate LES with the goal to demonstrate that a simple LES approach is capable of providing adequate information on the turbulent reacting flow field and flame structures of both unconfined and confined flames. They show that using realistic wall temperatures and boundary conditions is crucial in simulating the flame shape and the heat transfer characteristics of the combustor

Most practical gas turbine combustors employ multiple nozzles. The geometry and layout of the nozzles in the combustor is determined by the overall engine design and can be one of three types: can, annular and can-annular (Figure 1.7). In addition to flame-wall interactions, flame-flame interactions also affect the local flow field and flame structure in multi-nozzle combustors. The current study will focus on a 5-nozzle can combustor.

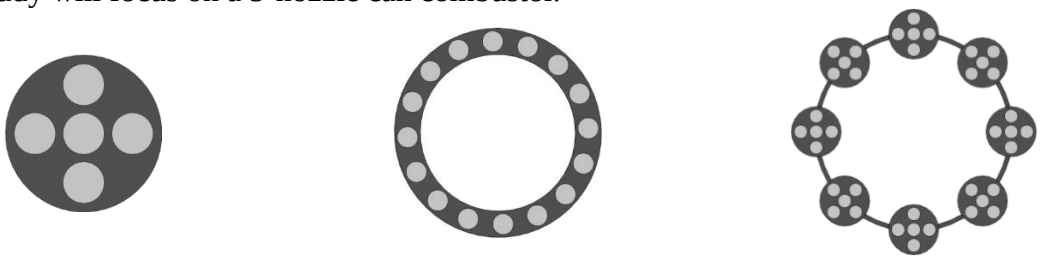

Figure 1.7. (a) 5-nozzle can combustor, (b) 16-nozzle annular combustor, (c) Can-annular combustor

In multi-nozzle combustors, there is significant interaction between adjoining swirling flows and flames. While this is an important phenomenon that governs flame structure and dynamics, this subject hasn't been extensively researched. Experiments and simulations have been performed on laboratory scale multiple flame configurations [35, 36, 37, 38, 39, 40] to investigate the structure of multiple interacting flames. However, studies on industrial scale multi-nozzle configurations are limited.

Worth and Dawson [35] performed experiments on two turbulent premixed bluff body stabilized flames and investigated the effects of separation distance on structure and response to perturbations. Their results (Figure 1.8) showed that as the two flames are brought closer together, the wake region between the two flames decreases and the merging of the flame fronts moves upstream. Compared with the flames that interact with the wall, the interacting flames show a thickened brush indicative of increased levels of turbulence generated by jet merging. This becomes more prominent when the flames are closer together.

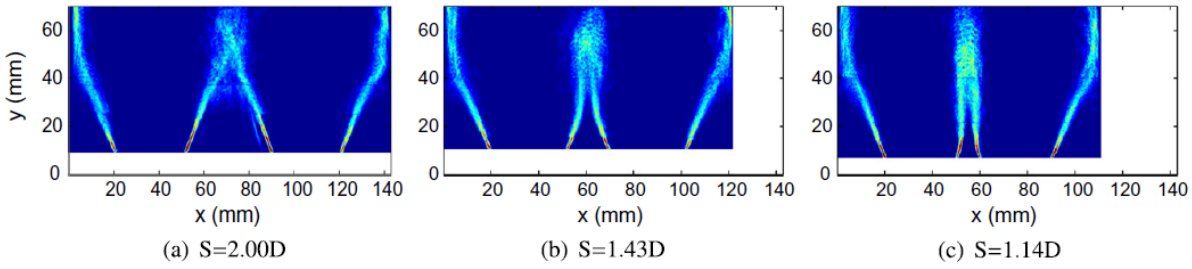

Figure 1.8. Effect of separation distance on flame structure [34]

Experiments that compared the flame structure and response in a single burner and an annular combustor were performed by Fanaca et al [41]. Their results show that the basic flame structures appear very different. OH* Chemiluminescence images (Figure 1.9) of the flames show that the single burner (SCC) flame on the right features a broad band of intensity with characteristic lobes at the sides, while in the annular combustor (ACC) flame on the left, the intensity is centered in two spots on either side of the central axis. This indicates that the flow field could be very different in an annular combustor compared to a single burner. Another experiment by Kunze et al. [42] on the same setup indicates that the effective swirl reduction in the annular combustor caused by interacting adjacent co-swirling flows influences the flame length and thereby the flame response characteristics. This illustrates the importance of the combustor chamber geometry on both flame structure and response.

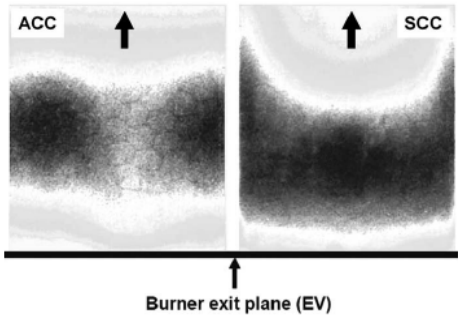

Figure 1.9. OH* Chemiluminescence images of a flame in a single burner (right) and an annular combustor (left) [40]

Using direct numerical simulations of twin turbulent V-flames for a range of turbulence intensities and length scales, Dunstan et al. [43] characterized flame-flame interactions using a novel feature extraction technique. Four distinct types of interactions were identified based on topological changes to the flame surface and characteristic length and time scales for all interactions were identified. The effects of these interactions on the turbulent flame brush were investigated by considering the global stretch rate of the flame.

Worth and Dawson [44] conducted experiments to determine the global flame response in a model annular gas turbine combustor undergoing strong self-excited circumferential instabilities. The combustor consisted of 12, 15 or 18 turbulent premixed swirl and bluff-body flames arranged around an annulus of fixed circumference. This allows the flame separation distance to be varied and its effect on the flame structure and dynamics to be investigated. It can be observed from the chemiluminescence images obtained from downstream of the combustor (Figure 1.10) that the mean heat release around of each flame shows a tendency to be mostly axisymmetric for higher flame separation. As flame separation distance is reduced, large-scale merging occurs between adjacent flames around the whole annulus. This results in a new asymmetric flame structure with the majority of the mean heat release occurring in the regions of large-scale flame merging and comparably little heat release along the inner and outer walls. The merged regions are angled with the direction of swirl.

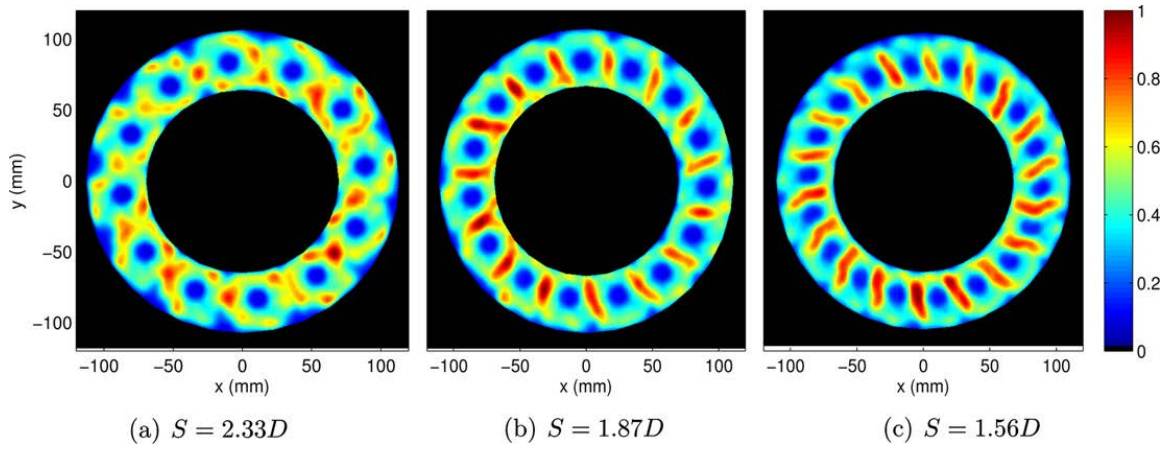

(a) $S = 2.33D$ (b) $S = 1.87D$ (c) $S = 1.56D$

Figure 1.10. Mean flame structure of flames in an annular combustor at varying separation distances [43]

The location of flame stabilization and flame structure are two important aspects to consider in the design of combustion systems as they play a crucial role in the heat transfer characteristics and determine the physical processes that control flame dynamics. Flame-wall and flame-flame interactions which also act to modify the flame structure and anchoring location(s) are, though not as well understood, also important considerations. Furthermore, the time averaged stabilization location varies with amplitude and frequency of the inlet perturbations during combustion dynamics [45, 46], implying that the underlying mechanisms that govern flame dynamics affect the local flame structure which in turn influences the heat release response.

1.3. Combustion Instabilities

Combustion instabilities are the result of naturally excited feedback loops that couple heat-release rate and pressure oscillations with the natural acoustic modes in a combustor [47, 48, 49]. They have been encountered in combustion systems related to propulsion (rockets [50], ramjets [51, 52], afterburners [52, 53, 54] etc.), power generation (land-based gas turbines [55], boilers [56]) and industrial use (furnaces [57], heating systems etc.). These instabilities result in sustained large amplitude pressure and heat release oscillations which in turn lead to fluctuations in the mechanical and thermal loads experienced by engine components downstream of the combustion nozzles. These could result in premature and/or catastrophic component failure (Figure 1.11). Other possible consequences of combustion instabilities are reduced combustion efficiency and increased emissions. As a result, this has been a topic of great interest within combustion research in the past decades. However, the understanding of the underlying mechanisms of combustion instability in realistic combustion systems is still incomplete.

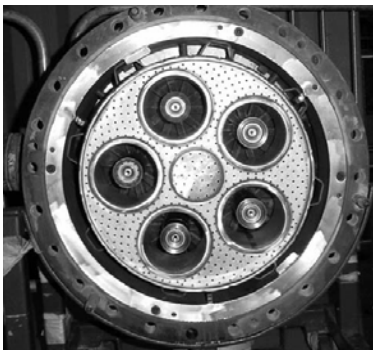

(a) Undamaged Gas Turbine Burner Assembly

(b) Failed burner assembly

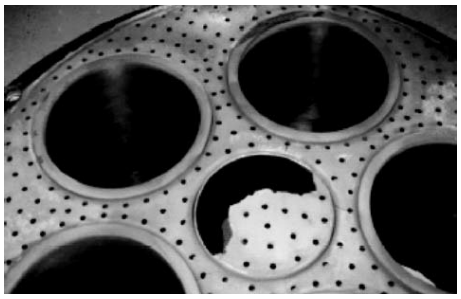

(c) Damaged burner face plate

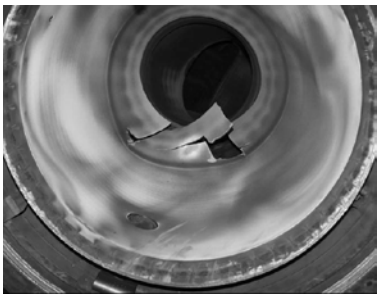

(d) Damaged combustor liner

Figure 1.11. Examples of natural gas turbines damaged by combustion instability [57]

Combustion instability is governed by a feedback process between acoustic oscillations in the combustion chamber, heat release fluctuations and fluctuations in the inlet mixture velocity and/or composition. Figure 1.12 illustrates the feedback loop responsible for combustion instabilities (Modified from Lieuwen and Yang [47]). In order to understand the entirety of the combustion instability process, it is necessary to understand each part of the loop. The loop consists of the following steps:

1. Flow and/or mixture perturbations induce a fluctuation in the heat release rate,
2. The heat-release fluctuation excites acoustic (pressure and velocity) oscillations,
3. The acoustic oscillations generate flow (vorticity and swirl strength) and mixture (equivalence ratio) perturbations

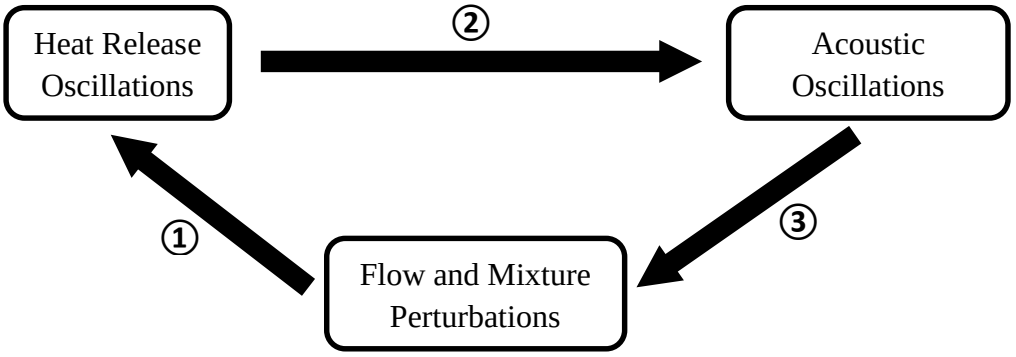

Figure 1.12. Feedback Loop for Combustion Instabilities [46]

The interaction between heat release fluctuations and acoustic oscillations is well understood. Heat addition to a gas causes its temperature to increase. At constant pressure, this results in volume expansion which performs work. In order to maintain the instability feedback loop, the heat release fluctuation (and thus, this volume expansion) must positively couple with the acoustic pressure field in the combustor. The conditions for this coupling were first proposed by Lord Rayleigh in 1878 [58]. Energy is added to the acoustic field if the heat release perturbation and pressure perturbations are in phase ($0° < \left|\theta_{p,\dot{q}}\right| < 90°$). Conversely, energy is removed from the acoustic field when the heat release and pressure perturbations are out of phase ($90° < \left|\theta_{p,\dot{q}}\right| < 180°$). This relationship is known as the Rayleigh criterion.

While the Rayleigh criterion describes conditions under which heat release rate oscillations add energy to the acoustic field, this alone does not imply that the combustor is unstable. Energy can be removed by viscosity, heat transfer and sound radiation. Depending on the relative magnitudes of the energy added and removed from the acoustic oscillations, the amplitude of oscillations may decrease, remain constant, or grow during each cycle of this loop. This statement can be summarized by the following equation [47]:

$$\int_V \int_T p'(x,t)q'(x,t)dtdV \geq \int_V \int_T \sum_i L_i(x,t)\,dtdV \qquad (1.4)$$

Where $p'(x,t)$ is the combustor pressure oscillation, $q'(x,t)$ is the heat release oscillation, V is the combustor volume, T is the period of oscillation and $L_i(x,t)$ is an energy loss process. The left hand side of the equation is the integral form of the Rayleigh criterion and is commonly referred to the Rayleigh integral and the right hand side of the equation describes the damping processes.

The next portion of the feedback loop involves acoustic oscillations triggering flow and mixture perturbations. This depends on the geometry of the system and the fuel injection method. In fully premixed systems such as the one used in this study, acoustic oscillations only generate flow perturbations. These flow perturbations are in the form of vorticity and swirl fluctuations. However, practical land-based gas turbines operate in technically premixed mode where fuel is injected a short distance upstream of the flame. In this configuration, while the fuel and air may be well mixed transversely (due to the induced swirl), it may not be completely and uniformly mixed axially before reaching the flame due to the relatively short mixing distance. This results in equivalence ratio fluctuations in the axial direction. Therefore in technically premixed systems, acoustic oscillations can generate both velocity and equivalence ratio perturbations.

1.4. Flame Response

The final part of the instability feedback loop, the generation of heat release oscillations by velocity and/or equivalence ratio fluctuations perturbing the flame, is one that is not completely understood. Therefore most of the research to understand combustion instabilities has focused on understanding this relationship, commonly known as flame response. Understanding the governing mechanisms of flame response is critical to develop a phenomenological model of combustion instabilities.

Research on flame response can be divided into two main categories depending on the nature of the inlet perturbations: self-excited response and forced response. During self-excited flame response investigations, an unstable flame couples with the system acoustics and the dominant

frequency of the self-excited oscillation must be determined from time varying measurements of pressure, velocity and heat release [59]. While the results of self-excited studies better resemble realistic gas turbine combustor conditions, the mechanisms responsible for instabilities cannot be isolated. In forced response investigations, inlet oscillations are generated by an external device such as a siren device or a loudspeaker at a known amplitude and frequency. The understanding of flame response mechanisms obtained from these studies can be used to develop thermoacoustic models to predict self-excited instabilities. The current study will focus on the forced response of fully premixed flames to velocity fluctuations.

In general, the heat release rate ($\dot{q}$) from a laminar premixed gas/air flame is given by the following expression:

$$\dot{q} = \rho_u A_f S_L \Delta h_R \qquad (1.5)$$

where ρ_u is the density of the unburned gas, S_L is the laminar flame speed, A_f is the flame surface area, and Δh_R is the heat of reaction per unit mass of the unburned mixture. The fluctuation of any of the four quantities on the right hand side of the equation results in a heat release rate fluctuation. While the density of the unburned gas scales directly with pressure fluctuations, pressure fluctuations are usually only a few percent of absolute mean pressure during combustion instabilities in gas turbines [60]. Therefore, the density of the unburned mixture may be treated as constant when characterizing flame response. Fluctuations of flame area, laminar flame speed and local heat of reaction are caused by perturbations in velocity and equivalence ratio [61]. Velocity perturbations generate vorticity fluctuations which wrinkle the flame front thus changing the flame surface area. Velocity perturbations may also cause flame speed fluctuations by generating fluctuations in the flame strain rate, but this effect is negligible at low frequencies [62] such as the frequency range investigated in this study. In contrast, the effects of equivalence ratio perturbations on flame speed, local heat of reaction and flame area are comparable. In fully premixed systems such as the one used in this study, heat release rate perturbations are only caused by velocity perturbations. Therefore, fluctuation in heat release rate is directly proportional to the relative fluctuation in flame surface area. However in technically premixed systems such as those used in practical gas turbine engines, both velocity and equivalence ratio perturbations cause changes in heat release rate. A companion study is being conducted to study the response of technically premixed flames in the multi-nozzle can combustor.

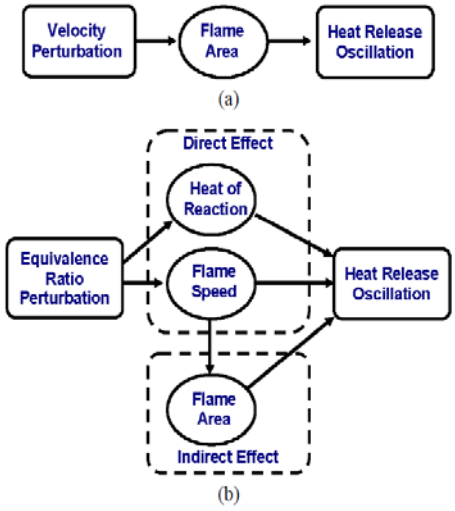

Figure 1.13. Processes that generate heat release oscillations caused by (a) velocity perturbations, and (b) equivalence perturbations [61]

1.4.1. Flame transfer function

In 1957, Merk [63] introduced the concept of a flame transfer function (FTF) to characterize flame response. It quantifies the relationship between overall heat release rate oscillations from a flame subject to oscillations in the inlet mixture. For the case of fully premixed flame response to velocity oscillations, the flame transfer function depends on both the frequency and amplitude of the inlet velocity oscillation and is defined as:

$$FTF\left(f, \frac{u'}{\bar{u}}\right) = \frac{\dot{q}'(f)/\bar{\dot{q}}}{u'(f)/\bar{u}} \qquad (1.5)$$

Here, $\bar{\dot{q}}$ is the time-averaged heat release rate from the flame, $\bar{u}$ is the mean inlet mixture velocity, $\dot{q}'$ is the magnitude of the heat release rate oscillation, u' is the magnitude of velocity oscillation, f is the frequency of oscillation, and $u'/\bar{u}$ denotes the amplitude of the velocity oscillation. The flame transfer function is a complex quantity; it characterizes both the magnitude and phase of the heat release rate response. The magnitude of the flame transfer function is commonly referred to as "gain" and quantifies the ability of the flame to amplify or damp the heat release rate response. The phase of the flame transfer function represents the delay between acoustic velocity oscillations travelling into the flame base and corresponding global heat release rate oscillations from the flame.

1.4.2. Flame response regimes

Flame response is divided into linear and nonlinear regimes. The regime where the normalized heat release rate fluctuation amplitude, $\dot{q}'/\bar{\dot{q}}$ scales linearly with the normalized velocity fluctuation amplitude, $u'/\bar{u}$ is known as the linear regime. Here, the flame transfer function gain (slope of the curve in Figure 1.14) is constant i.e. independent of velocity fluctuation amplitude. As the amplitude of the velocity fluctuation increases, the flame response transitions to the nonlinear regime. Nonlinearities in flame response cause the heat release rate response to saturate and the gain of the flame transfer function depends on inlet velocity fluctuation amplitude (Figure 1.14).

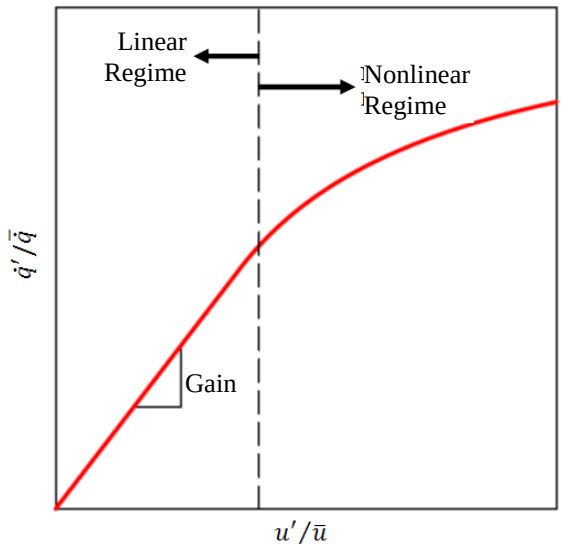

Figure 1.14. Flame response regimes

1.5. Literature Review: Velocity Forced Flame Response

A number of studies which include experimental, theoretical, and computational investigations have been performed in order to understand flame response of fully premixed flames to inlet velocity fluctuation and its underlying mechanisms. Excluding a select few studies, much of the research on combustion instabilities has been performed on single-nozzle, laboratory scale combustors. Investigations of flame response in both laboratory scale and realistic combustors will be reviewed with a focus on studies of turbulent fully premixed flames. Proposed mechanisms for velocity forced flame response will then be reviewed and finally, the effects of flame-wall interaction and flame-flame interactions on flame response (which are important considerations for multi-nozzle systems) will be discussed.

Many of the earlier studies on flame response focused on the response of laminar premixed flames to inlet fluctuations [64, 65, 66, 67, 68, 69, 70, 34]. The results of these studies show that the nature of flame response depends on flame structure, forcing frequency and amplitude and that flame response could potentially be determined by multiple mechanisms. This fundamental understanding of flame response motivated more recent investigations on the flame response of turbulent flames in single-nozzle and multi-nozzle combustor configurations.

One of the first studies on turbulent flame response was performed by Külsheimer and Büchner [71] who studied the influence of periodic mass flow excitation on the flow field and flame characteristics of axial jet flames and swirling flames. Their results showed that the interaction of coherent ring-vortex structures with the combustion process is a fundamental phenomenon that governs the occurrence of instabilities and that the formation of these coherent structures are determined by two dimensionless parameters; the pulsating level (normalized RMS fluctuation of mass flow rate at the burner exit) and Strouhal number ($St = fL/U$) where f is the pulsating frequency, L is a characteristic length scale and U is the velocity of the fluid. Furthermore, a difference in the response of jet flames and swirling flames was observed which the authors attributed to the higher entrainment of ambient air by swirling flames which results in local changes in equivalence ratio.

Experimental results of swirl-stabilized, turbulent premixed flames by Kim et al. [72] suggest that M-shaped flames are less influenced by the interaction with vortex ring structures when compared to V-shaped flames. In addition to Strouhal number, the flame dynamics were shown to also be characterized by the flame length and flame angle indicating that flame shape and location plays an important role in determining flame response. A further study by Kim et al. [73] on the dynamics of turbulent V-flames showed that the resonance type behavior of a turbulent swirl-stabilized flame is controlled by the nondimensional ratio of half the convective wavelength to the flame length ($0.5\lambda_{conv}/L_f$). Flame transfer function measurements made at 26 operating conditions were shown to collapse when normalized by this ratio. It was also shown that increasing the swirl number increased turbulence intensity and hence increased the flame angle and decreased the flame length which results in a reduced flame transfer function gain due to improved acoustic stiffness of the flame.

Palies et al. [74] investigated the dynamics of premixed confined swirl-stabilized flames and confirmed previous findings of transfer functions (gain and phase) data collapsing when normalized by a Strouhal number particularly at lower frequencies. Their experiments indicate that the flame response is controlled by the relative phasing between the azimuthal velocity

perturbations generated at the swirler and axial velocity perturbations generated at the injector exit. Another study by the same authors [75] showed that radial and axial swirlers exhibited the same characteristic response while the amplitude of the response was highly dependent on swirl number thus illustrating the dependence of combustor hardware on flame response.

The response of a turbulent, perfectly premixed flame to upstream acoustic perturbations was investigated using both experimental and analytical tools by Borghesi et al [76]. The results of this study show that the flame dynamics are dominated by the response of the flow field to the inlet perturbation. This suggests that combustion instabilities in gas turbine engines may depend on how swirling flows, especially in the regions where flow recirculation occurs, respond to acoustic perturbations.

Balachandran et al. [77] performed experiments to study the non-linear flame response of a bluff-body-stabilized turbulent premixed flame. Non-linearity in flame response was observed when the reacting shear layers rolled up into vortices. These vortices not only generated flame area when the flame wrapped around them but also caused cusps and even large-scale “flame annihilation events”. Their results suggest that the flame sheet kinematics play a major role in the saturation mechanism of lean premixed flame response. They also indicate that the heat release fluctuations due to local fluctuations of strain rate and curvature have a smaller effect on the global heat release rate even at large forcing amplitudes.

The vast amount of research on flame response in single-nozzle combustor configurations has shown that the heat release response has a strong dependence on flame structure and the response of the flow field response to inlet velocity oscillations. However, the current understanding on the detailed mechanisms that govern this response is still limited.

Since most practical gas turbine systems utilize multi-nozzle combustors, it is important to determine the response of multi-nozzle flames to inlet oscillations. A majority of research uses results derived from single-nozzle studies to inform the design and development of industrial gas turbine engines. In doing this, it is assumed that single-nozzle data is representative of the behavior of the behavior of the individual flames in realistic multi-nozzle gas turbine combustors. Whilst the validity of this has not been fully determined as yet, there are some studies that have attempted to assess flame response in multi-nozzle combustors and correlate it to single-nozzle results.

One of the first multi-nozzle studies was performed on an annular combustor by Kunze et al. [42]. Here, the response of the flame(s) is presented in terms of experimentally measured flame transfer functions which relate the fluctuation of the flame heat release rate (obtained by measuring OH^* chemiluminescence with a photomultiplier tube) to the axial velocity fluctuation at the burner outlet (measured using a hot wire probe). The response of a single-nozzle combustor and the annular combustor are compared and the differences observed are attributed to two effects. The first effect that occurs at low frequencies is an increased gain in the annular combustor that the authors attribute to the interaction of adjacent co-swirling flows that creates a low swirl region in between adjacent nozzles. This led to the flames in the annular combustor being longer and showing an increased gain response compared to their single-nozzle counterparts. At higher frequencies, a second effect in the form of an azimuthal mode, a circumferentially propagating acoustic wave traveling around the combustor annulus caused changes in the flame structure and response. Fanaca et al. [78] developed a network model of the acoustical field in this annular combustor and compared the model parameters developed in the single-nozzle and annular

configurations. The modal pressures calculated using the network model compared well to the experimental data obtained was shown for a fixed location over the entire frequency domain as well as around the circumference at a fixed frequency.

Worth and Dawson [44] conducted experiments to determine the global flame response in a model annular gas turbine combustor undergoing strong self-excited circumferential instabilities. The geometry of the combustor allowed the flame separation distance to be varied by changing the number of nozzles in the annulus, and its effect on the global heat release dynamics to be investigated. Their results showed that reducing flame separation produced an increase in both the resonant frequency and the limit-cycle amplitudes of pressure and heat release. High-speed OH* chemiluminescence images obtained from downstream of the combustor, showed that these changes are caused by large-scale modifications to the flame structure around the annulus. Phase averaged global heat release measurements show that when self-excited instabilities occur for large flame separation, each flame behaves independently and adopts a helical heat release structure. As flame separation is reduced, merging of global heat release occurs along the outer annular wall and extends around half of the annulus. These large-scale structures occupy opposite sides of the annulus with a 180° phase difference in peak heat release and a counterclockwise spin.

O'Connor collaborated with the Worth & Dawson in a study comparing the response of the annular combustor described above to a single-nozzle experiment subject to transverse excitations [79]. They show that despite obvious differences in flame structure, the flame behavior during a self-excited, standing-wave instability is fundamentally similar in an annular model combustor and a transverse rig forced with a standing-wave pattern. At the pressure anti-node, symmetric fluctuations that stem from ring vortices shed in the shear layers was observed in both configurations. At the pressure node, asymmetric motion due to helical vortex shedding was observed in the flames in both configurations. Several key considerations that should be accounted for in the comparison of results from single-nozzle and multi-nozzle investigations are then discussed. The "macro" geometry and behavior of the flow field particularly the structure of the recirculation zones, flame structure and anchoring locations and acoustic conditions should be matched for accurate comparison between these types of experiments. However, differences in flame response due to flame front merging in closely spaced annular flames cannot be accurately captured by studying a single flame; two or more flames need to be studied to accurately capture the merged flame dynamics.

The only published work of the flame response in a can combustor was performed by Szedlmayer et al. [2]. In this study, the response of a turbulent premixed flame in a multi-nozzle can combustor was compared to that of a single nozzle combustor which utilized the same injector type. Over broad range of operating conditions, the response of the multi-nozzle flame was qualitatively similar to a single nozzle flame when subjected to inlet velocity fluctuations. However, the actual transfer function gain values and frequencies of maximum and minimum gain differed. The multi-nozzle transfer function data showed collapse with Strouhal number in a similar manner to single-nozzle data which suggests that either similar (or the same) mechanisms govern flame response in both these cases.

The work reviewed above show that the flame response in multi-nozzle combustors exhibits differences to that of a single-nozzle combustor thus indicating that the assumption of single-nozzle data being representative of the behavior of practical gas turbine devices may not be valid.

The results also suggest that the governing mechanisms of flame response in multi-nozzle combustor are much more complex than in single-nozzle combustors.

1.5.1. Mechanisms of flame response

Several mechanisms that could govern the flame response characteristics of fully premixed, velocity forced, turbulent flames have been proposed. The following section will review studies that investigated changes in flame area due to: (i) axial velocity fluctuations, (ii) flame-vortex interactions, and (iii) swirl fluctuations. A combination of two or more of these mechanisms may determine the flame response. This can occur by multiple mechanisms affecting the flame simultaneously or different parts of the flame being affected by different mechanisms.

Using the results of an experimental study on a laboratory scale single-nozzle swirl-stabilized combustor, Jones et al. [80] proposed a mechanism for the change in flame area due to the interaction between two phenomena: One is the direct effect of the inlet velocity fluctuation on the mean flame area or mean flame length (axial velocity fluctuation), while the second is the effect of the vorticity fluctuations generated at generated at the exit of the injector by the inlet velocity fluctuation (flame-vortex interaction). The results showed similar behavior to a mechanism proposed by Palies et al. [74] where a high flame response was a result of these two disturbances being in-phase and a minimum flame response resulting from the disturbances being out-of-phase.

Palies et al. conducted experimental [74], analytical [81], and computational [82] studies to investigate the response of turbulent, swirl-stabilized premixed flames to velocity forcing. The authors observe that the swirler adds an oscillating azimuthal velocity component to the flow field. The combined axial and azimuthal velocity oscillations will generate swirl number fluctuations. This manifests into the flame and combines with vortex roll-up inducing changes in flame angle and flame surface area at the flame root.

In the experimental study [74], chemiluminescence images of the flame (obtained at a range of frequencies at two Reynolds numbers) were divided into upstream and downstream windows and analyzed independently. Results showed that at transfer function gain minimum conditions, the heat release components of the upstream and downstream regions of the flame were out of phase and destructively interfere. Conversely, when the upstream and downstream regions of the flame are in phase, they constructively interfere and result in a maximum gain condition. Using a combination of previous experimental data and an actuator disk theory-based analytical model, the flame area oscillations of the upstream region (flame root) are attributed to changes in swirl number and the flame area oscillations of the downstream region (flame tip) are attributed to vortices shed from the injector.

In the corresponding analytical study [81], the response of the experimentally observed turbulent swirling flame to axial and azimuthal velocity perturbations was modeled using a linearized version of the G-equation (first proposed by Markstein [83]). It is first concluded that the flame motion results from the combined effects of axial and azimuthal velocity perturbations. It is also shown that the phase difference between the axial velocity perturbation (which travels at the speed of sound) and the azimuthal velocity perturbation (which is convected by the mean flow) is an important parameter which should be accounted for in accurately modeling the global flame response.

Large eddy simulation calculations of the flame configuration used in the above analytical and experimental studies indicate that the interaction of vortex shedding and rotation rate fluctuations (swirl number fluctuations) interfere either constructively or destructively to induce a large or small heat release fluctuation [82]. This was also shown to depend on the inlet acoustic wave frequency. Results showed strong vortex roll-up when fluctuations of the rotation rate were limited and the inner recirculation zone strength was weak. In contrast, less intense shedding and roll-up process was observed when the large fluctuations in the IRZ strength were present and the rotation rate was high.

Bunce et al. [84] obtained flame transfer function measurements over a large range of inlet conditions where all the FTF gain curves showed alternating gain minima and maxima with increasing velocity forcing frequency. The results of the study showed that while phase difference between the axial velocity fluctuation and swirl number at the minimum FTF gain conditions was consistent with destructive interference between two mechanisms, the phase difference at the maximum FTF gain condition was not consistent with constructive interference. Furthermore, an inverse trend between the magnitude of the fluctuation of the flame base (caused by swirl number fluctuations) and the flame transfer function gain was observed. The proposed mechanism for this behavior is that as the flame position fluctuates, the vortex shedding associated with Kelvin-Helmholtz instability in the shear layer is damped resulting in low flame response. The results of this investigation are significant as they apply to a broad range of operating conditions.

More recently many researchers such as, Meier et al. [26, 85, 86], and Basu et al. [87] have attempted to better understand the interaction of the inlet perturbation with the flow structure in the combustor which in turn governs flame dynamics. Experimental measurements of the self-excited swirling flow field in a model gas turbine combustor obtained by Meier et al. showed several distinct flow patterns: reactants periodically entered the combustor at a dominant frequency that the authors define as the ‘thermo-acoustic frequency’, a helical precessing vortex core (PVC) circumscribes the burner nozzle at a frequency different to the thermo-acoustic frequency but undergoes axial extension and contraction at the thermo-acoustic frequency. Chemiluminescence measurements of the flame showed that the global heat release rate fluctuates at the thermo-acoustic frequency: however, the centroid of heat release moves around the combustor at a frequency which is the difference between the thermo-acoustic and PVC frequencies. This periodic deformation of the PVC caused it to interact with the flame in an oscillatory manner over the thermoacoustic cycle. Depending on the relative shapes of the flame and the PVC in their axially extended and contracted configurations, these interactions caused flame surface area fluctuations at different thermoacoustic phase angles thus heavily influencing the thermoacoustic state of the combustor.

1.5.2. Effects of flame-wall interaction and confinement

As one would expect, the confinement experienced by the flame strongly influences its geometry and the flow field in which it resides. Both are factors which have been shown to affect flame response. Confinement and flame-wall interactions are therefore important issues to be considered in the process of understanding combustion instability. Fu et al. [33] performed an experiment using LDV on a non-reacting swirling flow field. The results show that changes in flow field that result from altering the confinement are important in determining the flame response to inlet oscillations.

Birbaud et al. [34] investigated the dynamics of inverted conical flames anchored on a central bluff-body both in confined and unconfined conditions. Cylindrical ducts with different diameters are used to modify confinement conditions and examine their effects on the flame response (Figure 1.15). Their results show that in the absence of confinement, the flame response is governed by the interaction between vortices shed at the injector exit which causes large heat release rate fluctuations. When the confinement ratio is increased but remains low, the flame propagates freely and vortices are weakly affected by the presence of the wall. It is shown that strong interactions with the wall occur when the confinement ratio exceeds a critical value. In this case, the vortex interaction is notably modified. The transfer function gain remains almost constant over a range of Strouhal numbers.

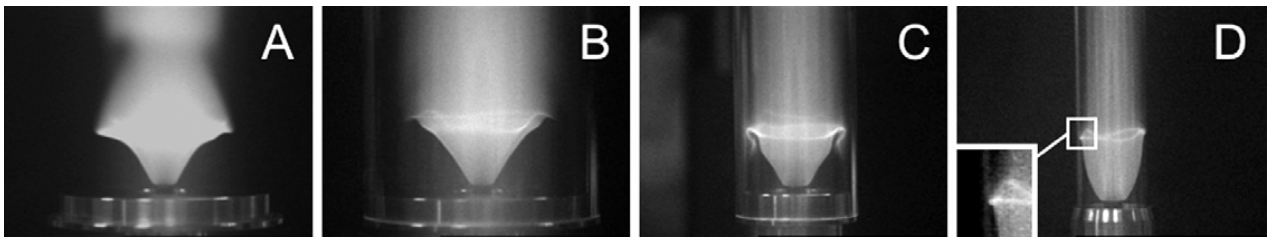

Figure 1.15. Steady inverted conical flames with different confinement ratios [33]

Kedia et al. [88] numerically investigated the response of perforated-plate stabilized premixed, laminar methane–air flames to inlet velocity perturbations. It was shown that the oscillations of heat exchange rate at the top of the burner surface and the heat transfer to the combustor walls play a critical role in driving the growth of the perturbations by affecting the convection of reactants to the flame base, and from the flame base to the flame tip.

1.5.3. Effects of flame-flame interaction

The interaction of adjacent flames is expected to strongly affect the response of a flame to inlet oscillations and is part of the reason why single-nozzle and multi-nozzle flame response differs.

An early study of this effect conducted by Poinsot et al. [89] showed that the interaction between vortices formed in neighboring jets has a significant effect on flame response and the flow field within the combustor. The authors attribute this to the production of small scale turbulence and intense mixing. A study on the response of multiple flames anchored on a perforated plate burner was conducted by Noiray et al. This showed that the mutual flame annihilation resulting from the merging of adjacent reactive sheets periodically releases pockets of fresh gases which drive self-sustained instabilities [90].

In their study of two premixed, bluff-body stabilized, turbulent flames [35], Worth and Dawson also studied the response to inlet velocity fluctuations in addition to the structure of interacting flames. The jet merging that occurs as a result of the flames being brought closer together was shown to have an effect on flame response which was dominated by the formation of vortex structures that interact with the flame. At lower separation distance, the adjacent flame fronts rolled-up together as a single vortex pair. A rapid production of flame surface area occurs followed by the merging of adjacent flame fronts in the wake of the vortex pair which simultaneously breaks down. At higher separation distances, flame fronts rolled up separately as two pairs generating flame surface area by the collision of adjacent vortex pairs. A majority of the unsteady heat release

was shown to occur in the interacting region. Another interesting result from this study was that the transition from linear to non-linear behavior occurred at a lower forcing amplitude for lower flame spacing cases.

1.6. Motivation and Objectives

There is a large amount ongoing research aimed at understanding combustion instabilities and the fundamental mechanisms that drive them. However, it is evident from the literature review that the understanding of the driving mechanisms is not complete. While multiple mechanisms have been proposed, the interaction of these mechanisms is not fully understood. Furthermore, flame response research in multi-nozzle combustors is limited and the understanding of the additional mechanisms that occur in these configurations e.g. varying confinement and flame-flame interaction is minimal.

Previous research on the multi-nozzle can combustor used in this study by Szedlmayer [2] yielded an extensive set of flame transfer function data at a range of inlet operating conditions, forcing frequencies and forcing amplitudes. The flame transfer functions obtained showed qualitative similarity to those obtained in single nozzle experiments with alternating gain minima and maxima. The results of the investigation showed that at low frequencies, the interaction of vertical structures with the flame had a large effect on flame response. However, a complete understanding of the governing mechanisms was not obtained.

Using the 3-D imaging technique developed by the author (discussed in Section 2), previously unavailable data on the structure of the multi-nozzle flame was obtained. The main goal of this study is to use this data to obtain a phenomenological understanding of flame response by identifying and characterizing the instability driving mechanisms through which velocity fluctuations result in heat release fluctuations in lean-premixed swirled multi-nozzle flames and the manner in which these mechanisms interact to cause extrema in the flame transfer function. This will be achieved by studying the response of various regions of the flame and understanding their interaction. Efforts will also be made to improve the understanding of the effects of varying confinement and flame-flame interaction on flame response.

A long term goal of this study is to determine the extent to which the flame response results obtained in a single-nozzle laboratory combustor can be used to predict the flame response in a multi-nozzle combustor.

2.0 Experimental Setup and Methods

2.1 Multi-Nozzle Can Combustor

The multi-nozzle can combustor used in this study has been used in previous work by Szedlmayer et al [2, 91] and is schematically illustrated in Figure 2.1 and Figure 2.3. It consists of five swirl stabilized nozzles mounted in a “four around one” configuration inside an optically accessible, open-ended combustor can. The combustor is operated with a fully premixed mixture of air and natural gas fuel. Air is supplied to the experiment by an air compressor system capable of providing a mass flow rate of up to 0.3 kg/s at a pressure of 2000 kPa. The air flow rate is controlled by a needle valve and monitored by a mass flow meter (Sierra Instruments Model 760S) with a

maximum flow rate of 0.16 kg/s. The pressure at the meter is controlled by a Powreactor dome regulator and set to 1400 kPa. To achieve the desired range of combustor inlet velocities, the flow rate is varied between 0.05 and 0.16 kg/s. A 50 kW process air heater (Tempco) is used to preheat the air to the desired combustor inlet temperatures (between 50°C and 250°C).

Natural gas consisting of approximately 95% methane is the primary fuel used in this study. A fuel manifold is used to supply the test rig with natural gas by discharging pressurized storage tanks through a series of regulators and heaters designed to prevent excessive cooling during expansion when the fuel pressure is reduced to the operating pressure of 1400 kPa. The fuel is injected into the heated air through a multi-hole injector designed to enable rapid mixing. The fuel and air are further mixed as they flow through several meters of pipe, elbows and a choked orifice. This premixing process ensures that the equivalence ratio of the fuel-air mixture entering the combustor is constant i.e. the incoming mixture is fully premixed. The natural gas flow rate is controlled by a needle valve and monitored by a Teledyne Hastings 300 series mass flow meter.

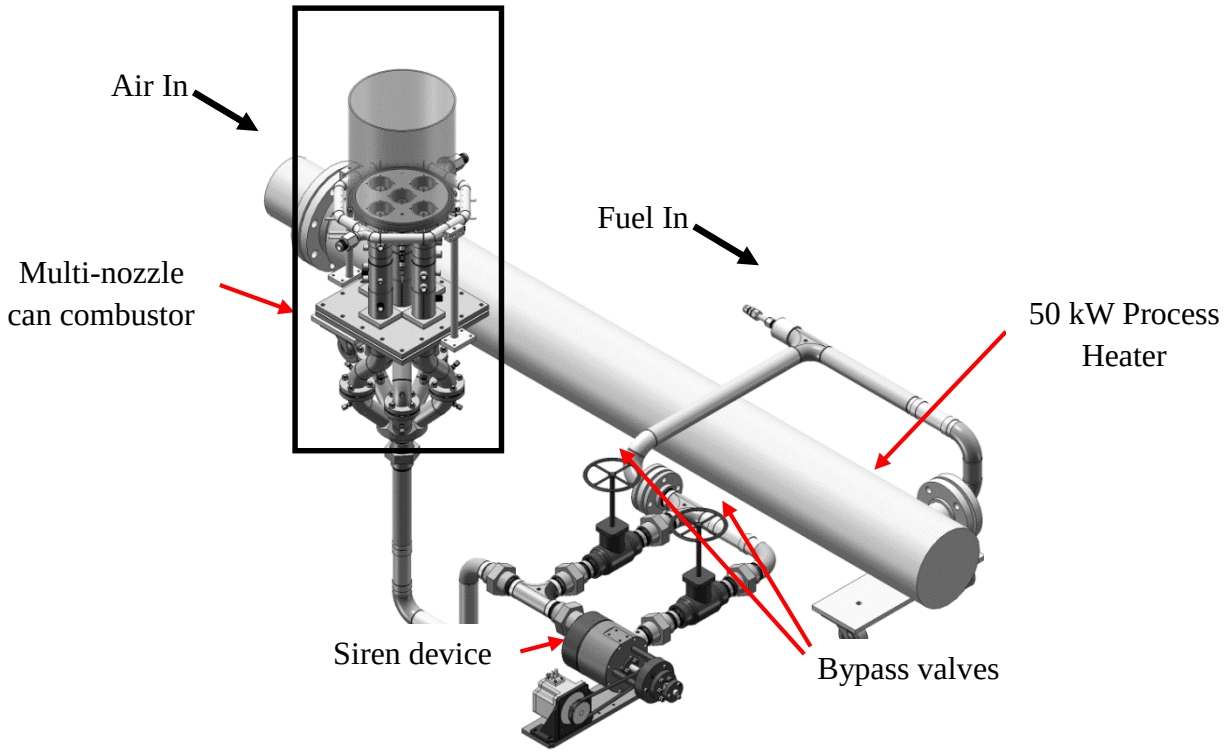

Figure 2.1. Schematic of multi-nozzle experiment

The premixed fuel and air then enters a rotor-stator siren device that is used to periodically modulate the velocity of the fuel-air mixture. The siren primarily consists of a rotor with four holes and a fixed stator with a single open passage (Figure 2. 2). The fuel-air mixture flows freely when a rotor hole aligns with the open passage of the stator. The siren rotor is driven by a brushless DC motor (Vexta BLFM6400-A) and this generates a sinusoidal perturbation in the mixture flow rate. The frequency of this perturbation is determined by the rotational speed of the siren rotor, while the RMS amplitude is controlled by varying the fraction of the fuel-air mixture that bypasses the siren. Each time the rotor makes a full rotation, an incremental rotary encoder (Koyo TRD-GK360-RZD) provides an electronic signal to the data acquisition system. This signal triggers the acquisition of pressure and heat release rate data.

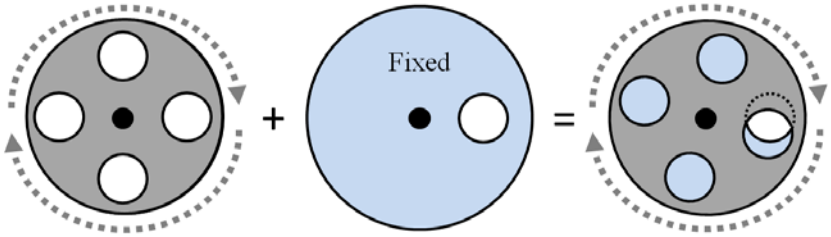

Figure 2.2. Siren rotor, stator and combined system [2]

Downstream of the siren, the fuel-air mixture enters a manifold (Figure 2.3) which divides the flow into five separate streams, one for each of the nozzles in the multi-nozzle combustor. The design of the manifold is such that all five flow paths are geometrically identical. A perforated plate is installed in each leg of the manifold to help ensure that the flow to each nozzle is approximately the same. After exiting the manifold, the fuel-air mixture flows to each of the nozzles which consist of a centerbody and a counter-clockwise axial swirler. The swirl number is on the order of that of a swirler used in practical gas turbine combustors (S = 0.70). The nozzles are mounted in a "four-around-one" configuration and their spacing relative to the diameter of the combustor can is typical of industrial can combustors. The ratio of total nozzle area to the dump area (or dump ratio) is approximately 6. The nozzles exit into a 260mm diameter, 300mm long quartz combustor can with a wall thickness of 5mm which is unrestricted and open to the atmosphere. Therefore combustion takes place at atmospheric pressure.

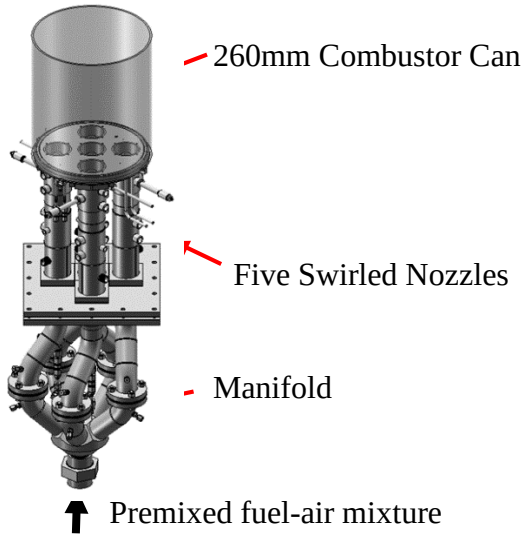

Figure 2.3. Schematic drawing of multi-nozzle combustor

In addition to the hardware described above, a variety of equipment regulates the environment in which the experiment is conducted. The outer surface of the quartz combustor wall is cooled by jets of air (flow rate = 0.067 kg/s). An exhaust hood above the experiment draws in combustion products and air from the room. An array of spray nozzles (Hago M10) sprays a fine mist of distilled water into the hot exhaust. This provides evaporative cooling and maintains the exhaust temperatures less than 300°C. Two portable industrial air conditioning units provide spot cooling to the data acquisition system and high speed camera to ensure that operating temperatures do not exceed allowable operating limits.

2.2 Measurements and Data Acquisition

2.2.1 Pressure Measurements

Pressure drop across the swirler is measured using electronic differential pressure gauges (Omega PX277-30D5V). Mean velocity of the incoming fuel-air mixture is obtained by applying empirical calibration data to these pressure drop measurements. The accuracy of this measurement is ±1 m/s. The measured nozzle-to-nozzle variation in mean velocity was ±2 m/s.

Piezoelectric pressure transducers (PCB 112A22) are used to obtain dynamic pressure measurements in three of the five nozzles. At each nozzle, pressure transducers are mounted at two locations between the swirler and the end of the centerbody. The spacing between the pressure transducers is 38mm. Signal conditioners (PCB 482A16) connected to each transducer are used to amplify and filter the signals before they are read into the data acquisition system. These measurements are used as inputs to a two-microphone method (TMM) calculation (described in section 1.2.1) which provides the time varying velocity in each nozzle.

2.2.1 Temperature Measurements

Temperatures at various locations of the system are monitored using K-type thermocouples to ensure that safe operating conditions are maintained. The temperature of the inlet fuel-air mixture is measured approximately 25 mm upstream of the swirler in each of the nozzles. The variation in mixture temperature between the five nozzles is less than 10˚C. The temperature in the middle nozzle serves as the control temperature for the air heater.

2.2.2 Heat Release Rate Measurements

The response of a flames heat release rate to inlet perturbations is a major factor in describing the instability characteristics of a combustion system. This is obtained from line-of-sight measurements of the natural chemiluminescence emissions produced by the combustion reaction. During the lean combustion of hydrocarbons and air, the strongest narrowband chemiluminescence emission is due to excited OH^* and CH^* radicals. As these radicals transition from excited electronic states back to the ground state, light is emitted at a narrowband centered at a specific wavelength. The CH^* radical emits light at 432 nm and the OH^* radical emits at 308 nm. The CO_2^* radical is also produces a strong chemiluminescence emission at a broadband wavelength interval (350–600 nm). The chemiluminescence emission spectrum from a lean premixed natural gas-air flame is shown in Figure 2.4.

For a flame with a fixed equivalence ratio, it has been shown that the CH^* and OH^* chemiluminescence intensity have a linear dependence on the mass flow rate of the reactants [92]. Since the global heat release rate is a function of only the mass flow rate, the linear relationship between chemiluminescence intensity and mass flow rate implies that chemiluminescence can be used as an indicator of heat release rate for flames with a fixed equivalence ratio i.e. fully premixed flames.

A number of limitations associated with this technique need to be considered. First, the narrowband chemiluminescence signals measured at the CH^* and OH^* wavelengths are partially due to CO_2^* broadband emissions. Therefore, to accurately measure CH^* and OH^* chemiluminescence, an independent measure of CO_2^* background intensity should be acquired which was not available for the current study. A second limitation deals with the fuel injection location. In realistic gas

turbine combustors, the fuel is typically injected slightly upstream of the flame anchoring location. This 'technically premixed' configuration gives rise to both velocity fluctuations and equivalence ratio fluctuations. The dependence of chemiluminescence intensity to equivalence ratio fluctuations is non linear and therefore, the chemiluminescence intensity is no longer directly proportional to heat release rate. In this study, this limitation is overcome by injecting the fuel far upstream of the flame anchoring location and flowing it through a choked orifice to prevent pressure oscillations from affecting the fuel flow rate. Another limitation that affects local chemiluminescence measurements i.e. chemiluminescence images, deals with the line-of-sight nature of the measurement. Because the entire flame produces chemiluminescence emission, the detected signal is the sum of the emission along a line-of-sight and therefore is not spatially resolved. In order to overcome this limitation, the 3-D distribution of chemiluminescence must be reconstructed from a number of 2-D line-of-sight projection images using a tomographic image reconstruction technique. The technique used to do this will be discussed in section 2.4.

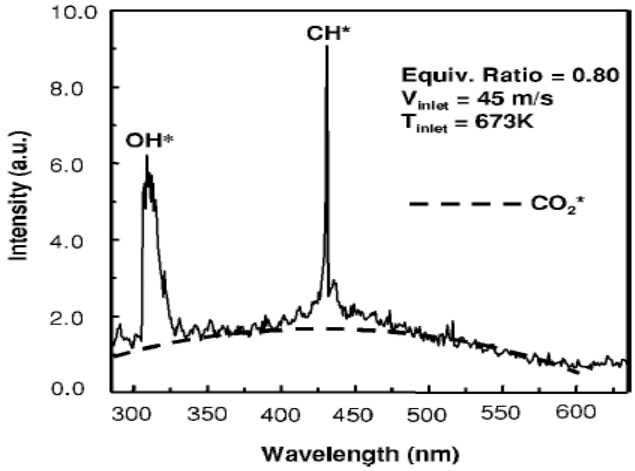

Figure 2.3. Chemiluminescence emission spectrum of a lean premixed CH_4-air flame [3]

In this study, the total rate of heat release of the entire flame as a function of time is determined from measurements of CH* emission using a photo multiplier tube (Hamamtasu H7732-10 with an integrated high voltage supply) fitted with a 432±5 nm bandpass filter.

The spatial distribution of the flame's rate of heat release is obtained by imaging the CH* chemiluminescence emission onto a camera-intensifier setup. For the part of this study that involved developing and validating the 3-D image reconstruction technique, an ICCD camera (Princeton Instruments #5768) was used. For the rest of the study, a high speed camera (Photron SA4) fitted with an intensifier (Invisible Vision UVi) is utilized. The high-speed camera's capacity to obtain images at a much higher frame rate than the ICCD camera results in a much shorter data acquisition time. The camera-intensifier setup is fitted with a Nikon AF Micro-Nikkor 60mm f/2.8D Lens and a 432nm ± 5nm bandpass filter. Each line-of-sight (projection) image captures one second of data acquired at a predetermined frame rate. Each projection image is background subtracted and corrected for dark current and flatfield effects of the detector. This is done using equation (2.10) below:

$$CI = \frac{(RI - DC) - (BG - DC)}{FF - DC} \qquad (2.1)$$

Where CI is the corrected image, RI is the raw image, BG is the background image, DC is the dark current correction and FF is the flatfield correction. Subtracting the background image, which is acquired with the same camera-intensifier settings as a raw image but with no flame present, removes the chemiluminescence signals not associated with the flame. The dark current image acquired with the sensor closed (lens cap on) is the signal output by the detector when there is no incident light. Subtracting this image from the raw images corrects for noise from the sensor in the form of dead or hot pixels. A flatfield image is obtained by acquiring an image of a uniform surface. Correcting for the flatfield eliminates error caused by variations in the pixel-to-pixel sensitivity of the detector and/or by distortions in the optical path

When imaging an unforced flame, 2000 frames (one second) of high speed chemiluminescence data are acquired and averaged to obtain a single mean image. This averaged image is then processed using 3-D reconstruction.

During the forced flame tests, the camera is triggered off the incremental rotary encoder attached to the siren motor. The encoder provides a trigger signal which starts the camera acquisition. However, this trigger signal does not necessarily correspond to a distinct phase angle within a forcing cycle and therefore, a delay was added to the encoder signal to account for the phase difference between the encoder and velocity obtained by the two microphone measurement. Each forced flame image captures 4000 frames (one second) of high speed chemiluminescence data. The images are processed in the frequency domain to characterize response at the forcing frequency (described in section 1.2.2) before applying the 3-D reconstruction (described in section 2.4). Figure 2.5 shows single frame line-of-sight images obtained at the different frame rates as well as a mean image obtained by averaging the frames.

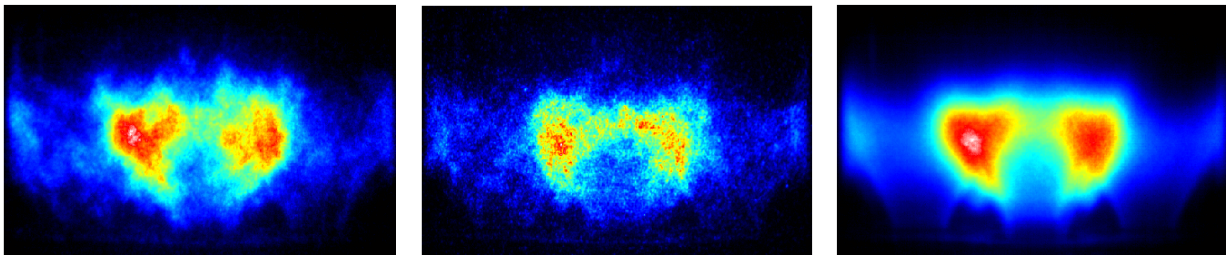

Figure 2.4. Line of sight images of multi–nozzle flame. (a) single frame captured at 2000 frames-per-second, (b) single frame captured at 4000 frames-per-second, (c) Mean Image

All the chemiluminescence images are presented in pseudo-color using the linear color bar shown in Figure 2.6 where black corresponds to zero intensity and white corresponds to the maximum intensity of a particular image.

Figure 2.5. Linear color bar for all chemiluminescence images.

2.2.3 Data Acquisition System

All measurements systems excluding the camera-intensifier system are controlled using a National Instruments PCI-6259 data acquisition board and BNC-2110 connector blocks. 16 consecutive

data sets, each consisting of a one second long recording obtained at a sampling rate (fs) of 8192 samples per second, are recorded at each test condition. When these signals are analyzed, they are split into the individual one second long sets (N = 8192 samples). This gives a frequency resolution (Δf) of one hertz. The data acquisition system is managed using the LabView software package. This provides the user interface that enables all the signals to be viewed in real time during tests using this system.

2.3 Data Processing and Analysis

2.3.1 Two-Microphone Method for Calculating Velocity Oscillations

In order to determine the flame transfer function (see Section 1.4.1), it is necessary to measure the time varying velocity in the nozzle, from which the amplitude and phase of the velocity fluctuation at the forcing frequency can be determined. There are a number of methods that can be used to measure the velocity fluctuation in the nozzle which include laser-based techniques such as laser doppler velocimetry (LDV) and particle image velocimetry (PIV), hot-wire and hot-film anemometry, and acoustic techniques such as the two-microphone method. Laser-velocimetry techniques are relatively complex and expensive, require optical access, and require the introduction of seed particles. Hot-wire or hot-film anemometry are effective methods to measure the velocity fluctuation because of the small probe size and fast response time. However, this is a point measurement i.e. it is dependent on the radial location within the nozzle. Furthermore, these probes are not designed to operate in the high inlet temperatures that are present in the nozzle. Since the velocity input of the flame transfer function (Equation # from chapter 1) is one-dimensional, the two-microphone method [93] is suitable to obtain the velocity fluctuation in the nozzle.

The derivation of the TMM method begins with a linearized form of Euler's equation shown in equation X. In order to use this form, incompressible, inviscid flow with negligible body forces are assumed.

$$\frac{\partial u}{\partial t} = -\frac{1}{\rho}\frac{\partial p}{\partial x} \tag{2.2}$$

Where u is particle velocity, t is time, ρ is mixture density, p is pressure, and x is the axial coordinate.

By applying a finite difference approximation to the pressure term and a Fourier transform to the entire equation, equation (1.5) is transformed into equation (1.5)

$$U \approx \frac{j}{\omega\rho\Delta x}(P_{DS} - P_{US}) \tag{2.3}$$

Where U is the linear spectrum of velocity, P_{DS} and P_{US} are the linear spectra of the pressure signals from the downstream and upstream piezoelectric pressure transducers respectively, ω is angular frequency, ρ is the mixture density, Δx is the spacing between the pressure transducers (fixed at 38 mm), and j is the imaginary unit. The resultant particle velocity linear spectrum is complex, containing both magnitude and phase information. Transformation back to the time domain is accomplished through an inverse Fourier transform. The TMM cannot be used to calculate the mean nozzle velocity since equation (1.5) is undefined for zero frequency.

The two microphone method is not accurate at all frequencies; there exists both a low frequency and high frequency limit. The high frequency limit is due to the finite difference approximation. The acoustic wavelength of the pressure perturbation depends on frequency i.e. the wavelength is longer for lower frequencies while the microphone spacing, Δx, is fixed. If the wavelength is on the order of the microphone spacing, or smaller, the measured pressure gradient will be incorrect [93]. The low frequency limit is due to the neglect of attenuation between the pressure transducers [94]. At low frequencies, the acoustic wavelength of the pressure perturbation is large and the measured pressure gradient between the upstream and downstream pressure transducers is small. Therefore, the errors associated with neglecting attenuation are large. Furthermore, the calculated particle velocity will be inaccurate if the magnitude of the pressure difference between the pressure transducers is comparable to the magnitude of pressure fluctuations associated with turbulence.

2.3.2 Forced Flame Data Analysis

Pressure, velocity, and chemiluminescence signals of the forced flames are measured as discrete time varying signals. These are then analyzed in the frequency domain to characterize the response at or near the forcing frequency. A Fast-Fourier transform given in equation (1.5) is used to calculate the signal's linear spectrum.

$$X_m = \sum_{n=0}^{N-1} x_n e^{-j2\pi \frac{nm}{N}} \Delta t \tag{2.4}$$

where X is the linear spectrum, x is the time domain signal, j is the imaginary unit, N is the number of data points, Δt is the time resolution (time increment between data points), and m and n are the frequency and time domain indices respectively. The linear spectrum, X, is a complex quantity and contains both amplitude and phase components of the time domain signal as a function of frequency.

The amplitude component of the time domain signal is obtained by calculating the single-sided power spectral density (G_{XX}) of the linear spectrum using equation (1.5).

$$G_{XX} = \begin{cases} \frac{1}{T}|X_m|^2 & for\ m = 0 \\ \frac{2}{T}|X_m|^2 & for\ 1 \leq m \leq N/2 - 1 \\ \frac{1}{T}|X_m|^2 & for\ m = \frac{N}{2} \end{cases} \tag{2.5}$$

Where T is the period of the time domain signal. The root mean square (RMS) amplitude of the time domain signal can be related to the single-sided power spectral density using Parseval's theorem, equation (1.5).

$$x_{rms} = \sqrt{\frac{1}{N}\sum_{n=0}^{N-1} x_n^2} = \sqrt{\sum_{m=0}^{N/2} G_{xx}(m)\Delta f} \tag{2.6}$$

Where Δf is the frequency resolution ($\Delta f = 1/T$). This form of Parseval's theorem calculates the RMS amplitude of the entire time domain signal or the integral of the single-sided power spectral density over all frequencies. Since our measurements are obtained at a distinct frequency i.e. the forcing frequency, a modified version of Parseval's theorem (equation (1.5)) is used to obtain the RMS amplitude at a single frequency.

$$x'_{rms}(f) = \sqrt{G_{xx}(f)\Delta f} \tag{2.7}$$

Here, the notation x'_{rms} denotes that this RMS value does not contain any mean information. The mean component is isolated using equation (2.8), where n is the frequency domain index.

$$x_{mean} = \sqrt{G_{xx}(0)\Delta n} \tag{2.8}$$

The phase component of the linear spectrum is determined from the angle between the real and imaginary component of the linear spectrum at the frequency of interest, equation (1.5).

$$x_{phase} = \tan^{-1}\left(\frac{X_{Im}}{X_{Re}}\right) \tag{2.9}$$

Where X_{Im} and X_{Re} are the imaginary and real parts of the linear spectrum respectively.

For the high speed chemiluminescence images, a mean, RMS and phase component can be calculated for all pixels and combined in matrices to obtain mean, RMS and phase images. Using these images a time series of 24 images that encompass a full forcing cycle is created using the equation (2.10) below.

$$\begin{aligned} Projection\ Image \\ = Mean\ Image + \sqrt{2}\ RMS\ Image * \cos(2\pi f t \\ + Phase\ Image) \end{aligned} \tag{2.10}$$

Where *f* is the forcing frequency and *t* is the time interval of a single forcing cycle divided into 24 increments. These 24 images are further processed as described in the sections below.

2.4 Three-Dimensional Image Reconstruction

2.4.1 Introduction and review of previous work

The literature reviewed in chapter 1 illustrates the importance of measurement techniques for characterizing flame structure in realistic combustor configurations. Optical techniques provide the best approach when compared to physical probes which are likely to disturb the local and overall flame and flow structure. Laser-based optical techniques can be implemented to make point, one-dimensional line, and two-dimensional planar measurements in a variety of combustion systems by systematically moving the measurement point, line or plane throughout the flame to map its 3-D structure. An alternative approach is to use the natural radiation emitted by the flame, referred to as flame luminosity, which includes thermal radiation emitted by high temperature gases or soot particles and chemiluminescence emission from electronically excited species in the flame's reaction zone. Luminosity measurements generally require less equipment and are simpler to implement than laser-based techniques. However, because flame radiation is emitted throughout the flame the detected signal is the sum of the radiation emitted along each line-of-sight and therefore is not spatially resolved. This limitation can be overcome using tomographic image

reconstruction techniques to reconstruct a 3-D image from a number of 2-D line-of-sight projection images.

The Inverse Radon Transform is a mathematical procedure widely used in tomographic image reconstruction [95]. It was first developed, along with the Radon Transform, by Johann Radon in 1917 [96, 97] as an integral transform for integrating a function over straight lines and planes. This mathematical operation has been improved on over time and is now used in many different applications of tomography such as medical imaging [98, 99], electron microscopy [100, 101] and seismology [102, 103].

To date there have been a number of studies involving the application of Inverse Radon Transform based three-dimensional tomographic reconstruction to flames [104, 105, 106, 107, 108, 109, 110, 111]. Most of the studies were performed on steady laminar flames where a limited number of line-of-sight luminosity measurements were used to reconstruct the three-dimensional luminosity distribution [104, 105, 106]. In laminar diffusion flames the luminosity is primarily thermal radiation from high temperature gases and soot particles. In this case it is also possible to determine the three-dimensional temperature field using two-color pyrometry [107]. The flames used in these studies were very nearly axisymmetric with little if any three-dimensional structure. More recently, this technique has also been applied to turbulent flames where the distribution of OH* chemiluminescence of non-premixed turbulent flames [108, 109], and the light intensity distribution of turbulent swirling flames [110] are studied. In addition to the Inverse Radon Transform, iterative tomographic reconstruction techniques such the Algebraic Reconstruction Technique (ART) [111, 112, 113, 114] and the Maximum Likelihood-Expectation Maximization (MLEM) [115, 116] as well as contour extraction methods [117, 118] have also been used to reconstruct 3-D images of flames. While iterative reconstruction methods yield better quality reconstructions with a fewer number of projection images compared to transform-based methods, they are more computationally intensive [98].

The current study differs from these previous studies in that tomographic reconstruction is applied to characterize complex three-dimensional flame geometries in both unforced and forced flames. The geometry of the combustor studied is representative of a commercial can combustor. This flame configuration exhibits complex 3-D flame structure (resulting from the flame-flame and flame-wall interactions that occur in this combustor configuration) which are not present in the various laboratory-scale multi-nozzle burners used in previous studies [112, 114].

Figure 2.7 shows two color photographs of the five-nozzle flame operating at fuel-lean premixed conditions, each from a different viewing angle. Figure 2.7a is an image of the flame recorded at a viewing angle of approximately thirty degrees above the horizontal plane and Figure 2.7b is an image of the five-nozzle flame from a position on the combustor centerline looking upstream into the combustor from the exhaust. These images show regions of significant flame-flame interaction and the complex asymmetric flame structure resulting from this interaction. The three-dimensional imaging technique described below provides the capability to characterize this complex flame geometry.

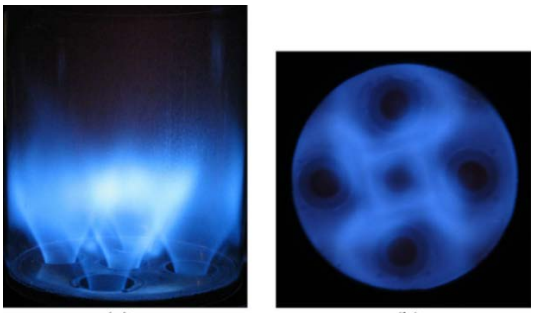

Figure 2.6. Color photographs of the five-nozzle flame viewed (a) from the side and (b) from the exhaust looking down into the combustor.

2.4.2 Multi-angle imaging setup

Figure 2.8 is a schematic drawing of the multi-angle imaging setup. The main component of the system is the camera-intensifier setup described in section 1.1.3. The camera is mounted on a dolly which moves along a 90° section of a 3.505 m diameter circular track. The track is secured to an optical table to ensure that the camera moves along a rigid and fixed plane which is positioned perpendicular to the centerline of the combustor.

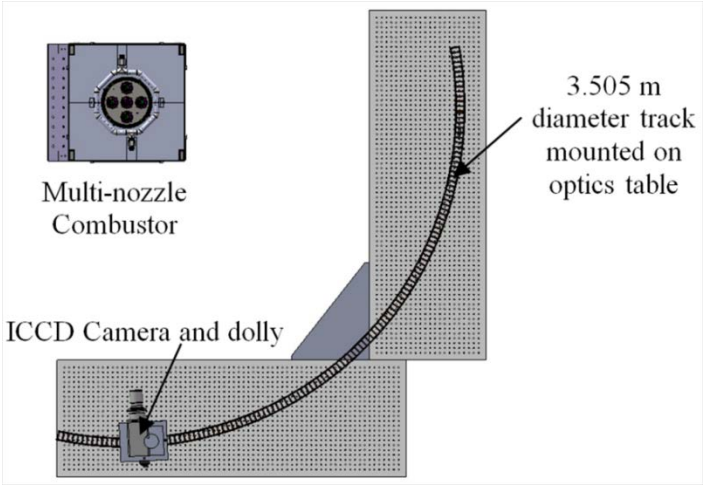

Figure 2.7. Schematic drawing of multi-angle imaging setup.

Camera views were calibrated by acquiring target images at each viewing angle of a 4.75 mm diameter by 36 mm long aluminum rod positioned at the center of the middle nozzle. The variation in camera alignment between viewing angles was determined by comparing the locations of the end of the rod (for variation in the vertical direction) and the location of the vertical centerline of the rod (for variation in the horizontal direction). The variation was found to be less than 10 pixels (or 5 mm) in the vertical direction and less than 6 pixels (or 3 mm) in the horizontal direction. The distances obtained for each viewing angle were used to shift the images as one of the first steps in the image processing to correct for the errors in camera views.

For the data set used to develop and validate the 3-D imaging technique, line-of-sight chemiluminescence images are acquired in equally spaced intervals of 2° around the 90° section

of track using the ICCD camera. Each image is the average of 10 frames acquired with a camera exposure time of 100ms. The result is a set of 46 projection images, each at a different viewing angle. Representative projection images are shown in Figure 2.9a for two viewing angles (0° and 44°) depicted in Figure 2.9b.

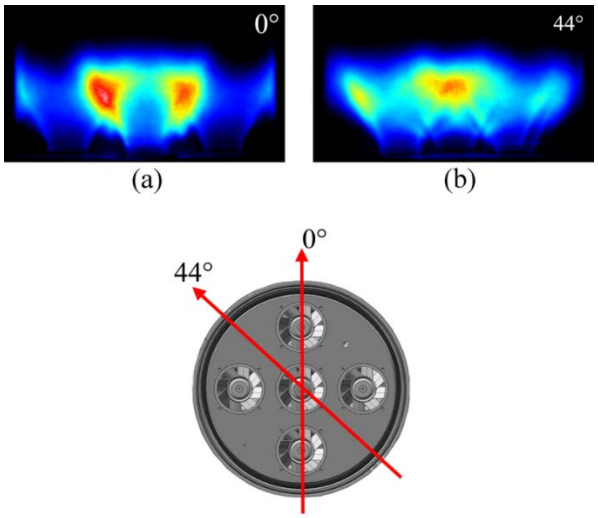

Figure 2.8. Unforced flame projection images from two different viewing angles 0° (a) and 44° (b).

2.4.3 Reconstruction Procedure

All projection images are shifted to correct for variations in the camera's field of view with changes in the viewing angle and then corrected for background, dark current and flat-field effects. Each projection image is then divided into single pixel wide horizontal bins as illustrated by the red lines in Figure 2.10a. These horizontal bins corresponding to a fixed axial position (z) in each of the N multi-angle projection images are combined into an N by W array, where W is the number of pixels along each of the horizontal bins. The multi-nozzle flames are assumed to display 90° symmetry. The fact that the downstream line-of-sight projection image in Figure 2.15b exhibits 90° symmetry verifies this assumption. Therefore, this array is repeated 3 more times to get a full 360° range of projection images resulting in a 4N by W array (Figure 2.10b).

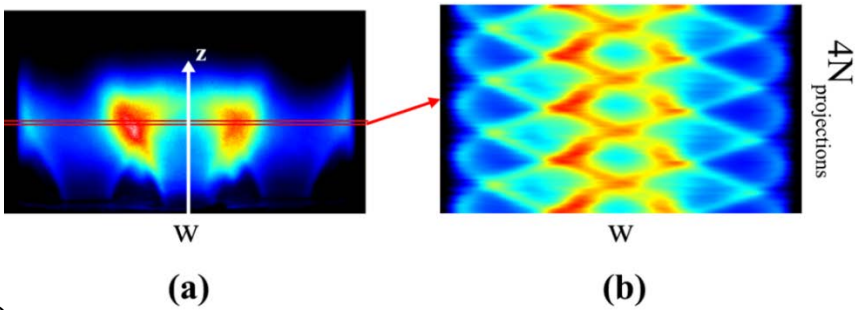

Figure 2.9. (a) Projection images showing a horizontal bin at location "z" and (b) Array of horizontal bins at location z from 4N projection images

A filtered back projection algorithm [119] is used to perform the Inverse Radon Transform on the array of multi-angle projection data (Figure 2.10b) corresponding to a specific axial position (z).

This yields a two-dimensional slice of the three-dimensional image, as illustrated in Figure 2.11. This process is repeated using the horizontal bins of pixels at each axial position (z), and the resulting two-dimensional slices are combined to produce a three-dimensional image. Two approaches for viewing the three-dimensional images were evaluated. The first method involves using a transparency map combined with the colormap (Figure 2.6) such that the opacity is proportional to the chemiluminescence intensity, i.e. high intensity regions are more opaque while low intensity regions are more transparent. The resultant three-dimensional image is shown in Figure 2.12a. The second method involved drawing a constant intensity surface in three-dimensions as shown in Figure 2.12b. While these three-dimensional visualizations provided useful qualitative validation to the accuracy of the reconstruction, neither one provided useful quantitative information of the flame's three-dimensional structure compared to two-dimensional slices of the three-dimensional flame structure (Figure 2.11)

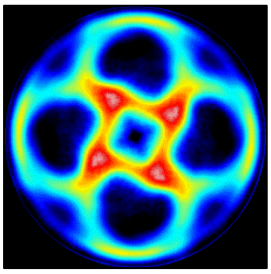

Figure 2.10. Two-dimensional slice oriented perpendicular to the combustor axis obtained from inverse radon transform.

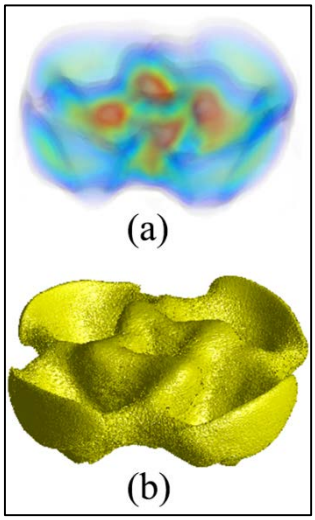

Figure 2.11. Visualization of the three-dimensional reconstruction of the five-nozzle flame.

Figure 2.13 shows a series of vertical slices of the reconstructed three-dimensional image. The results shown in this figure clearly illustrate the complex three-dimensional structure of this multi-nozzle flame, including the flame interaction regions and the effect of swirl on this interaction. The images show that the interaction between the swirl flows exiting each nozzle alters the swirl flow field surrounding each flame resulting in highly complex flame shapes. Therefore, one should not expect that a simple scaling argument could be used to predict the behavior of the five-nozzle flame from that of an equivalent single-nozzle flame.

Additional insight regarding the flame structure of the five-nozzle flame is provided by the sequence of horizontal slices shown in Figure 2.14. In the two-dimensional image closest to the

dump plane (Figure 2.14d) the center flame appears to be smaller in diameter than the outer flames, which suggests that the outer flames act to confine the center flame, thereby decreasing the flame angle at the base of the flame which can be observed in Figure 2.13c. This is also likely to lengthen the center flame, which will affect the center flame's response to acoustic velocity fluctuations. The outer flames also show evidence of flame-wall interaction which "flattens" the outer side of the flame. Moving further downstream (Figure 2.14c), the two-dimensional image shows four small circular regions of intense chemiluminescence intensity (corresponding to large rates of heat release) located in the region between adjacent outer flames and the center flame. These regions mark the base of the flame interaction regions. The next image (Figure 2.14b) lies in the center of the flame interaction region and shows the significant distortion of the flame resulting from the interaction of the counter clockwise swirling flows from each nozzle. The images also reveal the unexpected transition in the center flame from a circular flame geometry in Figure 2.14d and Figure 2.14c to a square flame geometry in Figure 2.14b and Figure 2.14a.

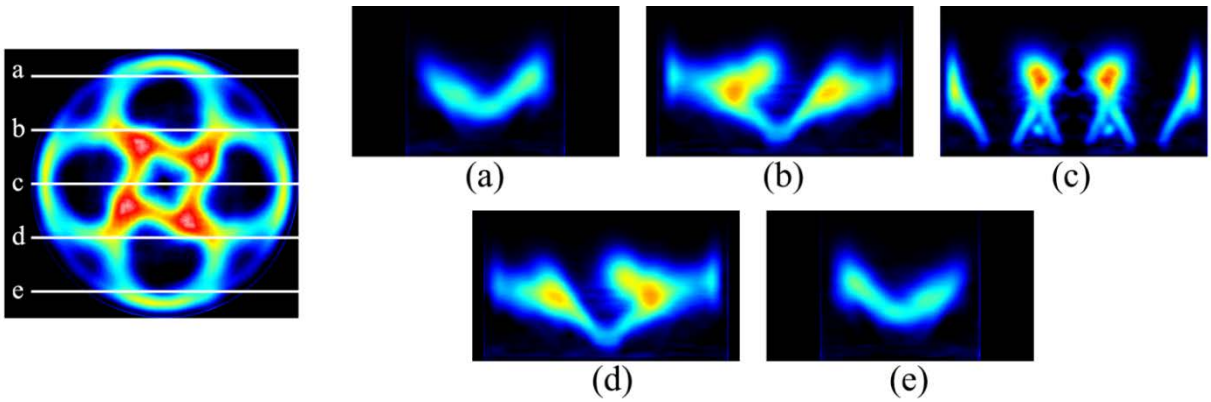

Figure 2.12. Vertical slices at the indicated locations: a, b, c, d and e.

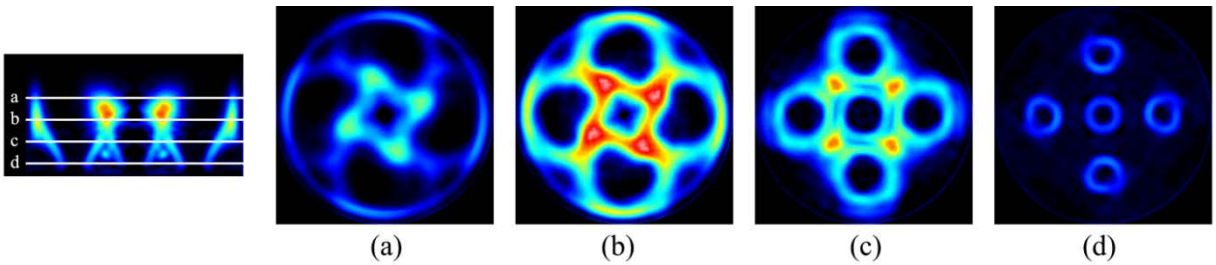

Figure 2.13. Horizontal slices at the indicated locations: a, b, c and d.

2.4.4 Reconstruction Accuracy

The accuracy of the three-dimensional reconstruction cannot be determined directly because the actual three-dimensional flame structure is unknown. Therefore an indirect assessment of the accuracy of the reconstruction was made by comparing projection images which were generated from the 3-D reconstruction to actual measured projection images. Figure 2.15 compares the reconstructed and measured projection images obtained by viewing into the combustor from downstream. Qualitatively, the reconstructed projection image (Figure 2.15a) include all of dominant features shown in the measured projection image (Figure 2.15b), giving confidence to the three-dimensional reconstruction results.

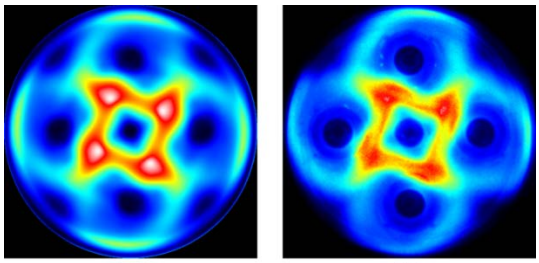

Figure 2.14. Comparison of reconstructed (a) and measured (b) downstream projection images.

The difference between the reconstructed and measured projection images can be quantified in terms of a 2-D correlation coefficient ($r_{2\text{-}D}$) defined using equation (1.5) and a 2-D agreement coefficient ($AC_{2\text{-}D}$) [120] defined in equation (2), where R_{mn} and M_{mn} are the matrices corresponding to the reconstructed and measured 2-D projection images, respectively, and $\bar{R}$ and $\bar{M}$ are the corresponding mean values. A value of $r_{2\text{-}D} = 1$ indicates perfect correlation between two images and $AC_{2\text{-}D} = 1$ indicates perfect agreement between the images.

$$r_{2-D} = \frac{\sum_m \sum_n (R_{mn} - \bar{R}) * (M_{mn} - \bar{M})}{\sqrt{\left[\sum_m \sum_n (R_{mn} - \bar{R})^2\right] * \left[\sum_m \sum_n (M_{mn} - \bar{M})^2\right]}} \tag{2.11}$$

$$AC_{2-D} = 1 - \frac{\sum_m \sum_n (R_{mn} - M_{mn})^2}{\sum_m \sum_n (|\bar{R} - \bar{M}| + |R_{mn} - \bar{R}|)(|\bar{R} - \bar{M}| + |M_{mn} - M|)} \tag{2.12}$$

The 2-D correlation coefficient for the downstream comparisons 0.9735 and the 2-D agreement coefficient for the downstream comparisons is 0.9032, which is further evidence of the accuracy of the three-dimensional reconstruction method employed. This agreement also supports the validity of the assumed 90° symmetry of the multi-nozzle flames.

2.4.5. Optimization

The quality and accuracy of the reconstruction is dependent on the number of projections [121], however, it is advantageous to minimize this number to reduce the time required to acquire and process the data used for the reconstruction. The effect of the number of viewing angles on the quality and accuracy of the three-dimensional reconstruction was investigated.

The 3-D unforced flame reconstruction used to obtain the two-dimensional slices shown in Figure 2.13and Figure 2.14 and the reconstructed downstream line-of-sight image shown in Figure 2.15a was based on 46 projection images acquired at 2° increments around the 90° section of track that encircles the combustor. Reconstructions have also been performed using every 2nd projection (23 projections in 4° increments), every 4th projection (11 projections in 8° increments), and every 8th projection (7 projections in 15° increments). The resulting three-dimensional reconstructions are qualitatively compared in terms of two-dimensional horizontal and vertical slices positioned at the locations indicated by the white lines in Figure 2.16. The results are presented in columns 2, 3 and 4 of Table 2.1. Discernible changes in the resulting images are observed as the number of measured projection images used in the reconstruction is reduced.

The 3-D correlation coefficient ($r_{3\text{-}D}$) defined in equation (2.13) and a 3-D agreement coefficient ($AC_{3\text{-}D}$) defined in equation (1.5) were used to quantitatively compare the entire three-dimensional reconstructions obtained for each of these cases relative to that obtained using all 46 projection images. A_{mno} and B_{mno} are two reconstructed 3-D image matrices which will be compared where A_{mno} is the matrix reconstructed using 46 projection images. As with the 2-D correlation coefficient, a value of $r_{3\text{-}D} = 1$ indicates perfect correlation between two images and $AC_{3\text{-}D} = 1$ indicates perfect agreement between the images.

$$r_{3-D} = \frac{\sum_m \sum_n \sum_o (A_{mno} - \bar{A}) * (B_{mno} - \bar{B})}{\sqrt{[\sum_m \sum_n \sum_o (A_{mno} - \bar{A})^2] * [\sum_m \sum_n \sum_o (B_{mno} - \bar{B})^2]}} \quad (2.13)$$

$$AC_{3-D} = 1 - \frac{\sum_m \sum_n \sum_o (A_{mno} - B_{mno})^2}{\sum_m \sum_n \sum_o (|\bar{A} - \bar{B}| + |A_{mno} - \bar{A}|)(|\bar{A} - \bar{B}| + |B_{mno} - \bar{B}|)} \quad (2.14)$$

This quantitative assessment is summarized in columns 5 and 6 of Table 2.1 and shows that there is a marked degradation in the three-dimensional reconstruction when the number of projections used is less than 11.

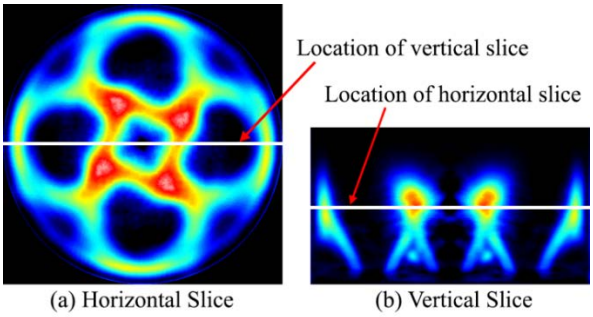

Figure 2.15. Two-dimensional horizontal (a) and vertical (b) slices of the three-dimensional reconstruction obtained using 46 projection images spaced every 2°.

The quality of the reconstruction obtained from a low number of projections can be improved by interpolating to a higher number of projections as illustrated by the data in the last row of Table 2.1 which is of 7 projection images interpolated to 46.

It is important to note that the number of projection images used to capture the details of the three-dimensional flame structure has an effect on the scale of the flame structures that can be observed. Unfortunately information on the number of projection images required for an accurate reconstruction is typically not available until after the three-dimensional flame structure is measured. Therefore it is necessary to take an initial three-dimensional flame structure measurement under typical conditions using a large number of viewing angles. Using this data, the minimum number of viewing angles can be determined.

Table 2.1. The effect of the number of projection images on the reconstruction results.

Number of Projections	Horizontal Slice	Enlarged View of Horizontal Slice	Vertical Slice	$r_{3\text{-}D}$	$AC_{3\text{-}D}$
46	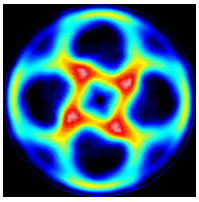	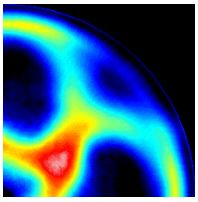	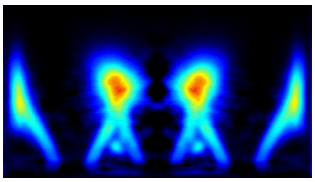	1.0000	1.0000
23	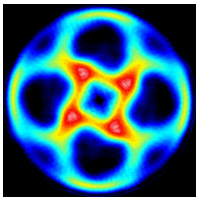	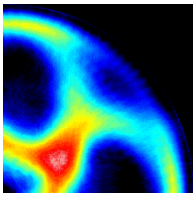	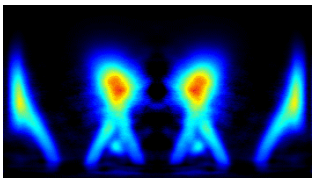	0.9978	0.9955
11	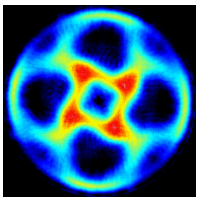	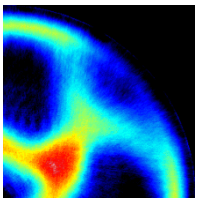	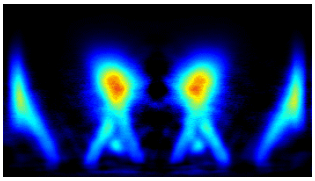	0.9866	0.9725
7	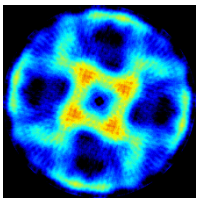	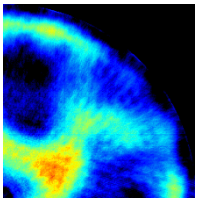	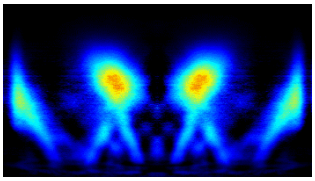	0.9308	0.8315
7 interpolated to 46	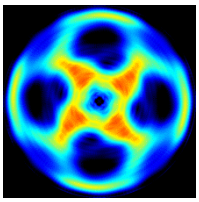	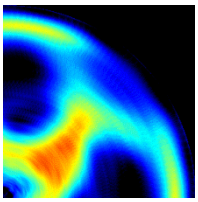	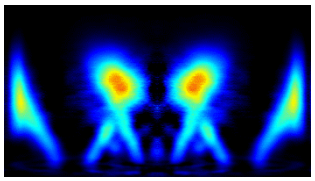	0.9744	0.9325

The images presented above show that the regions where adjoining flames interact have strong heat release rate compared with the rest of the flame indicating that these interaction regions could potentially play an important role in the flame dynamics. Knowledge of the spatial distribution of heat release rate is as important as temporal information in understanding the dynamics of multi-nozzle flames. 3-D images will aid in furthering our understanding of these phenomena since various regions of the flame can be isolated and studied independently. These images also provide further evidence that single-nozzle flame response data alone cannot be used for predicting multi-nozzle behavior.

3.0 Results

3.1. Operating conditions

The inlet parameters that can be varied in the multi-nozzle combustor described in Chapter 2 are: velocity, equivalence ratio, temperature of the reactants, fuel type and composition and fuel injection location. The forcing frequency and amplitude of the inlet velocity can be varied by adjusting the speed of the siren motor and the flow split between the siren and the bypass. While the system hardware (e.g. heater capacity, flow meter ranges etc.) place limitations the extent to which these parameters can be varied, a range of inlet conditions that the industrial nozzle used in the study is designed to operate at can be achieved. The only parameters that do not match a practical gas turbine combustor are fuel injection location (this study is conducted in fully premixed mode whereas most practical gas turbine combustors operate in technically premixed mode) and operating pressure (this experiment is conducted at atmospheric pressure).

Realistic gas turbine combustor pressures can be up to 20 atmospheres and since experimental data cannot be obtained at elevated pressures in the current test rig, a brief literature review on the effect of pressure on forced flame response is presented below. Flame transfer functions at high pressure and inlet temperature conditions were obtained by Cheung et al [1]. Their results showed that the transfer function gain curves were qualitatively similar at both low pressure (1.2 bar) and high pressure (15 bar) conditions. Discontinuities were observed in the transfer function phase curves at different frequencies for different pressures which were attributed to a shorter flame length at high pressures. Freitag et al. [2] acquired flame transfer functions at a fixed inlet velocities, temperatures, and equivalence ratios while varying the operating pressure from 1.1 to 5 bar. They too observed discontinuities in the FTF phase curves at higher pressures that were attributed to the change in location of highest heat release rate fluctuation. The results also showed that the FTF has a power law scaling with pressure which led the authors to conclude that by extrapolating low pressure FTF results, flame response at engine pressures could be described to an acceptable level. From the literature it is apparent that multi-nozzle flame response data will eventually be need to be obtained at elevated pressures. However, given the qualitative similarity in flame response at a range of pressures, it is likely that the flame response mechanisms identified in atmospheric tests will still persist at elevated pressure. The current study will aim to identify these mechanisms that future high pressure multi-nozzle flame response studies could use as a baseline.

In this study, the combustor is operated with a mixture of air and natural gas fuel at an inlet temperature of 200°C, an inlet velocity of 20 m/s and a fuel lean equivalence ratio of 0.6. Both unforced and forced measurements are obtained. For the forced measurements, the velocity of the fuel-air mixture was modulated at frequencies in the range of 100-400 Hz (in increments of 20 Hz) with RMS fluctuation amplitude (u'_{rms}/u_{mean}) of 10%. PMT data was obtained at all forcing frequencies. Image data of the forced flames were obtained at frequencies in the range 100-280 Hz.

3.2. Unforced multi-nozzle flame images and metrics

Images of the unforced flames are important because they represent the behavior of the flame when no thermo-acoustic instabilities are present within the combustor. The unforced flame images, at a given operating condition, represent a baseline against which forced flame images can be compared.

The literature reviewed in Section 1 show that a flame's response to velocity perturbations is a strong function of flame structure. Many studies on flame response have identified governing parameters which are aspects of flame structure such as flame length or flame angle [1, 2, 3, 4, 5]. The following sections attempt to characterize the flame structure of unforced and forced flames in the multi-nozzle combustor by defining a set of metrics to describe features of the flame's structure from the flame images. These metrics describe features of the flame shape (mean flame position and flame length) and the flow field (approximate shear layer locations and outer recirculation zone size)

As described in the section on 3-D imaging in Chapter 2, detailed information of the multi-nozzle flame structure can be obtained by investigating 2-D slices of the 3-D image of the multi-nozzle flame. Furthermore, the multi-nozzle flames can be isolated into three independent 3-D regions (indicated by constant intensity surfaces in Figure 3.1): the flame base (blue surface), the interaction region (red surface) and the outer half of a single outer flame (yellow surface). Isolating the flame base enables the effects of swirl on the flame response to be studied before any flame-flame or flame-wall interaction occurs. Analyzing individual slices of the outer half of a single outer flame provides data on the effect of both swirl and confinement on flame response. The region that encompasses the entire downstream section of the middle flame, and the downstream section of the inner regions of the outer flames experiences high amounts of flame-flame interaction and is thus called the interaction region.

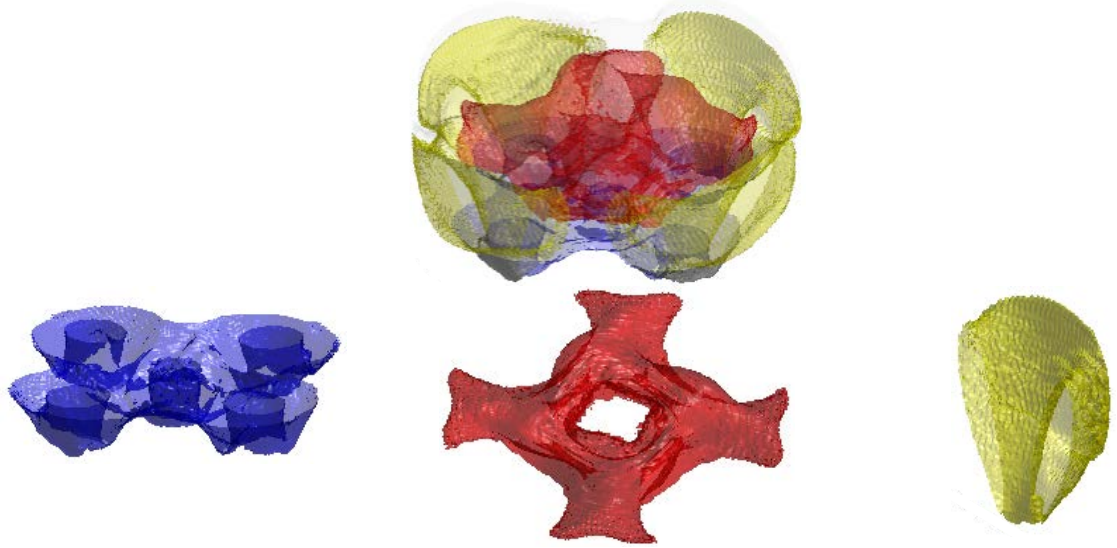

Figure 3.1. Division of multi-nozzle flame into 3-D regions: Flame base (blue), interaction region (red), and outer half of single outer flame (yellow)

The flame structure and interaction of adjacent swirl flames in this combustor configuration is not completely understood and therefore, only the image slices from the outer half of a single outer flame (yellow region in Figure 3.1) will be analyzed in this portion of the study. The only boundary experienced by the flame in this region is the combustor wall. The lower set of images in Figure 3.2 shows 2-D vertical slices around the circumference of the outer half of a single outer flame. The upper image of Figure 3.2 shows a horizontal slice of the multi-nozzle flame with the outer half of the outer flame isolated. The slices are labeled as an angle of rotation (θ_{rot}) in degrees

increasing in the direction of swirl. The slices that are unconfined are labeled as 0° and 180° and the slice that has the highest interaction with the wall is labeled as 90°.

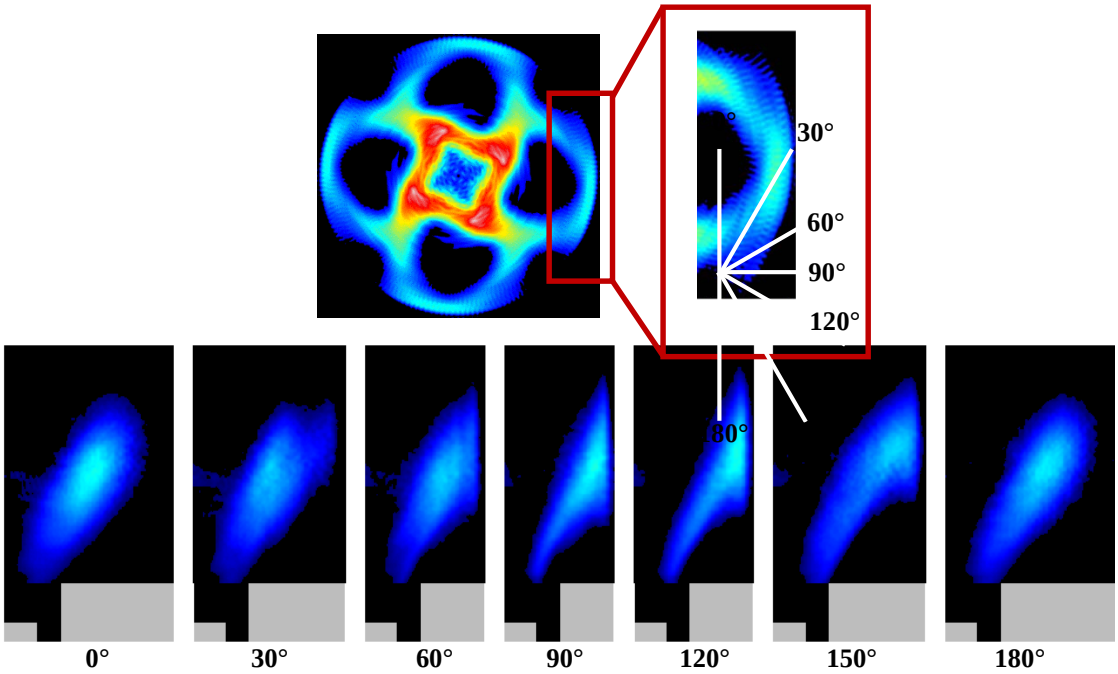

Figure 3.2. Two dimensional vertical slices of a single outer flame

The flame image slices illustrate that the structure of the outer flame varies as you move around the circumference. This is due to both the swirling flow field experienced by the flame and the fact that the flame experiences varying degrees of confinement (the effect of swirling flow and confinement on flame structure is discussed in section 1.2). The near-wall slices (θ_{rot} = 60° - 120°) display similar structure to previously studied confined single-nozzle V-shaped flames [1, 2, 3] and the slices in the range θ_{rot} = 0° - 30° and θ_{rot} = 150° - 180° show similar structure to previously observed swirl-stabilized unconfined flames [6, 7, 8]. The fact that different regions of the multi-nozzle flame exhibit varying flame structure is an indication that the response of a multi-nozzle flame cannot be fully predicted using only single nozzle flame response data.

The level of confinement experienced by the flame is quantified using a confinement ratio based on the combustor geometry. This method is limited to regions of the flame that only experience wall confinement (highlighted in yellow in Figure 3.3a). A clear boundary for the interaction zone between adjacent swirling flames cannot be simply defined. Therefore the confinement effect of adjacent flames will be a topic covered in the future work on flame-flame interactions. The confinement ratio (C) is defined as the ratio of the nozzle radius (r) and the distance to the nearest wall (d).

$$C(\theta) = \frac{r}{d(\theta_{rot})}$$

A plot of confinement ratio as a function of rotation angle (θ_{rot}) is shown in Figure 3.3b. The highest confinement ratio corresponds to the region of the flame that experiences the highest confinement, i.e. the flame is closest to the combustor wall (θ_{rot} = 90°).

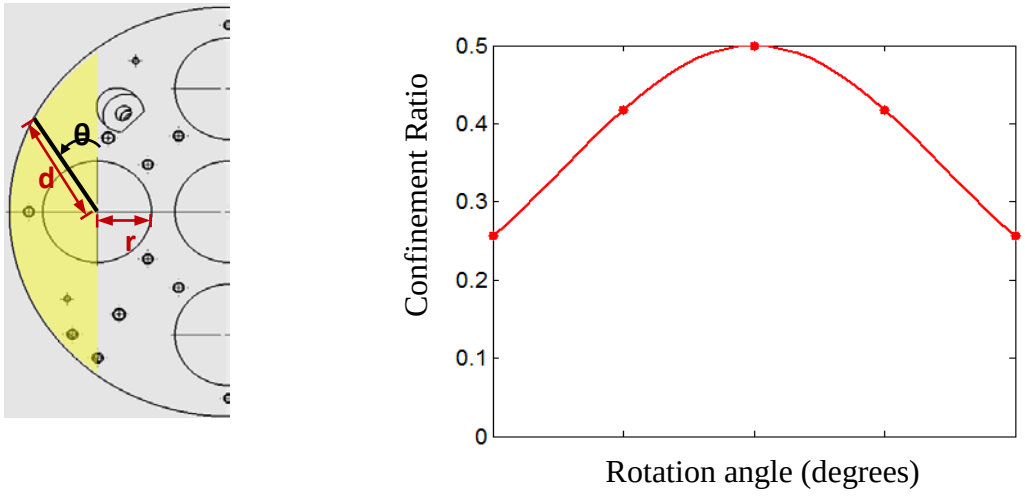

(a) **(b)**

Figure 3.3. (a) Dimensions used in calculation of confinement ratio and (b) Variation of confinement ratio with rotation angle θ

Another important observation from Figure 3.2 is that the flame is not symmetric i.e. the slices at θ_{rot} = 0°, 30°, 60° do not exhibit the same structure as θ_{rot} = 180°, 150°, 120° even though the confinement is the same. This is due to the swirling flow field in the combustor affecting the local flame stabilization locations as discussed in Section 1.2.

The flow in this experiment is highly turbulent (Re ≈ 30000 based on a hydraulic diameter). Therefore, the location of the reaction zone moves rapidly in space resulting in a time-averaged 'flame brush' that gives the appearance of a thick reaction zone [9]. This is illustrated in an image slice of the multi-nozzle outer flame that interacts with the combustor wall (Figure 3.4a). The approximate location of the flame sheet or the mean flame position is determined from the flame brush by finding the location of the pixel of maximum intensity row-wise in the flame image. Figure 3.4b shows an image of the flame brush with the mean flame position overlaid as a white line.

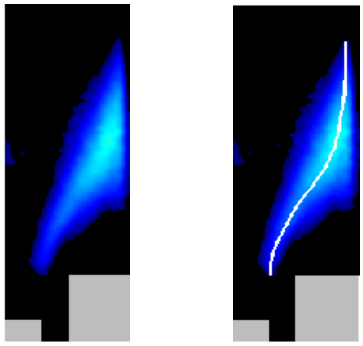

(a) **(b)**

Figure 3.4. (a) Flame brush of an unforced multi-nozzle outer flame slice (θ_{rot} = 90°) with (b) mean flame position overlaid

Figure 3.5 illustrates vertical slices around the circumference of the outer half of an outer flame with the mean flame position overlaid. As the flame gets more confined (rotation angles 60° - 120°), it is forced downstream along the combustor wall. The asymmetry in the flame (variation in flame structure at locations where confinement is the same) is apparent by the variation in the shape of the mean flame position curves around the circumference.

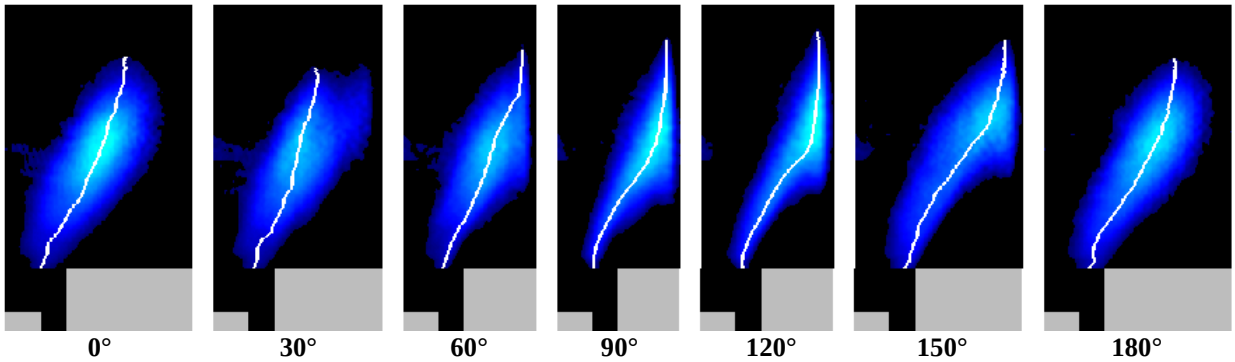

Figure 3.5. 2-D vertical slices of a single outer flame with mean flame position overlaid (angles below images represent rotation angle, θ_{rot})

A common metric used to quantify flame structure is flame length (L_f). In laminar conical flames, the characteristic flame length is typically the length of the flame from base to tip. In turbulent flames, especially those that interact with a boundary, the downstream "end" of the flame is not clearly defined. In this study, flame length is defined as the distance from the flame anchoring location to the region of the flame where a majority of the heat release occurs. Various methods can be used to obtain flame length from processed chemiluminescence images. They are:

1. Axial heat release profiles of line-of-sight images
2. Linear distance of flame anchoring location to maximum heat release location
3. Length of mean flame position curve from flame anchoring location to maximum heat release location

For the first approach, a line-of-sight image of the multi-nozzle flame is summed radially thus obtaining an axial heat release profile. The distance from the axial location of the highest intensity to the flame anchoring location (centerbody edge) is defined as the flame length (Figure 3.6). This method yields a single flame length value for the entire multi-nozzle flame, therefore not accounting for variation in flame length between the middle and outer flames and around the circumference of a single flame. Hence this calculation is utilized when only line-of-sight data is available.

The spatial variation of the flame length can be accounted for by calculating the flame length using axial heat release profiles of 2-D flame image slices obtained from a reconstructed 3-D image). However, this method only accounts for change in flame length in a single dimension (the axial direction). The change in flame length in both the axial and radial direction is considered in approaches 2 and 3.

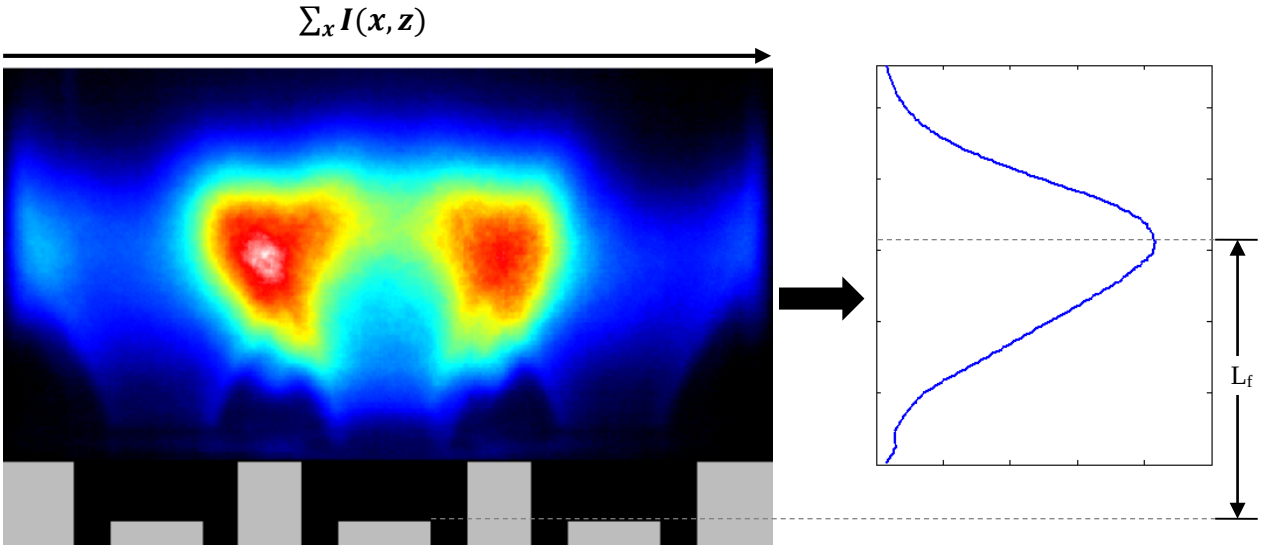

Figure 3.6. Calculating axial flame length from a line-of-sight image

Both approaches 2 and 3 mentioned above use the center of heat release as a marker of the downstream edge of the flame brush. To obtain the center of heat release, a set of pixels are isolated from a 2-D image slice based on intensity value (all pixels with intensity values of over 90% of the maximum intensity are isolated). The centroid of this area is then found.

In approach 2, the distance from the centroid of highest heat release to the flame attachment point (edge of the centerbody for the flames studied) is then taken as the flame length (Figure 3.7a). This approach for obtaining flame length makes the assumption that the flame brush is linear i.e. ignores its curvature and therefore underestimates the actual flame length. Previous studies redefine flame length by multiplying the measured flame length by a constant factor which is dependent on the flame shape in an attempt to account for this limitation e.g. Kim et al [9] used twice the linear distance from the centerbody edge to the location of maximum heat release as the flame length when studying v-shaped flames. In this study, this assumption is eliminated by approach 3 which redefines flame length as the length of the mean flame position curve (white curve) from the edge of the centerbody to the centroid of the region of 90% of the maximum heat release (black contour) as illustrated in Figure 3.7b. The root of the flame (between the centerbody and the dump plane) is not captured in the cameras field-of-view and therefore, the flame brush is assumed to be linear in this region.

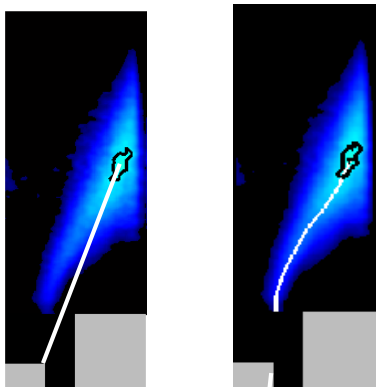

(a) **(b)**

Figure 3.7. Flame length obtained using 2-D flame image slices (θ_{rot} = 90°)

Care must be exhibited with approach 3 however, as two (or more) distinct regions of high heat release may exist in a flame brush which would result in an erroneous mean flame position profile and hence an inaccurate flame length. This is observed in flames that display an M-shaped structure such the vertical slice shown in Figure 3.8a which shows a part of a single outer flame that interacts with the middle flame (corresponds to θ_{rot} = 270°) with the mean flame position curve overlaid in black. To correct this error, the regions not associated with the main flame brush are zeroed out before calculating flame length (Figure 3.8b).It is evident that this sufficiently corrects the mean flame position curve to obtain a more accurate flame length.

Of all the methods described above, the mean flame position-based approach (approach 3) is the only one that can account for large scale wrinkling of a flame undergoing forcing. Therefore, it will be used to calculate flame length throughout this study.

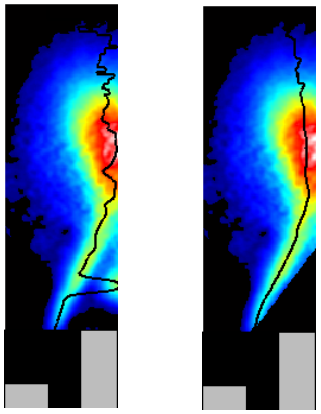

Figure 3.8. Vertical slice of an M-shaped flame with erroneous mean flame position overlaid in black (left) and corrected image and mean flame position (right)

Figure 3.9 shows the outer flame slices with regions of highest (top 10%) heat release (within black contour) and the mean flame position (white curve) used to calculate the flame length overlaid. An increase in flame length is observed as the flame gets more confined (θ_{rot} = 45° - 90°) by the combustor wall. While the flame length is expected to decrease as confinement reduces (θ_{rot} = 90° - 150°), it continues to increase; an indication that confinement is not the only governing parameter of the flame structure of these outer flames. This result is illustrated in the plot of flame length and confinement ratio as a function of rotation angle in Figure 3.10. The increase in flame length occurs in the direction of swirl which is an indication that the swirling flow field in the combustor affects the flame structure in addition to confinement.

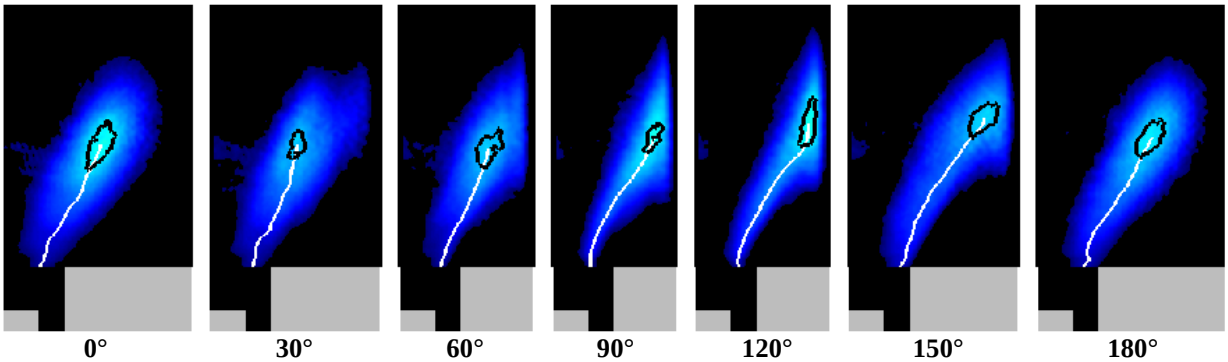

Figure 3.9. 2-D vertical slices of a single outer flame with flame length location overlaid (angles below images represent rotation angle, θ_{rot})

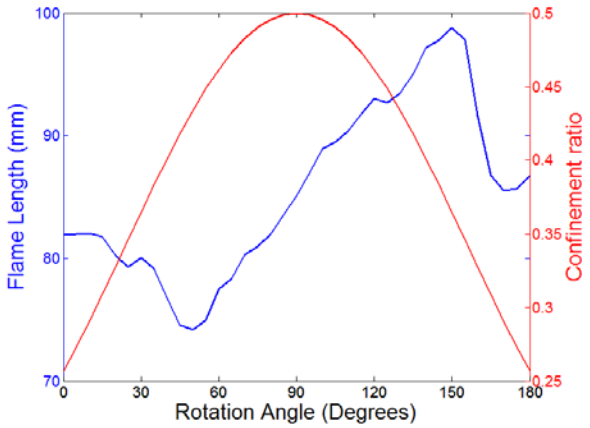

Figure 3.10. Flame length (blue) and confinement ratio (red) of the outer flame slices as a function of rotation angle

In the absence of flow field measurements, the locations of shear layers and recirculation zones are approximated based on the mean flame position and size of the flame brush. The flame slices studied in the range of interest (outer half of a single outer flame) all exhibit a V-shaped flame structure. The discussion on flame shapes in section 1.2 reveals that V-shaped flames stabilize on the inner shear layer of a swirling flow field. Therefore, the location of the inner shear layer (ISL) is approximated to be along the mean flame position. Flow field measurements in a reacting swirling v-shaped flame stabilized on a centerbody show that the outer shear layer (OSL) assumes a similar shape to the ISL and originates from the edge of the nozzle [13]. Therefore the location of the outer shear layer is approximated as the mean flame position offset by the annular distance *(nozzle radius - centerbody radius)*. The approximated outer shear layer ends at the axial location where the flame 'flattens' out as this is an indication of the beginning of flow recirculation. The approximated inner shear layer is assumed to extend axially till the flame tip although this cannot be confirmed without flow field measurements. The flame slices studied in the range of interest (outer half of a single outer flame) with the shear layers overlaid are illustrated in Figure 3.11. In each image in the figure, the white line on the left denotes the ISL location and the white line on the right denotes the OSL location.

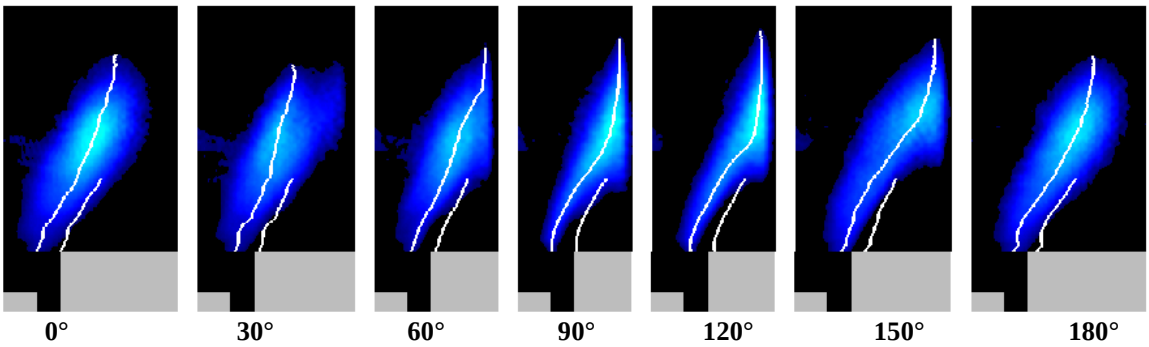

Figure 3.11. 2-D vertical slices of a single outer flame with inner and outer shear layer locations overlaid (angles below images represent rotation angle, θ_{rot})

Using the location of the outer shear layer and extending it along the edge of the flame, the outer recirculation zone (ORZ) can be approximated. The area of the ORZ (cross-hatched areas in Figure 3.12) is calculated by summing the number of pixels within this region. While this method does not accurately determine the size of the recirculation zone, it is sufficient to gather trends on the change of recirculation zone size with varying inlet conditions and confinement.

The areas of the recirculation zones in the rotation angle range 30° - 150° (θ_{rot} = 0° and 180° slices are unconfined and therefore do not have an ORZ) are plotted as a function of rotation angle and compared to the confinement ratio in Figure 3.13. A review of research on flows over a backward facing step conducted by Eaton and Johnston [11] shows that the reattachment length (the distance from the step to the location where flow recirculation zone begins) is proportional to the expansion ratio (inverse of the confinement ratio defined here). This would result in a larger recirculation zone over the backward facing step for smaller confinement ratios. The area of the recirculation zone shows an inverse dependence to confinement as is expected, even though the flame length shows no dependence on confinement due to the effect of swirl on the flame structure.

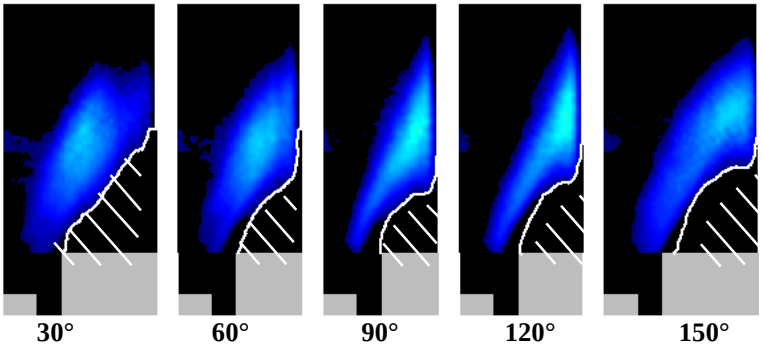

Figure 3.12. 2-D vertical slices of a single outer flame with outer recirculation zone overlaid (angles below images represent rotation angle, θ_{rot})

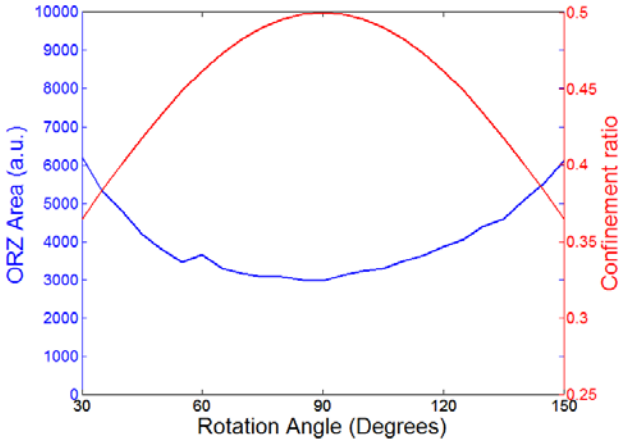

Figure 3.13. Area of outer recirculation zone and confinement ratio as a function of rotation angle

3.3. Forced multi-nozzle flame data

Forced flame data of the multi-nozzle flame was obtained at the same inlet conditions as the unforced data. The incoming fuel-air mixture was modulated with an RMS amplitude of 10% at

frequencies in the range 100-400 Hz in 20 Hz increments. Of these frequencies, image data was obtained at certain conditions in the frequency range 100-280 Hz.

3.3.1. Global flame response data

A global flame transfer function of the multi-nozzle flame at the inlet conditions described in section 3.1 was obtained using a photomultiplier tube for the heat release rate measurement. As mentioned in section 1.4.1, the flame transfer function is a complex quantity and thus has both a magnitude and a phase component. The FTF gain and phase plots are illustrated in Figure 3.14 Error bars on each data point of the plots represent +/- one standard deviation of 16 samples. The gain plot exhibits qualitatively similar behavior of alternating minima and maxima seen previously in single- and multi-nozzle studies reviewed in section 1.5. Inflections in the phase near the gain minima are also observed which is consistent with the trends of previously studied flame transfer function data of turbulent, premixed, swirl-stabilized single- and multi-nozzle flames. The large phase inflection at 320 Hz is an artifact of the phase being wrapped to the range -360° to 0°.

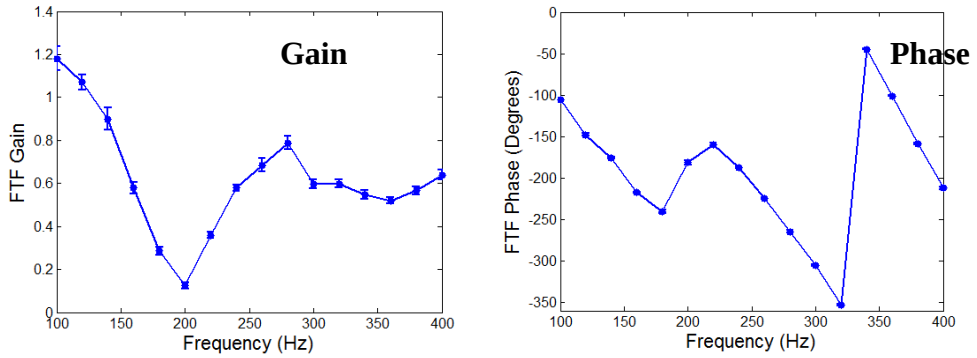

Figure 3.14. Global flame transfer function gain and phase curves of multi-nozzle flame obtained from PMT data

3-D Image data was obtained at ten forcing frequencies over the frequency range from the initial high gain condition (100 Hz) and a local maximum gain (280 Hz) and the corresponding gain and phase plots are illustrated in Figure 3.15. The blue markers correspond to global heat release rate measurements obtained from the PMT and the red lines and markers correspond to global heat release rate measurements obtained by summing the pixels of a reconstructed 3-D image. As mentioned above, the error bars on each data point of the plots represent +/- one standard deviation of 16 data sets. The standard deviation of the data points obtained from the summed 3-D image are based solely on the variation in the velocity data since only a single time series of heat release data is obtained from the 3-D image reconstruction. The plots show good agreement between PMT data and reconstructed 3-D data giving further validation to the quality of the 3-D reconstruction.

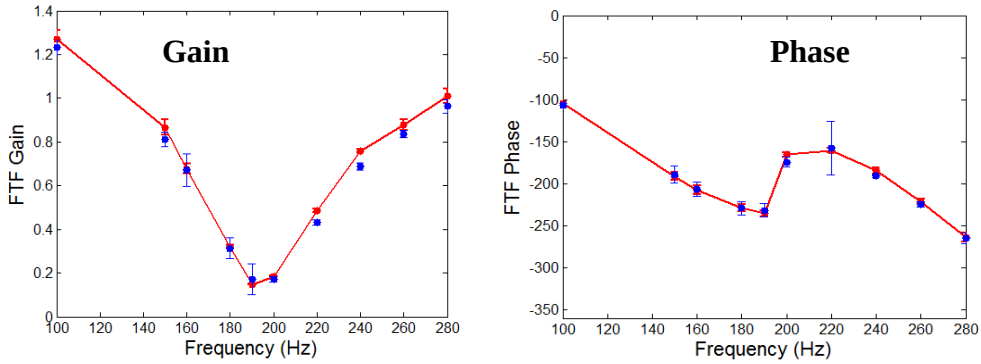

Figure 3.15. Global flame transfer function gain and phase curves of multi-nozzle flame obtained from flame images (red lines and markers) and PMT (blue markers)

3.3.2. Forced Flame images

Using the image processing technique described in chapter 2 (section 2.4), a time series of twenty-four 3-D images is generated corresponding to one forcing period. As with the unforced flame data, the analysis will be limited to the outer half of a single outer flame. The nomenclature used to label these images is the same as for the unforced multi-nozzle flame images.

Figure 3.16 shows the slices of the outer half of a single outer flame within a single forcing cycle (forcing frequency is 190 Hz which corresponds to a minimum overall FTF gain). Six images within a forcing period (in 60° phase angle increments) are shown for the range of rotation angles considered for the unforced flames. It can be seen that in the more confined flame slices (θ_{rot} = 60° to 120°), the flame interacts with the wall and is forced to propagate both upstream and downstream of the interaction location. The less confined flame slices fluctuate more freely as seen in the slices at θ_{rot} = 0° and 180°.

From Figure 3.16 it is evident that there are fluctuations in the position and structure of the flame within a forcing cycle, but these are difficult to resolve. These spatially-resolved heat release rate fluctuations can be identified by determining the RMS magnitude and phase of each pixel in an image (this method has also previously been used by Freitag et al. [2]). Figure 3.17 and Figure 3.18 show magnitude and phase images of vertical image slices of the outer half of a single outer flame (Figure 3.2). In each image, a mask is applied to pixels with intensity less than five percent of the maximum intensity of the mean image. The white line overlaid in each image denotes the averaged mean flame position (Figure 3.4) of all 24 image slices within a forcing cycle and the red plus sign denotes the mean location of the center of heat release in the flame brush within a forcing cycle.

Three forcing frequencies are investigated: a low frequency, high FTF gain (100 Hz), a FTF gain minimum (190 Hz), and an FTF gain maximum (280 Hz). The magnitude of each pixel is determined using the single-sided power spectral density described in section # in chapter 2 and the phase of each pixel is referenced to the peak in velocity oscillation obtained by the two-microphone measurement.

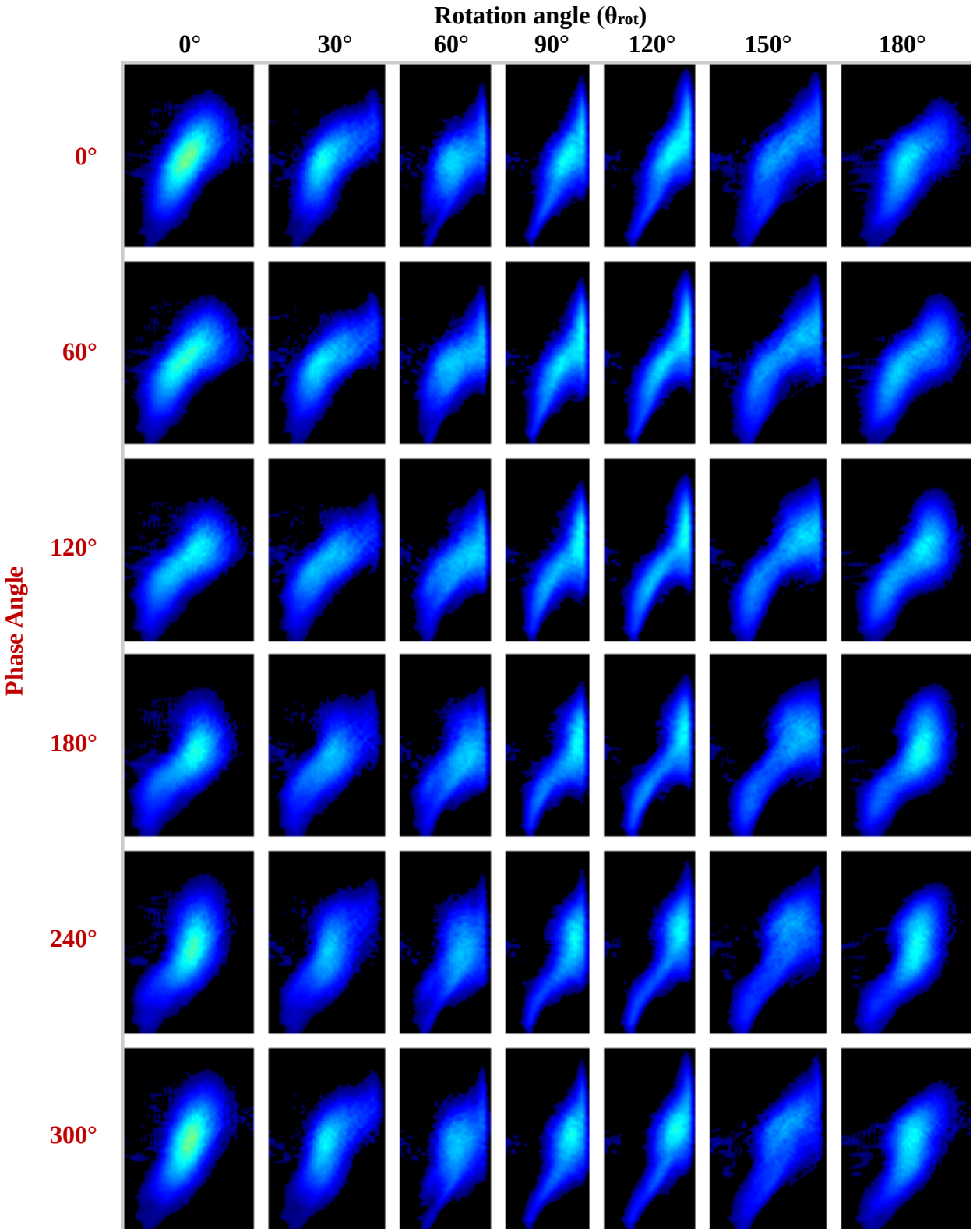

Figure 3.16. Images outer flame slices of the outer half of a single outer multi-nozzle flame forced at 190 Hz.

The RMS magnitude images in Figure 3.17 show that the regions of very low heat release rate fluctuation (which show up as a dark blue/black line along the flame brush) correspond to the location of the average mean flame position curve (white line). This validates the methodology used to determine the mean flame position because by definition, the mean position of the flame should correspond to the location of zero heat release fluctuation. In addition, the regions of highest heat release rate fluctuation (orange and red regions in the magnitude image) do not correspond to the center of heat release (red plus sign). While the center of heat release captures the location of maximum heat release, it does not coincide with the location of maximum heat release fluctuation. This result indicates that analyses that are based on a single point metric that describes flame structure may be incorrect as they do not capture the regions of highest heat release rate fluctuation. Finally, at the gain minimum frequency, the regions of largest heat release rate fluctuation are spread out through the flame brush while at the high gain conditions, the regions are concentrated to relatively small localized regions in the downstream portion of the flame.

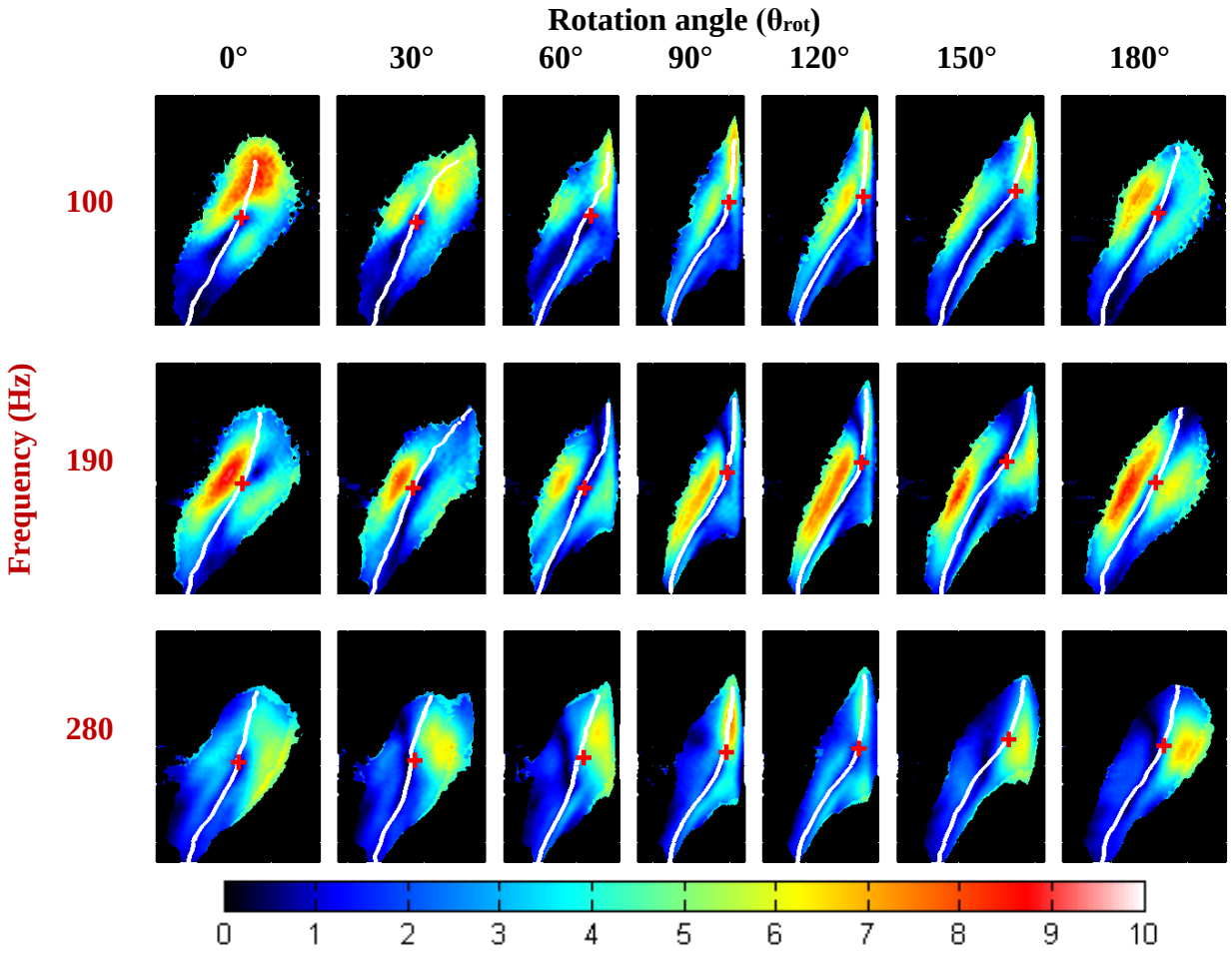

Figure 3.17. RMS magnitude images of the outer flame slices of the outer half of a single outer multi-nozzle flame forced at three frequencies

The phase images in Figure 3.18 illustrate that the flame response is not purely acoustic in nature. If the flame only responded to the inlet acoustic oscillations, the phase values of the pixels in each image would only vary by a few degrees and the phase images would appear to be similar at all frequencies investigated. Even at the highest frequency investigated (280 Hz), the wavelength of the acoustic oscillation is much larger than the flame length (see calculation in Appendix A), the flame is acoustically compact, and therefore would respond in bulk to the acoustic oscillation. The fact that variation in phase within a flame brush is observed indicates that a shorter wavelength convective disturbance propagating along the flame sheet produces local oscillations in heat release rate.

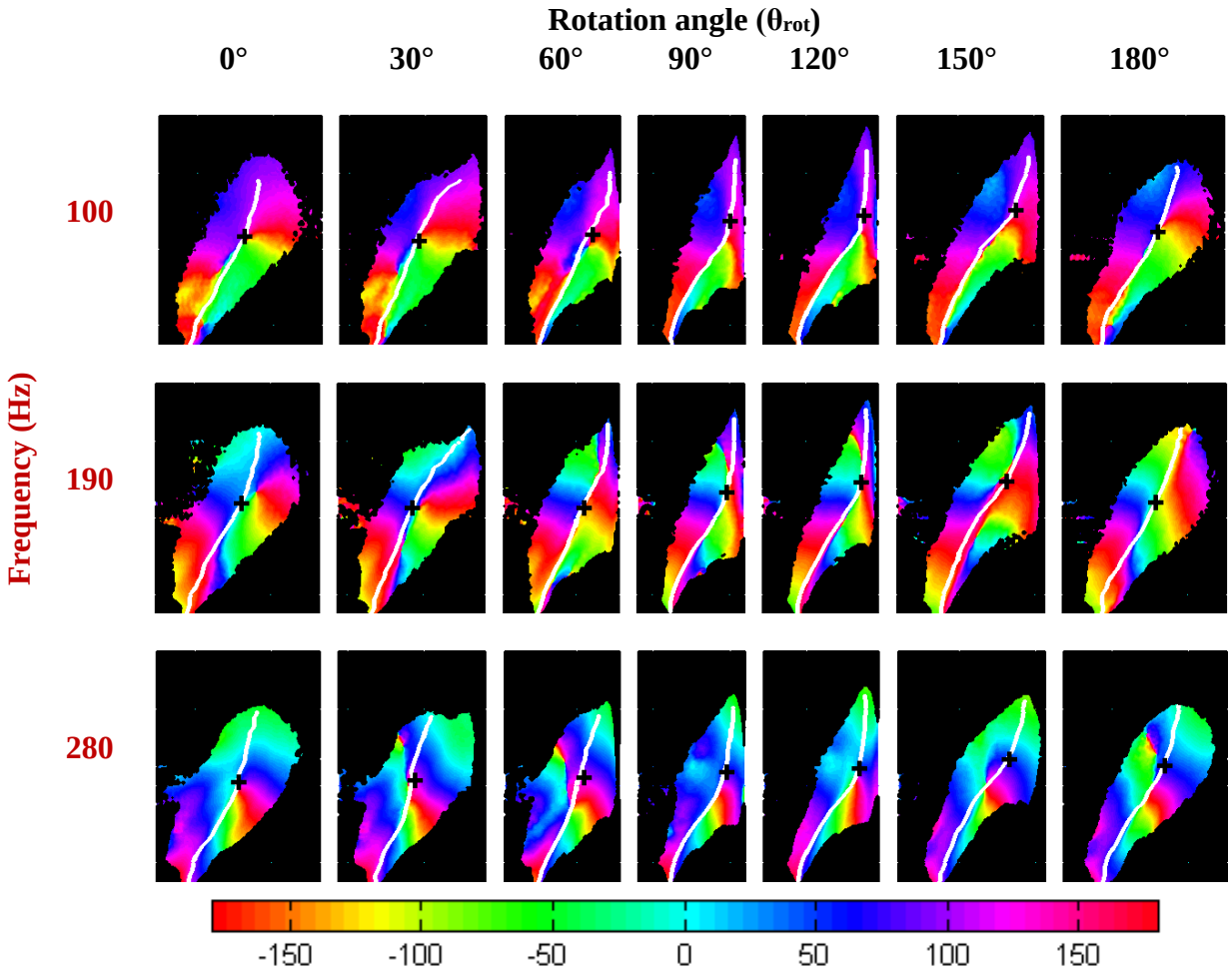

Figure 3.18. Phase images of the outer flame slices of the outer half of a single outer multi-nozzle flame forced at three frequencies

3.3.3. Local flame transfer functions

In section 3.2, it was shown that the three-dimensional image of the multi-nozzle flame can be isolated into three 3-D regions: the flame base, interaction region and the outer half of a single outer flame (Figure 3.1). The global heat release rate of these regions are obtained by summing the intensity of all pixels within each region. Flame transfer functions based on the global heat release rate fluctuation of each region and the inlet velocity fluctuations are obtained using

equation 1.6 in chapter 1. The flame transfer function gain and phase plots of the three regions and the entire flame (summed pixel intensity of entire 3-D image) are shown in Figure 3.19. At and near the gain minimum frequency of 190 Hz, it can be seen that the gain of all four regions are similar while at the other frequenices, the interaction region dominates the flame response. There exists a constant phase difference of 140° between the flame base and the other regions from the initial high gain (100 Hz) to the minimum gain (190 Hz) conditions. At the higher frequencies, the phase difference between the flame base and other regions is small (less than 30°).

Another observation is that the interaction region and outer half of the outer flame are in phase with the global heat release at the high gain conditions (100-160 and 220-280 Hz) whereas at the minimum gain conditions (180-200 Hz), the phase of the two regions varies with respect to each other as well as the global FTF phase. This is an indication that out of phase behavior in these regions cause destructive interference leading to reduced FTF gain.

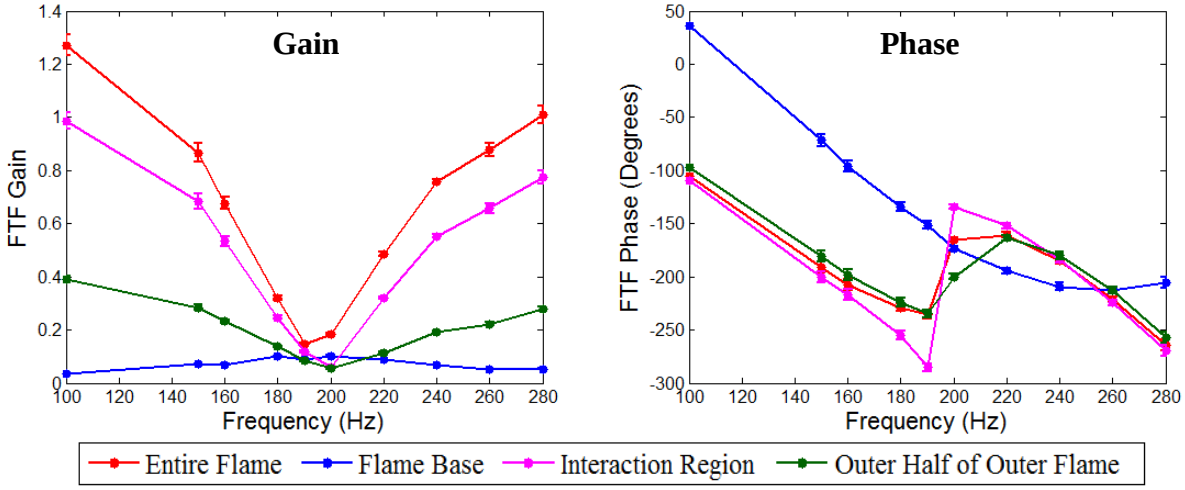

Figure 3.19. Flame transfer function gain and phase curves of three-dimensional regions of multi-nozzle flame

To further understand the flame response mechanisms in the outer half of the outer flame, transfer functions of the flame slices illustrated in Figure 3.2 are obtained. As with the 3-D regions discussed previously, the heat release rate of each flame slice is obtained by summing the intensity of all pixels in the slice and the flame transfer function for each region is calculated using equation 1.6. FTF gain and phase plots are illustrated in Figure 3.20. While the plots look qualitatively similar, the frequency of the gain minimum varies around the circumference. This trend is illustrated in Figure 3.21 where it can be seen that the FTF gain minimum frequency increases with increasing confinement.

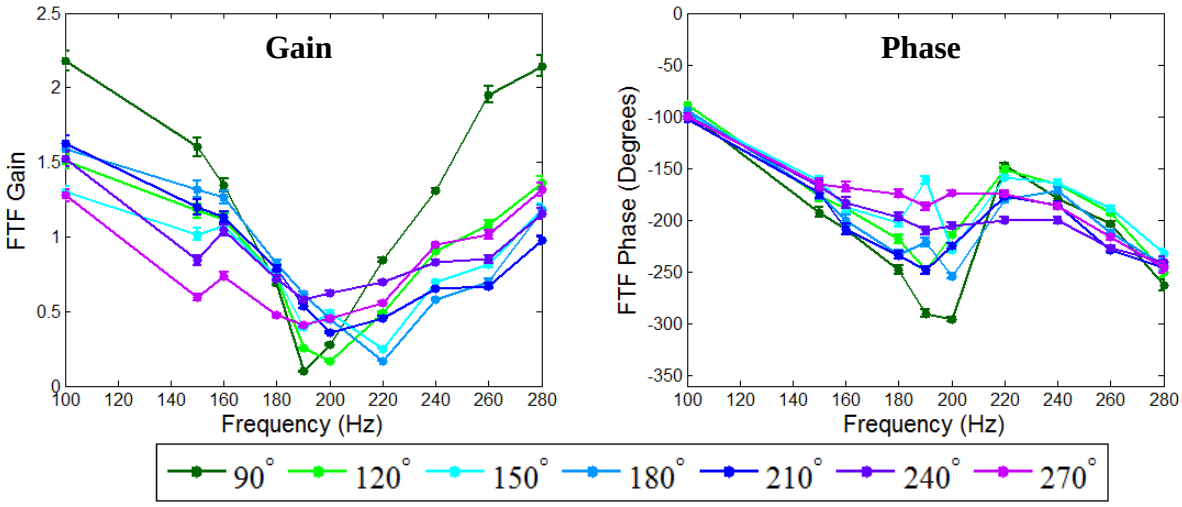

Figure 3.20. Flame transfer function gain and phase curves of two-dimensional slices of the outer half of a single outer flame

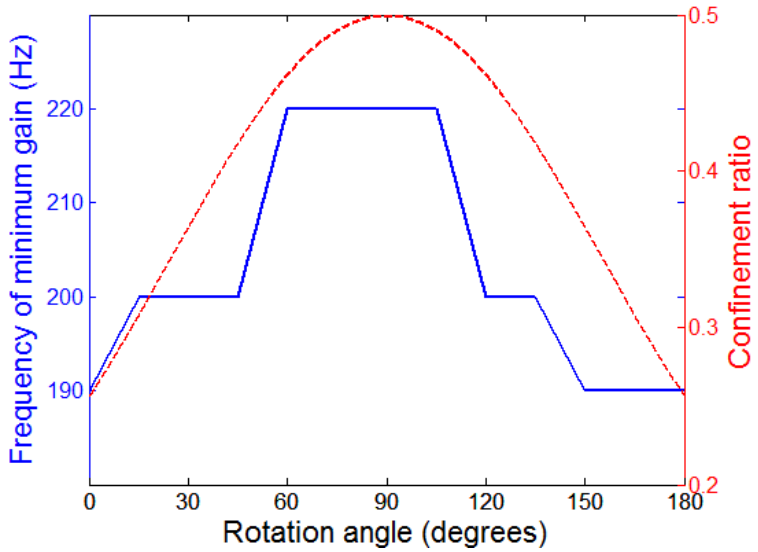

Figure 3.21. Variation of gain minimum frequency and confinement as a function of rotation angle

A non-dimensional parameter commonly used to generalize flame transfer function data [3, 4, 15] is the Strouhal number defined as $St = fL/U$ where f is the forcing frequency, L is a characteristic length scale (flame length in this case) and U is the velocity of the fluid. This definition of Strouhal number stems from the physical basis of a single convective velocity fluctuation perturbing the flame. The investigations cited above all show that both the FTF gain and phase curves collapse at low frequencies all the way to the gain minimum frequencies. Attempting to generalize the FTF gain and phase curves of the outer half of a single outer flame (Figure 3.20) using the Strouhal number proves to be unsuccessful as illustrated in Figure 3.22.

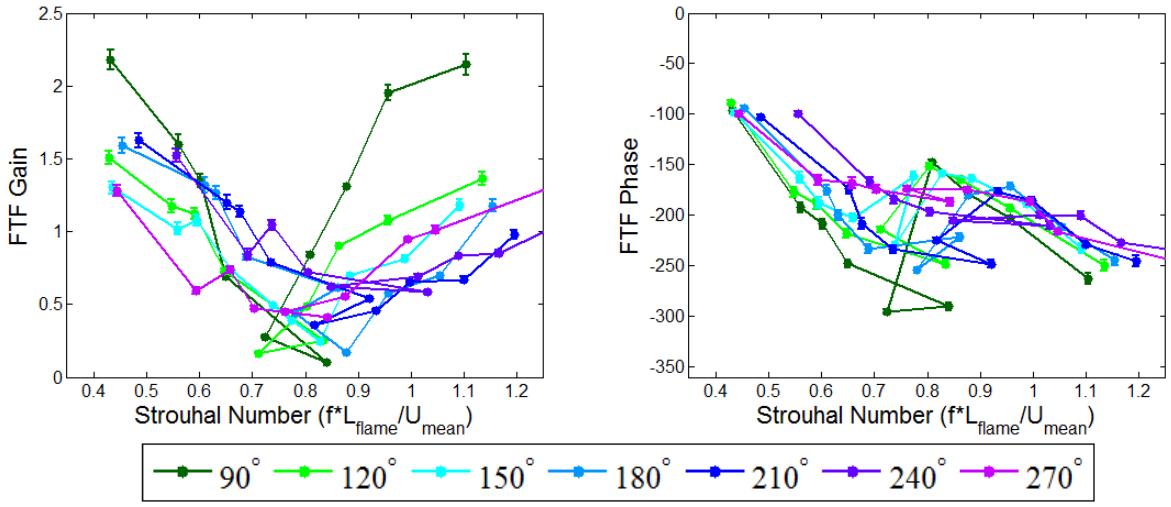

Figure 3.22. Flame transfer function gain and phase curves of two-dimensional slices of the outer half of a single outer flame as a function of Strouhal number

At the gain minimum condition, this behavior is explained by the fact that while the gain minimum frequency of each 2-D slice scales with confinement (Figure 3.21), the characteristic length parameter used i.e. flame length does not (Figure 3.10). This is a further indication that more than one convective mechanism is responsible for the flame response in this region.

3.3.4. Forced flame image metrics

The metrics described for unforced flames in section 3.2 can also be applied to the forced flame images. This portion of the study will only focus on analyzing the variation of mean flame position in forced flames. Figure 3.23a shows a time averaged 2-D image slice of a flame forced at 190 Hz with the mean flame position at twenty-four different phase angles of a forcing cycle overlaid. Figure 3.23b shows the envelope of mean flame positions presented in Figure 3.23a.

The width of the envelope of the mean flame positions is a measure of the extent or magnitude of the fluctuation of the mean flame position during a forcing cycle. In previous work using a single-injector version of the multi-injector combustor it was found that the magnitude of the fluctuation of the mean flame position is related to the magnitude of the fluctuation of the flame's overall rate of heat release [15]. Applying this same measurement to one of the outer flames in the multi-nozzle combustor gave the results presented in Figure 3.24. Because this flame is not axisymmetric, results are shown at 7 different positions around the circumference of the injector. There is a noticeable decrease in the magnitude of the fluctuation of the mean flame position as the confinement increases.

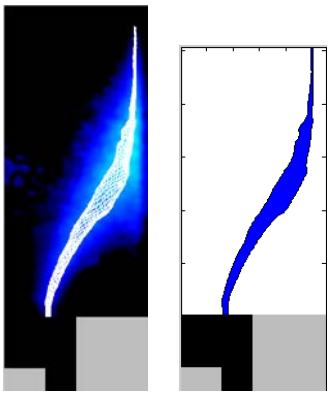

(a) **(b)**

Figure 3.23. (a) mean image (2-D slice at θ_{rot} = 90°) of multi-nozzle flame forced at 190 Hz with mean flame positions overlaid and, (b) Envelope of mean flame position over a period of forcing

Bunce et al. [15] correlated the fluctuation of the mean flame base position to the amplitude of the flame response, showing that the maximum flame base fluctuation i.e. thickest mean flame base position envelope occurred at or near the flame transfer function minimum frequency and vice versa. The authors attributed this behavior to the interaction of the flame with the Kelvin–Helmholtz instability of the shear layer in the combustor. Previous work shows that when vortices are located on the hot products side of the flame, the Kelvin–Helmholtz instability is damped. They propose that when the mean flame position fluctuation is large, the flame's position relative to the shear layer changes. As the flame moves closer to the shear layer, the vorticity of the flow is dissipated (Vorticity is dissipated much faster when the vortices are located on the hot products side of the flame as opposed to the cold reactants side) and the flame response is low. Conversely, when the mean flame position fluctuation is minimal, the vorticity of the flow is not dissipated before interacting with the flame, which leads to the large flame response.

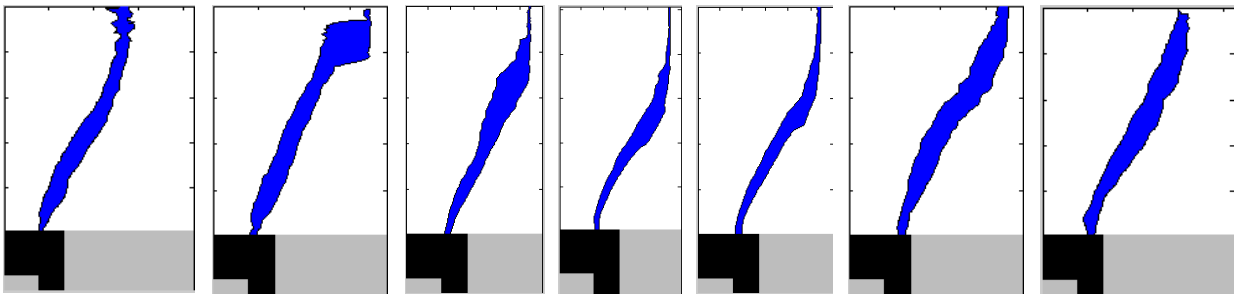

0° **30°** **60°** **90°** **120°** **150°** **180°**

Figure 3.24. Mean flame position envelopes of the image slices in the outer half of a single outer multi-nozzle flame forced at 190 Hz (minimum FTF gain)

Applying the same analysis to this data yields a result somewhat consistent with Bunce et al.'s findings. Figure 3.25 shows the mean flame position envelopes of the flame base (the 30mm downstream of the dump plane) of the flame slices in the region of interest. Five frequencies are studied: A high gain condition (100Hz), three near-minimum gain conditions which include the gain minima frequencies at all the rotation angles considered (190, 200, 220 Hz) and a maximum gain condition (280 Hz). The flame base envelope at the minimum gain frequency of each rotation angle (see plot in Figure 3.21) is highlighted with a red box.

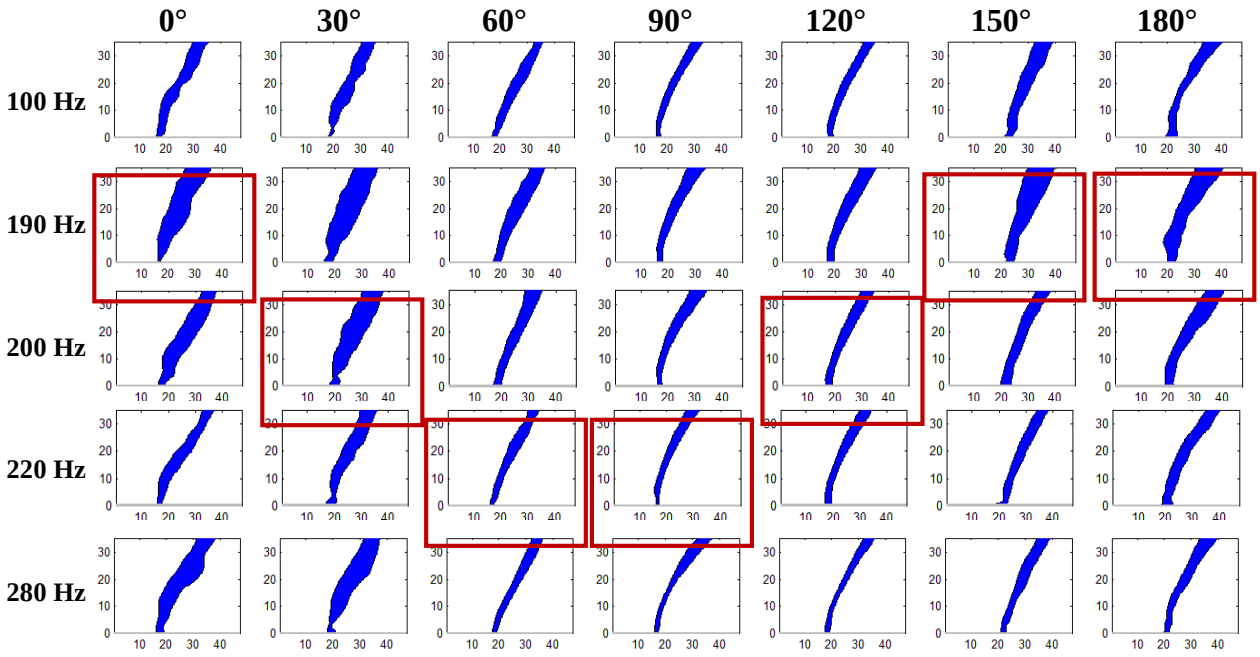

Figure 3.25. Flame base envelopes of multi-nozzle flame slices at five forcing frequencies and seven rotation angles

The largest flame base fluctuations are generally observed at the minimum gain condition. For certain cases, the largest flame base fluctuation seems to occur at the frequency adjacent to the gain minimum condition identified. This is postulated to be due to the actual gain minimum frequency being at a frequency in-between the two measurements obtained. In addition it is observed that the flame base fluctuations are smallest in the most confined cases (θ_{rot} = 60° - 120°). While Bunce observed that the minimum flame base fluctuation occurred at the maximum FTF gain condition, this is not always observed in the less confined flame slices (θ_{rot} = 0° - 30° and 180°) indicating that the effect of this mechanism on flame response differs with confinement.

4.0 Summary of results

The possibility of analyzing various regions of a 3-D image of a multi-nozzle flame was illustrated. Three independent 3-D regions were divided: the flame base, the interaction region and the outer half of a single outer flame. Due to the lack of understanding of the complex flame-flame interaction, only the outer half of a single outer flame is isolated in this portion of the study. Analyzing individual slices of this 3-D region provides data on the effect of both swirl and confinement on flame response.

Analysis of 3-D images of an unforced multi-nozzle flame yielded a range of metrics that are used to describe the flame structure from the flame images. Around the circumference of the flame for the range calculated (θ_{rot} = 0° - 180°), the flame length increases in the direction of swirl and does not seem to depend on confinement indicating that swirling flow field in the combustor affects the flame structure in addition to confinement. Using known information of the location of flow structures with respect to the flame position, approximate locations of shear layers and outer recirculation zone can be determined. The area of the outer recirculation zone shows an inverse dependence to confinement i.e. smallest ORZ size is observed at highest confinement case.

The global flame transfer function data of the multi-nozzle flame displays qualitatively similarity behavior of alternating minima and maxima as seen in previous single- and multi-nozzle studies. Good agreement is seen between the global heat release rate obtained from the PMT and the 3-D images. Flame transfer functions of the isolated 3-D regions show out of phase behavior between regions at gain minimum conditions. This indicates that destructive interference between fluctuations in these regions leads to reduced FTF gain. Isolating 2-D image slices of the outer half of a single outer flame shows that the frequency of minimum gain of each image slice is dependent on confinement i.e. the highest gain minimum frequency occurred at the highest confienement ratio case. Furthermore, the FTF data cannot be generalized with Strouhal number which shows that more than one convective mechanism is responsible for the response of the mult-nozzle flame.

The spatially-resolved heat release rate fluctuations in the forced flame images can be identified by obtaining RMS magnitude and phase images at each forcing frequency. The RMS magnitude images show that the regions of highest heat release rate fluctuation do not correspond to the center of heat release which indicates that analyses based on a single point metric that describes flame structure (such as flame length) may be inaccurate as they do not capture the regions of highest heat release rate fluctuation. The phase images show a variation in phase within the flame brush indicating that instead of the flame responding in bulk, a shorter wavelength convective disturbance propagating along the flame sheet produces local oscillations in heat release rate.

The variation of mean flame position of the flame slices of the outer half of a single outer flame in the forced flame case was investigated. The results showed that the maximum fluctuation of the flame base occurs at the gain minimum frequency which is consistent with previous research. In addition, there is a noticeable decrease in the magnitude of the fluctuation of the mean flame position as the confinement increases.

5.0 References

[1] A. Lefebvre and D. Ballal, Gas Turbine Combustion: Alternative Fuels and Emissions, Boca Raton, FL: CRC Press, 2010.

[2] M. Szedlmayer, "An Experimental Study of the Velocity Forced Flame Response of a Lean-Premixed Multi-Nozzle Can Combustor for Gas Turbines (Doctoral Dissertation)," Penn State University, University Park, PA, 2013.

[3] J. G. Lee and D. A. Santavicca, "Experimental Diagnostics for the Study of Combustion Instabilities in Premixed Combustors," *Journal of Propulsion and Power,* no. 19, pp. 735-750, 2003.

[4] American Society of Mechanical Engineers, "The World's First Industrial Gas Turbine Set at Neuchâtel (1939)," 1988.

[5] National Energy Technology Laboratory, The Gas Turbine Handbook, 2006.

[6] GE Energy, *GE 9FB Heavy Duty Gas Turbine Engine*, www.ge-energy.com, 2013.

[7] T. Lieuwen and K. McManus, "Introduction: Combustion Dynamics in Lean-Premixed Prevaporized (LPP) Gas Turbines," *Journal of Propulsion and Power,* vol. 19, no. 5, p. 721, 2003.

[8] J. J. Keller, "Thermoacoustic Oscillations in Combustion Chambers of Gas Turbines," *AIAA Journal*, vol. 33, no. 12, pp. 2280-2287, 1995.

[9] S. Turns, An Introduction to Combustion: Concepts and Applications, Third Edition, New York: McGraw-Hill, 2012.

[10] E. Kilik, A. Lefebvre and K. Ramsden, "The influence of swirler design parameters on the aerodynamics of downstream recirculation region," PhD Thesis, Cranfield Institute of Technology, Cranfield, Bedfordshire, UK, 1976.

[11] J. M. Beer and N. A. Chigier, Combustion Aerodynamics, London: Applied Science Publishers, 1972.

[12] N. Chigier and A. Chervinsky, "Experimental Investigation of Swirling Vortex Motion in Jets," *Journal of Applied Mechanics,* vol. 34, no. 2, pp. 443-451, 1967.

[13] I. Chterev, D. Foti, J. Seitzman, S. Menon and T. Lieuwen, "Flow Field Characterization in a Premixed, Swirling Annular Flow," in *50th AIAA Aerospace Sciences Meeting*, Nashville, TN, 2012.

[14] N. Syred and J. Beer, "Combustion in Swirling Flows: A Review," *Combustion and Flame,* vol. 23, pp. 143-201, 1974.

[15] O. Lucca-Negro and T. O'Doherty, "Vortex Breakdown: A Review," *Progress in Energy and Combustion Science,* vol. 27, pp. 431-481, 2001.

[16] Y. Huang and V. Yang, "Dynamics and Stability of Lean-Premixed Swirl Stabilized Combustion," *Progress in Energy and Combustion Science,* vol. 35, pp. 293-364, 2009.

[17] S. Leibovich, "the Structure of Vortex Breakdown," *Annual Review of Fluid Mechanics,* vol. 10, pp. 221-246, 1978.

[18] T. Sarpkaya, "On stationary and travelling vortex breakdowns," *J . Fluid Mech,* vol. 45, no. 3, pp. 545-559, 1975.

[19] J. O'Connor and T. Lieuwen, "Recirculation zone dynamics of a transversely excited swirl flow and flame," *Physics of Fluids,* vol. 24, no. 7, p. 075107, 2012.

[20] S. Wang, S. Hsieh and V. Yang, "Unsteady flow evolution in swirl injector with radial entry 1. Stationary conditions," *Physics of Fluids,* vol. 17, p. 045106, 2005.

[21] H. Sheen, W. Chen and S. Jeng, "Recirculation Zones of Unconfined and Confined Annular Swirling Jets," *AIAA Journal,* vol. 34, no. 3, pp. 572-579, 1996.

[22] N. Syred, "A review of oscillation mechanisms and the role of the precessing vortex core (PVC) in swirl combustion systems," *Progress in Energy and Combustion Science,* vol. 32, p. 93–161, 2006.

[23] P. M. Anacleto, E. C. Fernandes, M. V. Heitor and S. Shtork, "Swirl Flow Structure and Flame Characteristics in a Model Lean Premixed Combustor," *Combustion Science and Technology,* vol. 175, no. 8, pp. 1369-1388, 2003.

[24] A. De, S. Zhu and S. Acharya, "An Experimental and Computational Study of a Swirl-Stabilized Premixed Flame," *Journal of Engineering for Gas Turbines and Power,* vol. 132, p. 071503, 2010.

[25] N. Syred, W. Fick, T. O'Doherty and A. Griffiths, "The Effect of the Precessing Vortex Core on Combustion in a Swirl Burner," *Combustion Science and Technology,* vol. 125, pp. 139-157, 1997.

[26] M. Stohr, I. Boxx, C. Carter and W. Meier, "Experimental study of vortex-flame interaction in a gas turbine model," *Combustion and Flame,* vol. 159, p. 2636–2649, 2012.

[27] C. Duwig and L. Fuchs, "Large eddy simulation of vortex breakdown/flame interaction," *Physics of Fluids,* vol. 19, p. 075103, 2007.

[28] G. Bruneaux, T. Akselvoll, T. Poinsot and J. H. Ferziger, "Flame-Wall Interaction Simulation in a Turbulent Channel Flow," *Combustion and Flame,* vol. 107, pp. 27-44, 1996.

[29] T. Poinsot, D. Haworth and G. Bruneaux, "Direct simulation and modeling of flame-wall interaction for premixed turbulent combustion," *Combustion and Flame,* vol. 95, no. 1-2, pp. 118-132, 1993.

[30] A. De Lataillade, F. Dabireau, B. Cuenot and T. Poinsot, "Flame/Wall Interaction and Maximum Wall Heat Fluxes in Diffusion Burners," *Proceedings of the Combustion Institut,* vol. 29, p. 775–779, 2002.

[31] K. J. Nogenmyr, H. J. Cao, C. K. Chan and R. K. Cheng, "Effects of confinement on premixed turbulent swirling flame using large eddy simulation," *Combustion Theory and Modelling,* 2013.

[32] A. Gruber, R. Sankaran, E. R. Hawkes and J. H. Chen, "Turbulent flame–wall interaction: a direct numerical simulation study," *Journal of Fluid Mechanics,* vol. 658, pp. 5-32, 2010.

[33] Y. Fu, J. Cai, S. Jeng and H. Mongia, "Confiment Effects on the Swirlng Flow of a Counter-Rotating Swirl Cup," in *Proceedings of the ASME Turbo Expo*, Reno-Tahoe, Nevada, 2005.

[34] A. L. Birbaud, D. Durox, S. Ducruix and S. Candel, "Dynamics of confined premixed flames submitted to upstream acoustic modulations," *Proceedings of the Combustion Institute,* vol. 27, p. 1257–1265, 2007.

[35] N. Worth and J. Dawson, "Cinematographic OH-PLIF measurements of two interacting turbulent premixed flames with and without acoustic forcing," *Combustion and Flame*, vol. 159, p. 1109–1126, 2012.

[36] T. Hirasawa, K. Gotanda, H. Masuda and Y. Nakamura, "Impact of Flame–Flame Interactions in Identical Twin Diffusion Microflames," *Combustion Science and Technology,* vol. 184, p. 1651–1663, 2012.

[37] Y. Yahagi, M. Sekiguti and K. Suzuki, "Flow structure and flame stability in a micro can combustor with a baffle plate," *Applied Thermal Engineering,* vol. 27, p. 788–794, 2007.

[38] K. Tatsumi, Y. Rai and Y. Nibayashi, "Mixing and Combustion Performances of a Baffle-Plate-Type Miniature Confined Multi-Jet," *Journal of Fluid Science and Technology,* vol. 6, no. 4, pp. 465-476, 2011.

[39] I. Francois, D. Larrauri and D. Escudie, "Interaction Between Two Premixed Laminar V-Shaped Flame Fronts at Low Lewis Number," *Combustion and Flame,* vol. 110, pp. 14-24, 1997.

[40] T. Yokomori and M. Mizomoto, "Interaction of Adjacent Flame Surfaces on the Formation of Wrinkling Laminar Premixed Flame," *Proceedings of the Combustion Institute,* vol. 29, pp. 1511-1517, 2002.

[41] D. Fanaca, P. R. Alemela, C. Hirsch and T. Sattelmayer, "Comparison of the Flow Field of a Swirl Stabilized Premixed Burner in an Annular and a Single Burner Combustion Chamber," *Journal of Engineering for Gas Turbines and Power,* vol. 132, p. 071502, 2010.

[42] K. Kunze, C. Hirsch and T. Sattelmayer, "Transfer Function Measurements on a Swirl Stabilized Premix Burner in an Annular Combustion Chamber," in *Proceedings of ASME Turbo Expo: Power for Land, Sea and Air*, Vienna, Austria, 2004.

[43] T. D. Dunstan, N. Swaminathan, K. N. C. Bray and N. G. Kingsbury, "Flame Interactions in Turbulent Premixed Twin V-Flames," *Combustion Science and Technology,* vol. 185, pp. 134-159, 2013.

[44] N. A. Worth and J. R. Dawson, "Self-excited circumferential instabilities in a model annular gas turbine combustor: Global flame dynamics," *Proceedings of the Combustion Institute*, vol. 34, p. 3127–3134, 2013.

[45] D. Kim, J. G. Lee, B. D. Quay, D. A. Santavicca, K. Kim and S. Srinivasan, "Effect of Flame Structure on the Flame Transfer Function in a Premixed Gas Turbine Combustor," *Journal of Engineering for Gas Turbines and Power,* vol. 132, p. 021502, 2010.

[46] S. Terhaar, B. Ćosić, C. O. Paschereit and K. Oberleithner, "Impact of Shear Flow Instabilities on the Magnitude and Saturation of the Flame Response," in *Proceedings of the ASME Turbo Expo 2013*, San Antonio, TX, 2013.

[47] B. Zinn and T. Lieuwen, "Combustion Instabilities: Basic Concepts," in *Combustion Instabilities in Gas Turbine Engines: Operational Experience, Fundamental Mechanisms, and Modeling*, Progress in Astronautics and Aeronautics, Vol 210, 2005.

[48] S. Candel, "Combustion Dynamics and Control: Progress and Challenges," *Proceedings of the Combustion Institute,* vol. 29, pp. 1-28, 2002.

[49] S. Ducruix, T. Schuller, D. Durox and S. Candel, "Combustion Dynamics and Instabilities: Elementary Coupling and Driving Mechanisms," *Journal of Propulsion and Power,* vol. 19, no. 5, pp. 722-734, 2003.

[50] V. Yang and W. Anderson, Liquid Rocket Engine Combustion Instability, AIAA: Progress in Astronautics and Aeronautics, 1995.

[51] S. Menon and W. Jou, "Large-Eddy Simulations of Combustion Instability in an Axisymmetric Ramjet Combustor," *Combustion Science and Technology,* vol. 75, no. 1-3, pp. 53-72, 1991.

[52] D. E. Rogers and F. E. Marble, "A mechanism for high-frequency oscillation in ramjet combustors and afterburners," *Jet Propulsion,* vol. 26, no. 6, pp. 456-462, 1956.

[53] G. J. Bloxsidge, A. P. Dowling and P. J. Langhorne, "Reheat buzz : an acoustically coupled combustion instability. Part 2. Theory," *Journal of Fluid Mechanics,* vol. 1988, pp. 445-473, 1988.

[54] P. J. Langhorne, "Reheat buzz : an acoustically coupled combustion instability. Part 1. Experiment," *Journal of Fluid Mechanics,* vol. 193, pp. 417-443, 1988.

[55] T. Lieuwen and V. Yang, Combustion Instabilities in Gas Turbine Engines, AIAA: Progress in Astronautics and Aeronautics, 2005.

[56] M. W. Thring, "Combustion oscillations in industrial combustion chambers," *Symposium (International) on Combustion,* vol. 12, no. 1, pp. 163-168, 1969.

[57] P. L. Woodfield, J. H. Kent and T. F. Dixon, "Computational modelling of combustion instability in bagasse-fired furnaces," *Experimental Thermal and Fluid Science,* vol. 21, no. 1-3, pp. 17-25, 2000.

[58] J. Rayleigh, "The Explanation of Certain Acoustical Phenomena," *Nature,* pp. 319-321, 1878.

[59] S. Peluso, B. D. Quay, J. G. Lee and D. A. Santavicca, "Comparison Between Self-Excited and Forced Flame Response of an Industrial Lean Premixed Gas Turbine Injector," in *Proceedings of ASME Turbo Expo*, Vancouver, 2011.

[60] T. Lieuwen, "Experimental Investigation of Limit-Cycle Oscillations in an Unstable Gas Turbine Combustor," *Journal of Propulsion and Power,* vol. 18, no. 1, pp. 61-67, 2002.

[61] J. H. Cho and T. Lieuwen, "Laminar Premixed Flame Response to Equivalence Ration Oscillations," *Combustion and Flames,* vol. 140, pp. 116-129, 2005.

[62] H. Y. Wang, C. K. Law and T. Lieuwen, "Linear response of stretch-affected premixed flames to flow oscillations," *Combustion and Flame,* vol. 156, pp. 889-895, 2009.

[63] H. J. Merk, "An analysis of unstable combustion of premixed gases," *Symposium (International) on Combustion,* vol. 6, pp. 500-512, 1957.

[64] Y. Matsui, "An Experimental Study on Pyro-Acoustic Amplification of Premixed Laminar Flames," *Combustion and Flame,* vol. 1981, pp. 199-209, 1981.

[65] T. Schuller, S. Ducruix, D. Durox and S. Candel, "Modeling Tools for the Prediction of Premixed Flame Transfer Functions," *Proceedings of the Combustion Institute,* vol. 29, pp. 107-113, 2002.

[66] M. Fleifil, A. M. Annaswamy, Z. A. Ghoneim and A. F. Ghoneim, "Response of a Laminar Premixed Flame to Flow Oscillations: A Kinematic Model and Thermoacoustic Instability Results," *Combustion and Flame,* vol. 106, pp. 487-510, 1996.

[67] A. Bourehla and F. Baillot, "Appearance and Stability of a Laminar Conical Premixed Flame Subjected to an Acoustic Perturbation," *Combustion and Flame,* vol. 114, pp. 303-318, 1998.

[68] S. Ducruix, D. Durox and S. Candel, "Theoretical and Experimental Determinations of the Transfer Function of a Laminar Premixed Flame," *Proceedings of the Combustion Institute*, vol. 28, pp. 765-773, 2000.

[69] S. Kartheekeyan and S. Chakravarthy, "An experimental investigation of an acoustically excited laminar premixed flame," *Combustion and Flame,* vol. 146, p. 513–529, 2006.

[70] Preetham, H. Santosh and T. Lieuwen, "Dynamics of Laminar Premixed Flames Forced by Harmonic Velocity Disturbances," *Journal of Propulsion and Power,* vol. 24, no. 6, pp. 1390-1402, 2008.

[71] C. Kulsheimer and H. Buchner, "Combustion Dynamics of Turbulent Swirling Flames," *Combustion and Flame,* vol. 131, pp. 70-84, 2002.

[72] K. T. Kim, J. G. Lee, H. J. Lee, B. D. Quay and D. A. Santavicca, "Characterization of Forced Flame Response of Swirl-Stabilized Turbulent Lean-Premixed Flames in a Gas Turbine Combustor," *Journal of Engineering for Gas Turbines and Power,* vol. 132, p. 041502, 2010.

[73] K. Kim, J. G. Lee, B. D. Quay and D. A. Santavicca, "The Dynamic Response of Turbulent Dihedral V Flames: An Amplification Mechanism of Swirling Flames," *Combustion Science and Technology,* vol. 183, no. 2, pp. 163-179, 2010.

[74] P. Palies, D. Durox, T. Schuller and S. Candel, "The combined dynamics of swirler and turbulent premixed swirling flames," *Combustion and Flame,* vol. 157, p. 1698–1717, 2010.

[75] P. Palies, D. Durox, T. Schuller and S. Candel, "Experimental Study on the Effect of Swirler Geometry and Swirl Number on Flame Describing Functions," *Combustion Science and Technology,* vol. 183, no. 7, pp. 704 - 717, 2011.

[76] G. Borghesi, F. Biagioli and B. Schuermans, "Dynamic response of turbulent swirling flames to acoustic perturbations," *Combustion Theory and Modelling,* vol. 131, no. 3, pp. 487-512, 2009.

[77] R. Balachandran, B. Ayoola, C. Kaminski, A. Dowling and E. Mastorakos, "Experimental investigation of the nonlinear response of turbulent premixed flames to imposed inlet velocity oscillations," *Combustion and Flame,* vol. 143, p. 37–55, 2005.

[78] D. Fanaca, P. R. Alemela, F. Ettner, C. Hirsch and T. Sattelmayer, "Determination and comparison of the dynamic characteristics of a perfectly premixed flame in both single and annular combustion chambers," in *Proceedings of ASME Turbo Expo 2008: Power for Land, Sea and Air*, Berlin, 2008.

[79] J. O'Connor, N. A. Worth and J. R. Dawson, "Flame and Flow Dynamics of a Self-Exctied, Standing Wave Circumferential Instability in a Model Annular Gas Turbine Combustor," in *Proceedings of the ASME Turbo Expo 2013, Power for Land, Sea, and Air*, San Antonio, 2013.

[80] B. Jones, J. G. Lee, B. D. Quay and D. A. Santavicca, "Flame Response Mechanisms Due to Velocity Perturbations in a Lean Premixed Gas Turbine Combustor," *Journal of Engineering for Gas Turbines and Power,* vol. 133, p. 021503, 2011.

[81] P. Palies, T. Schuller, D. Durox and S. Candel, "Modeling of premixed swirling flames transfer functions," *Proceedings of the Combustion Institute,* vol. 33, p. 2967–2974, 2011.

[82] P. Palies, T. Schuller, D. Durox, L. Y. M. Gicquel and S. Candel, "Acoustically perturbed turbulent premixed swirling flames," *Physics of Fluids,* vol. 23, p. 037101, 2011.

[83] G. Markstein, "Theory of Flame Propagation," in *Non-steady Flame Propagation*, New York, Macmillan, 1964.

[84] N. A. Bunce, B. D. Quay and D. A. Santavicca, "Interaction Between Swirl Number Fluctuations and Vortex Shedding in a Single-Nozzle Turbulent Swirling Fully-Premixed Combustor," *Journal of Engineering for Gas Turbines and Power,* vol. 136, p. 021503, 2013.

[85] A. Steinberg, I. Boxx, M. Stöhr, C. Carter and W. Meier, "Flow–flame interactions causing acoustically coupled heat release fluctuations in a thermo-acoustically unstable gas turbine model combustor," *Combustion and Flame,* vol. 157, p. 2250–2266, 2010.

[86] A. Steinberg, I. Boxx, M. Stöhr and W. Meier, "Effects of Flow Structure Dynamics on Thermoacoustic Instabilities in Swirl-Stabilized Combustion," *AIAA Journal,* vol. 50, no. 4, pp. 952-967, 2012.

[87] R. Santhosh, A. Miglani and S. Basu, "Transition and acoustic response of recirculation structures in an unconfined co-axial isothermal swirling flow," *Physics of Fluids,* vol. 25, p. 083603, 2013.

[88] K. S. Kedia, H. M. Altay and A. F. Ghoniem, "Impact of flame-wall interaction on premixed flame dynamics and transfer function characteristics," *Proceedings of the Combustion Institute,* vol. 33, p. 1113–1120, 2011.

[89] T. Poinsot, A. C. Trouve, D. P. Veynante, S. M. Candel and E. J. Esposito, "Vortex-driven acoustically coupled combustion instabilities," *Journal of Fluid Mechanics,* vol. 177, pp. 265-292, 1987.

[90] N. Noiray, D. Durox, T. Schuller and S. Candel, "Self-induced instabilities of premixed flames in a multiple injection configuration," *Combustion and Flame,* vol. 145, p. 435–446, 2006.

[91] M. T. Szedlmayer, B. D. Quay, J. Samarasinghe, A. De Rosa, J. G. Lee and D. A. Santavicca, "Forced Flame Response of a Lean Premixed Multi-Nozzle Can Combustor," in *Proceedings of ASME Turbo Expo*, Vancouver, 2011.

[92] J. G. Lee, E. Gonzalez and D. A. Santavicca, "On the Applicability of Chemiluminescence to the Estimation of Unsteady Heat-Release During Unstable Combustion in a Lean Premixed Combustor," in *41st AIAA/ASME/SAE/ASEE Joint Propulsion Conference & Exhibit*, Tucson, AZ, 2005.

[93] M. P. Waser and M. J. Crocker, "Introduction to the Two-Microphone Cross-Spectral Method of Determining Sound Intensity," *Noise Control Engineering Journal,* vol. 22, no. 3, pp. 76-85, 1984.

[94] M. Abom and H. Boden, "Error analysis of two-microphone measurements in ducts with flow," *Journal of the Acoustical Society of America,* vol. 83, no. 6, pp. 2429-2438, 1988.

[95] C. Marton, Advances in electronics and electron physics, Academic Press, 1981.

[96] J. Radon, "On the determination of functions from their integral values along certain manifolds," *Medical Imaging, IEEE Transactions,* vol. 5, no. 4, pp. 170-176, 1986.

[97] J. Radon, "Über die Bestimmung von Funktionen durch ihre Integralwerte längs gewisser Mannigfaltigkeiten," *Berichte über die Verhandlungen der Sächsische Akademie der*

Wissenschaften (Reports on the proceedings of the Saxony Academy of Science), no. 69, p. 262–277, 1917.

[98] G. Herman, "Image Reconstruction From Projections," *Real-Time Imaging,* vol. 1, no. 1, pp. 3-18, 1995.

[99] A. Bui and R. Taira, Medical Imaging Informatics, Springer, 2009.

[100] P. Midgley and M. Weyland, "3D electron microscopy in the physical sciences: the development of Z-contrast and EFTEM tomography," *Ultramicroscopy,* vol. 96, no. 3–4, pp. 413-431, 2003.

[101] S. Pennycook, Scanning Transmission Electron Microscopy: Imaging and Analysis, Springer, 2011.

[102] M. de Hoop, H. Smith, G. Uhlmann and R. van der Hilst, "Seismic imaging with the generalized Radon transform:," *Inverse Problems,* vol. 25, no. 2, 2009.

[103] G. Nolet, Seismic tomography: with applications in global seismology and exploration geophysics, Dordrecht, Holland: D. Reidel Publishing Company, 1987.

[104] G. Gilabert, G. Lu and Y. Yan, "Three dimensional visualisation and reconstruction of the luminosity distribution of a flame using digital imaging techniques," *Journal of physics: Conference Series (1742-6588),* no. 15, p. 167, 2005.

[105] G. Gilabert, G. Lu and Y. Yan, "Three-Dimensional Tomographic Reconstruction of the Luminosity Distribution of a Combustion Flame," *IEEE Transactions on Instrumentation and Measurement,* vol. 56, no. 4, pp. 1300-1306, 2007.

[106] M. M. Hossain, G. Lu and Y. Yan, "Three-dimensional Reconstruction of Combustion Flames through Optical Fiber Sensing and CCD Imaging," *Instrumentation and Measurement Technology Conference (I2MTC), 2011 IEEE,* pp. 1-5, 2011.

[107] P. M. Brisley, G. Lu, Y. Yan and S. Cornwell, "Three-Dimensional Temperature Measurement of Combustion Flames Using a Single Monochromatic CCD Camera," *IEEE Transactions on Instrumentation and Measurement,* pp. 1417-1420, 2005.

[108] N. Anikin, R. Suntz and H. Bockhorn, "Tomographic reconstruction of the OH∗-chemiluminescence distribution in premixed and diffusion flames," *Applied Physic B,* vol. 100, no. 3, pp. 675-694, 2010.

[109] N. Anikin, R. Suntz and H. Bockhorn, "Tomographic reconstruction of 2D-OH∗-chemiluminescence distributions in turbulent diffusion flames," *Applied Physics B,* vol. 107, no. 3, pp. 591-602, 2012.

[110] J. Moeck, J. Bourgouin, D. Durox, T. Schuller and S. Candel, "Nonlinear interaction between a precessing vortex core and acoustic oscillations in a turbulent swirling flame," *Combustion and Flame,* vol. 159, no. 8, p. 2650–2668, 2012.

[111] T. Upton, D. Verhoeven and D. Hudgins, "High-resolution computed tomography of a turbulent reacting flow," *Experiments in Fluids,* vol. 50, no. 1, pp. 125-134, 2011.

[112] J. Floyd and A. Kempf, "Computed Tomography of Chemiluminescence (CTC): High resolution and instantaneous 3-D measurements of a Matrix burner," *Proceedings of the Combustion Institute,* vol. 33, no. 1, pp. 751-758, 2011.

[113] J. Floyd, P. Geipel and A. Kempf, "Computed Tomography of Chemiluminescence (CTC): Instantaneous 3D measurements and Phantom studies of a turbulent opposed jet flame," *Combustion and Flame,* vol. 158, no. 2, pp. 376-391, 2011.

[114] N. A. Worth and J. R. Dawson, "Tomographic reconstruction of OH* chemiluminescence in two interacting turbulent flames," *Measurement Science and Technology,* vol. 24, p. 024013, 2013.

[115] Y. Ishino, K. Takeuchi, S. Shiga and N. Ohiwa, "Measurement of Instantaneous 3D-Distribution of Local Burning Velocity on a Turbulent Premixed Flame by Non-Scanning 3D-CT Reconstruction," in *European Combustion Meeting*, 2009.

[116] Y. Ishino and N. Ohiwa, "Three-Dimensional Computerized Tomographic Reconstruction of Instantaneous Distribution of Chemiluminescence of a Turbulent Premixed Flame," *JSME International Journal Series B Fluids and Thermal Engineering,* vol. 48, no. 1, pp. 34-40, 2005.

[117] H. Bheemul, G. Lu and Y. Yan, "Digital Imaging-Based Three-Dimensional Characterization of Flame Front Structures in a Turbulent Flame," *IEEE Transactions on Instrumentation and Measurement,* vol. 54, no. 3, 2005.

[118] H. Bheemul, G. Lu and Y. Yan, "Three-dimensional visualization and quantitative characterization of gaseous flames," *Measurement Science and Technology,* vol. 13, no. 10, pp. 1643-1650, 2002.

[119] S. Deans, "Radon and Abel Transforms," in *The Transforms and Applications Handbook: Second Edition*, Boca Raton, FL, CRC Press LLC, 2000.

[120] L. Ji and K. Gallo, "An agreement coefficient for image comparison," *Photogrammetric engineering and remote sensing,* vol. 72, no. 7, p. 823, 2006.

[121] A. Dhawan, "Image Reconstruction," in *Medical Image Analysis,* Wiley-IEEE Press, 2011, pp. 173-180.

[122] W. S. Cheung, G. J. M. Sims, R. W. Copplestone, J. R. Tilston, C. W. Wilson, S. R. Stow and A. P. Dowling, "Measurement and Analysis of Flame Transfer Function in a Sector Combustor Under High Pressure Conditions," in *Proceedings of the ASME Turbo Expo*, Atlanta, GA, 2003.

[123] E. Freitag, H. Konle, M. Lauer, C. Hirsch and T. Sattelmayer, "Pressure Influence on the Flame Transfer Function of a Premixed Swirling Flame," in *Proceedings of the ASME Turbo Expo 2006: Power for Land, Sea and Air*, Barcelona, Spain, 2006.

[124] K. T. Kim and D. A. Santavicca, "Generalization of Turbulent Swirl Flame Transfer Functions in Gas Turbine Combustors," *Combustion Science and Technology,* vol. 185, no. 7, pp. 999-1015, 2013.

[125] C. S. Cooper and N. M. Laurendeau, "Quantitative Measurements of Nitric Oxide in High-Pressure (2–5 atm), Swirl-Stabilized Spray Flames via Laser-Induced Fluorescence," *Combustion and Flame,* vol. 123, pp. 175-188, 2000.

[126] J. K. Eaton and J. P. Johnston, "A Review of Research on Subsonic Turbulent Flow Reattachment," *AIAA Journal,* vol. 19, no. 9, pp. 1093-1100, 1981.

[127] S. Peluso, "An Experimental Study of Flame Response Mechanisms in a Lean-Premixed Gas Turbine Combustor (Doctoral Dissertation)," Penn State University, University Park, PA, 2012.

[128] N. A. Bunce, B. D. Quay and D. A. Santavicca, "Interaction Between Swirl Number Fluctuations and Vortex Shedding in a Single-Nozzle Turbulent Swirling Fully-Premixed

Combustor," *Journal of Engineering for Gas Turbines and Power,* vol. 136, p. 021503, 2013.

[129] R. Chen and J. Driscoll, "The role of the recirculation vortex in improving fuel-air mixing within swirling flames," in *Twenty-Second Symposium (International) on Combustion, The Combustion Institute* , 1988.

[130] C. Goy, S. James and S. Rea, "Monitoring Combustion Instabilities: E.ON UK's Experience," in *Combustion Instabilities in Gas Turbine Engines: Operational Experience, Fundamental Mechanisms, and Modeling*, Progress in Astronautics and Aeronautics, Vol 210, 2005.

Technical Details – Georgia Institute of Technology

1.0 Introduction

The key accomplishment of this research program was to broaden our understanding of combustion instabilities through both analytical and experimental work – in particular to take prior knowledge that has been gained for single nozzle systems, and to see how this generalizes and what new physics arise with multi-nozzle systems. “Combustion instabilities” refers to damaging pressure oscillations excited by the combustion process. If significant, the amplitude of these oscillations causes significant damage in low emissions turbines every year, through forced outages and broken parts. Predictive models were developed for flame response of multi-nozzle premixed flames to helical flow disturbances and for analyzing azimuthal flow fluctuations in the annular nozzle of a swirler. Sub-analyses were also performed to resolve and elucidate additional questions which surfaced through our efforts. Two of such being reconciling differences in the analytical, laminar, linear flame transfer function derived with bulk forcing in three different coordinate systems for a two-dimensional, bluff body-anchored flame and developing theoretical models to explain the behavior of the flow fields obtained from the experimental data previously obtained.

2.0 Work Overview

This report summarizes our efforts on the response of time-averaged non-axisymmetric premixed flames (such as would be encountered in a multi-nozzle combustion system) to axisymmetric and helical flow disturbances. These disturbances have an azimuthal disturbance of the form $\hat{u}_i' \propto \exp(im\theta)$ where m denotes the helical mode number. For axisymmetric mean flames, such as would be encountered in single-nozzle test environments, it is known that the helical modes affect local flame response to varying degrees but that the global flame response was purely due to the m=0 mode. This is due to area cancellations effects between diametrically opposite locations on a perfectly axisymmetric flame surface. However, in the case of mean flame non-axisymmetry, the azimuthal deviations on the mean flame surface inhibit such cancellations and the asymmetric helical modes ($m \neq 0$) cause a finite global flame response. In this report, the theoretical framework for both weakly non-axisymmetric flames and a numerical solver for strongly non-axisymmetric flames is presented and used with two example cases. These examples clearly illustrate the contributions made by these asymmetric helical modes to the global flame response (Flame Transfer Function) and how this varies with different control parameters such as degree of asymmetry in mean flame, Strouhal number, Mach number and flame angle.

Additional work done under this program includes the analytical and experimental investigation of the dynamics of harmonically forced turbulent flames. The turbulent local consumption speed was studied to determine how it was influenced by harmonic flame wrinkling. Along a similar analytical path, flame transfer functions were investigated utilizing the G-equation, and the derived ξ-equation. Significantly, this work reconciled differences in the analytical, laminar, linear flame transfer function derived with bulk forcing in three different coordinate systems for a two-dimensional, bluff body-anchored flame. Our work completely reconciled differences in the

analytical, laminar, linear flame transfer function derived with bulk forcing in three different coordinate systems for a two-dimensional, bluff body-anchored flame. Interesting and significant findings were obtained which close this problem. In addition, work was done to elucidate previously obtained experimental data results. Progress has been made on the development of theoretical models to explain the behavior of the flow fields obtained from the experimental data previously obtained. From the experimental data it was observed that the behavior of the stagnation point varied drastically between the instantaneous and the time-averaged flow field. A theoretical model has been proposed which quantitatively explains this behavior.

In the experimental regime, work was done on the helical mode decomposition of a transversely forced, swirl stabilized combustor. Experimental data was post processed and analyzed. A major part of this analysis was on the helical mode decomposition (HMD) performed on the time resolved velocity fields. One of the dominant mechanisms leading to heat release oscillations in swirl combustors are flow velocity fluctuations. The flow oscillations are comprised of both acoustic and vortical disturbances. The direct excitation of the flame by these flow disturbances has previously been treated in detail by both experimental and modeling studies. Acoustic waves are directly excited by the flame and reverberate in the combustor system. Vortical disturbances are generated by modulation of the separating shear layer, which organize themselves into concentrated regions of vorticity through the Kelvin-Helmholtz instability. In addition, there exists an additional, “indirect” mechanism that is unique to swirl flows. In this mechanism, acoustic waves propagating through swirlers excite axial vortical disturbances, leading to modulations in swirl number.

3.0 Response of non-axisymmetric premixed flames to helical flow disturbances

The response of axisymmetric premixed swirling flames to helical flow disturbances has already been studied by our previous efforts. In contrast, coming from work done during this reporting period, we shall summarize results for the case when the time-averaged mean flame is non-axisymmetric. This problem was motivated by interest in combustion instability where the acoustics, flow hydrodynamics and unsteady heat release are tightly coupled.

Swirling flows are subject to hydrodynamic flow instabilities, leading to a variety of unsteady flow features, such as the precessing vortex core and helical shear layer disturbances[1-5]. In addition, vortex breakdown is a manifestation of the global instability of flows with sufficient swirl[2, 6-10]. In turn, these steady and unsteady swirl flow characteristics control flow recirculation[11, 12], flame stabilization, flame shape, dynamic stability limits[13], as well as a number of other critical parameters in swirl combustors.
The excitation of flames by harmonic flow disturbances is of particular focus. The direct excitation of the flame by both acoustic and vortical flow disturbances has previously been treated in detail[14-16]. These interactions have been successfully analyzed using level set approaches to predict the space-time distribution of unsteady flame wrinkling and heat release oscillations[17-19]. In addition there exists an additional, "indirect" mechanism that is unique to swirl flows where acoustic waves propagating through swirlers excite axial vortical disturbances, leading to modulations in swirl number[20-24].

Existing flame response studies have primarily focused on the flame response to axisymmetric disturbances, such as ring vortices excited by the flow forcing. However, there are two important instances where the forcing is non-axisymmetric, a feature, which excites an additional degree of freedom into the problem, as, described later. First, during transverse instabilities, the flame may be subjected to transverse acoustic oscillations, which induce an intrinsically non-axisymmetric forcing on the flame[25]. This problem has been analyzed earlier by the authors[26]. In addition, helical modes may be excited during both axial and transverse acoustic instabilities. For example, Figure 1 shows a simulation by Huang and Yang[27], clearly indicating the helical flow disturbances in the combustor.

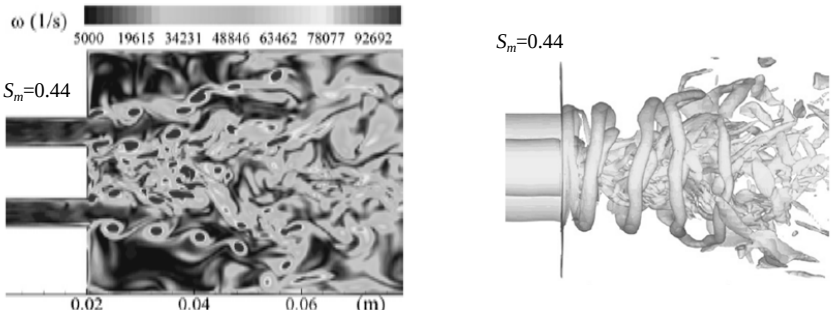

(a) **(b)**

Figure 1 – Snapshots from LES-level-set computations of (a) vorticity field magnitude and (b) iso-vorticity surfaces for a swirl number of 0.44, reproduced from Huang and Yang[27].

In order to fix some notation, consider the following azimuthal decomposition of the fluctuating flow field into helical modes as:

where

$$\hat{u}_i'(r,\theta,z,\omega) = \sum_{m=-\infty}^{\infty} \hat{B}_{i,m}(r,z,\omega)\, e^{im\theta}$$

$$\hat{B}_{i,m}(r,z,\omega) = \frac{1}{2\pi}\int_0^{2\pi} e^{-im\theta}\hat{u}_i'(r,\theta,z,\omega)\, d\theta \qquad (1)$$

where $\hat{u}_i'$ is the Fourier transform of the fluctuating velocity field in the i-direction and $\hat{B}_{i,m}$ is the amplitude of its helical mode number *m*. Note that, $m = 0$ is the axisymmetric mode, while $m < 0$ and $m>0$ denote the co-swirling (counter-clockwise) and counter-swirling (clockwise) modes, respectively[1].

Helical modes are present in both swirling and non-swirling jets and wake flows. In non-swirling jets, the relative strengths of the axisymmetric, $m = 0$ mode and low order helical modes is a function of the separating boundary layer thickness very near the jet exit, while helical modes

[1] The phase function of the disturbance at a fixed time is defined as $(kz + m\theta)$, where z is the axial flow direction and θ increases in the swirl direction. Hence, a positive mode (+*m*) has a line of constant phase with a sense of winding in the opposite direction to swirl. Conversely, a negative mode (-*m*) is co-rotating with the swirl.

dominate downstream of the potential core[28-30]. Similarly, the dominant instability mode in non-swirling, axisymmetric wakes is the helical, $m = \pm 1$ modes [31, 32].

The presence of swirl further influences the hydrodynamic stability tendencies of the flow, and biases the strength of the positive and negative mode numbers. Depending upon the flow configuration and specific instability leading to the helical disturbances, they may either wind co- or counter-to the direction of swirl. For example, stability calculations were performed by Loiseleux *et al.*[33] for a Rankine vortex model with the following velocity profiles:

$$\begin{aligned} r < R: &\qquad \bar{U}_z(r) = U_\infty + \Delta U, \quad \bar{U}_r(r) = 0, \quad \bar{U}_\theta(r) = \Omega r \\ r > R: &\qquad \bar{U}_z(r) = U_\infty, \quad \bar{U}_r(r) = 0, \quad \bar{U}_\theta(r) = \Omega R^2 / r \end{aligned} \tag{2}$$

They show that increasing swirl number decreases the temporal instability growth rate of the axisymmetric, *m*=0 mode. Impacts of swirl on helical modes are more complex, generally showing non-monotonic behavior. For example, the $m = -1$ is influenced differently by swirl in two ranges $0 \le S \le S_c$ and $S \ge S_c$, where $S = \Omega R / \Delta U$ is the swirl number and $S_c(m = -1) = 0.46$. In the range $S \ge S_c$, increasing S decreases the temporal growth rate of all axial wave numbers, which, nonetheless, remain unstable for all *S*. For $S \le S_c$, increasing *S* has a stabilizing and destabilizing impact on low and high wave number disturbances, respectively.

Having considered some basic issues associated with hydrodynamic stability that explain why helical disturbances are present in swirl flows, we next consider the flame response problem. The Rayleigh criterion[34] describes the conditions under which a periodic heat release adds energy into acoustic oscillations. Mathematically, this is given by:

$$\iint_V \int_t p'(\vec{x},t) q'(\vec{x},t) dt dV \ge 0 \tag{3}$$

For a given point in the combustor, the heat release process adds energy locally to the acoustic field when the magnitude of the phase between the pressure and heat release oscillations is less than 90 degrees. In situations where the flame region is small relative to an acoustic wavelength, the spatially integrated heat release, $Q'(t)$, is of particular interest for combustion noise and thermoacoustic instability problems. This is given by:

$$Q'(t) = \iint_V q'(\vec{x},t) dV \tag{4}$$

For this "acoustically compact" case, it is this single quantity, $Q'(t)$, which controls the noise generation by flames and/or the thermoacoustic stability of a ducted system, regardless of the spatial details, $q'(\vec{x},t)$. For this reason, we will focus significant attention on $Q'(t)$ in this paper.

A number of observations of forced flames or flames during instabilities have noted the strong presence of helical disturbances along the flame[9, 10, 35-39]. In non-swirling flows, it is well known that important interference effects control the axial flame wrinkling character, as vortices disturbing the flame, and the flame wrinkles excited by these convecting vortices, do not generally

travel at the same speed. In swirling flows, the simultaneous presence of swirl and helical disturbances introduces important physics because of the simultaneous azimuthal and axial propagation of wrinkles by the flow[40-42]. As such, interference processes influence both the axial and azimuthal distribution of flame wrinkling and the distribution of the unsteady heat release. These flame wrinkle propagation processes cause the flame to respond differently to helical modes winding co- and counter- to the swirl direction. Recent experimental work by Moeck*et al.*[38] studied the interaction of a helical flow mode with the heat release of a swirl-stabilized, premixed flame. Their results indicated that the helical mode excites azimuthally rotating heat release oscillations on the flame. They also inferred that phase averaged images of the vertical cuts of the flame were different view angles of a stationary structure. In addition, they presented a second order analysis of the *G*-equation to illustrate the sources of non-linear interactions between flame wrinkles excited by acoustic and vortical disturbances; e.g., the excitation of sum and difference frequencies in flame response. Additionally, experiments performed by Stohr*et al.*[37] characterized the phase-averaged, three-dimensional structure of the reaction zone, drawing similar conclusions as Moeck*et al.*[38]. Finally, recent experiments by Worth and Dawson[43] analyzed the global heat release dynamics due to self-excited circumferential instabilities in an annular combustor. Depending upon azimuthal location of the nozzle in the standing wave, they showed that significantly different helical disturbances were excited in the flame, consistent with observations of O'Connor and Lieuwen[39]. They also showed that flames excited by helical disturbances, as opposed to axisymmetric structures, had much smaller amplitude of heat release oscillations, also consistent with the above observations.

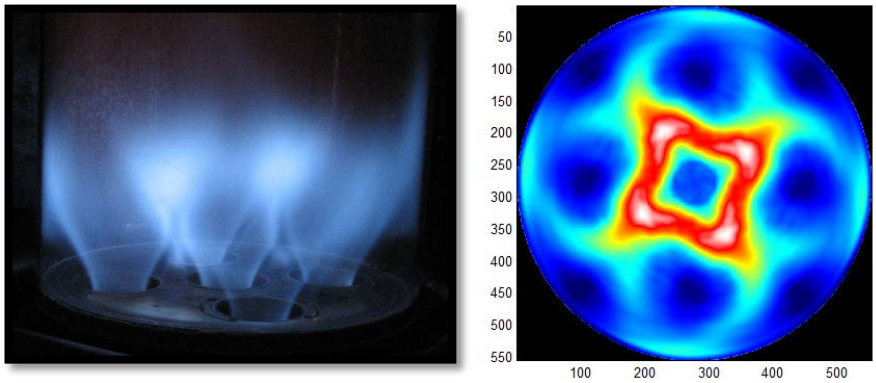

Figure 2 - Side and end-on view of a combustor with five swirling nozzles, showing the non-circular shape taken by the flames. Images reproduced from Ref. [44].

The key contribution of this portion of the final report is to present a systematic analysis of premixed flames to helical modes. In particular, it focuses on the spatially integrated heat release, or Flame Transfer Function (*FTF*). It first describes the analytical formulation used to analyze this problem. Earlier work on axisymmetric flames showed that the *FTF* was zero for asymmetric helical modes ($m \neq 0$) and that only the m=0 mode contributed to the *FTF*. An important observation from this result relates to comparisons of the forced response sensitivities of axisymmetric and non-axisymmetric flames. For example, single flames are nearly axisymmetric when placed in circular geometries. However, a single flame becomes non-axisymmetric when placed in a non-circular geometry, such as a square or sector combustor. In addition, multiple nozzles configurations generally lead to strong flame-flame interactions, whose shapes are

decidedly not axisymmetric [45]. An illustrative example of this point is shown in Figure 2, showing a side view and end-on visualization of a 5-flame configuration housed in a circular combustor [44]. Note the nearly square shape of the central flame. *Thus, the sensitivity of the flame to helical modes is fundamentally different in axisymmetric or non-axisymmetric environments.* In this section of the report we consider the effects of mean flame non-axisymmetry and hence how asymmetric modes in the disturbance field affect global flame response (*FTF*). The general analyses presented is followed by explicit calculations and solutions for a solid body swirling flow showing the contributions made by the asymmetric helical modes in the *FTF*.

We first reiterate the formulation from the previous report. The analytical formulation is based on the front tracking approach[46-50] that is used to capture thin flame surfaces. The flame is assumed to be located at the zero contour of an implicit function denoted as, $G(r,\theta,z,t)$. The evolution of this contour is tracked using the G-equation[47, 50]:

$$\frac{\partial G}{\partial t^*} + \vec{u}^* \cdot \vec{\nabla} G = s_L^* \left| \vec{\nabla} G \right| \tag{5}$$

where $\vec{u}$ is the flow velocity at the flame front and the superscript "*" denotes a dimensional variable.

The key assumptions made using this equation are that: (i) the flame is a thin, three-dimensional interface, dividing reactants and products, (ii) the flame position is a single-valued function of space and time, (iii) negligible density jump across the flame and (iv) the flame speed, s_L, is constant. Assumption (iii) is made implicitly as we prescribe the velocity field at the flame. In reality, the density jump across the flame alters the disturbance flow field, as discussed extensively in the literature[51-55]. In general, flames have finite density jumps, although the weak density jump across flames is an important limit in its own right, as many practical applications utilizing highly compressed or vitiated flows have small density jumps. An important qualitative effect introduced by the density jump is to introduce the Darrieus-Landau flame instability, where the approach flow field is altered in such a way as to cause amplification of flame wrinkles[54]. The character of this hydrodynamic instability is altered by harmonic forcing as well. For example, low amplitude harmonic excitation leads to stabilization of the hydrodynamic instability, while large amplitude forcing introduces a new parametric instability, resulting in oscillation of flame sheet at the subharmonic of the forcing frequency[56]. Assumption (iv) is a good approximation at lower frequencies – however, as shown by Preetham*et al.*[57] and Wang *et al.*[58], oscillatory curvature and/or hydrodynamic stretch can lead to modulation of the burning velocity, an effect that becomes important at high frequencies when the convective wavelength of the disturbance is of the same order of magnitude as the Markstein length.

Based on assumption (ii), we can convert $G(r,\theta,z,t)$ to an explicit flame position using the transformation $G = z^* - \xi^*(r,\theta,t)$ and applying the non-dimensional scheme: $u = u^*/U_o$, $r = r^*/L_f$, $z = z^*/L_f$, $\xi = \xi^*/L_f$, $s_L = s_L^*/U_o$ and $t = t^*/(L_f/U_o)$, where L_f is a characteristic flame length scale (flame height), and U_0 is a velocity scale (representative of the spatial flow field), we may write Eq.(5) in polar coordinates as:

$$\frac{\partial \xi}{\partial t}+u_r\frac{\partial \xi}{\partial r}+\frac{u_\theta}{r}\frac{\partial \xi}{\partial \theta}+s_L\left[\left(\frac{\partial \xi}{\partial r}\right)^2+\frac{1}{r^2}\left(\frac{\partial \xi}{\partial \theta}\right)^2+1\right]^{1/2}=u_z \tag{6}$$

flame length scale (flame height), and U_0 is a velocity scale (representative of the spatial flow field), we may write Eq.(5) in polar coordinates as:

$$\frac{\partial \xi}{\partial t}+u_r\frac{\partial \xi}{\partial r}+\frac{u_\theta}{r}\frac{\partial \xi}{\partial \theta}+s_L\left[\left(\frac{\partial \xi}{\partial r}\right)^2+\frac{1}{r^2}\left(\frac{\partial \xi}{\partial \theta}\right)^2+1\right]^{1/2}=u_z \tag{7}$$

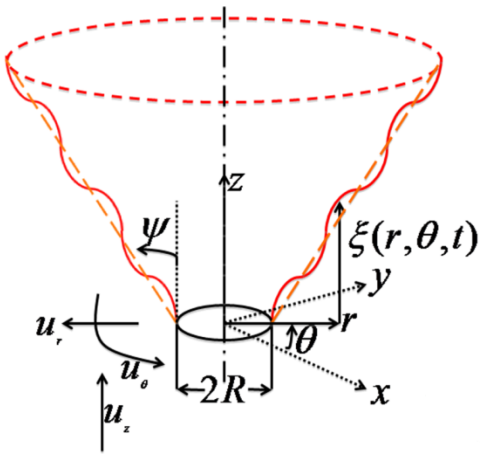

Figure 3 - Schematic of the center-body swirl-stabilized premixed flame [26].

The flame schematic provided in Figure 3 shows a center-body stabilized premixed flame in a swirling flow. The time averaged flame position is shown by the dashed line, and the perturbed flame by the solid line. The flame is stabilized on a center-body, which provides the following boundary condition for ξ:

$$\xi(r=R,\theta,t)\big|_{flame-holder}=0 \tag{8}$$

We write quantities at the flame location, in terms of a steady mean (overbar notation) and a spatio-temporally varying disturbance (superscript prime notation), as:

$$\begin{aligned}\xi(r,\theta,t)&=\bar{\xi}(r,\theta)+\varepsilon\xi'(r,\theta,t)\\ u_i(r,\theta,t)&=\bar{U}_i(r,\theta)+\varepsilon u_i'(r,\theta,t)\end{aligned} \tag{9}$$

where *i* denotes the *r*, θ, or *z* coordinate. Note that while the velocity field is a function of all three spatial components, we are only interested in its value at the mean flame locations, $z=\bar{\xi}(r,\theta)$, for this linear analysis. The evolution equations for the mean and linear perturbation in flame position may then be written as[20, 26]:

$$\bar{U}_r \frac{\partial \bar{\xi}}{\partial r} + \frac{\bar{U}_\theta}{r} \frac{\partial \bar{\xi}}{\partial \theta} = \bar{U}_z - s_L \left[\left(\frac{\partial \bar{\xi}}{\partial r} \right)^2 + \left(\frac{1}{r} \frac{\partial \bar{\xi}}{\partial \theta} \right)^2 + 1 \right]^{1/2} \tag{10}$$

$$\frac{\partial \xi'}{\partial t} + \vec{\bar{u}}_t \cdot \vec{\nabla} \xi' = \left(u'_z - u'_r \cot\psi - u'_\theta \frac{1}{r} \frac{\partial \bar{\xi}}{\partial \theta} \right) \tag{11}$$

where

$$\frac{\partial \bar{\xi}}{\partial r} = \cot\psi(r, \theta) \tag{12}$$

and the net tangential velocity vector along the flame surface, due to both the azimuthal and axial velocity components, is given by:

$$\vec{\bar{u}}_t = \vec{\bar{U}} - s_L \vec{e}_n \tag{13}$$

where $\vec{e}_n$ is the local unit normal vector, pointing from the time averaged flame surface into the products.

Equation (11) shows that flame wrinkles propagate along the flame surface in the direction given by, $\vec{\bar{u}}_t$. As shown in our prior study, the general characteristic equation for propagation of flame wrinkles in characteristic space coordinate *s*, is given by[26]:

$$\begin{aligned} ds &= \frac{dt}{1} = \frac{dr}{\left(\bar{U}_r - s_L \vec{e}_n \cdot \vec{e}_r \right)} = \frac{r d\theta}{\left(\bar{U}_\theta - s_L \vec{e}_n \cdot \vec{e}_\theta \right)} \\ ds &= \frac{dr}{\left(\bar{U}_r(r,\theta) - s_L \vec{e}_n \cdot \hat{e}_r \right)} \\ ds &= \frac{r d\theta}{\left(\bar{U}_\theta(r,\theta) - s_L \vec{e}_n \cdot \hat{e}_\theta \right)} \end{aligned} \Rightarrow \begin{aligned} r &= r(r_p, \theta_p, s) \\ \theta &= \theta(r_p, \theta_p, s) \end{aligned} \Rightarrow s_p = s_p(r_p, \theta_p) \tag{14}$$

Note that r_p and θ_p are the spatial coordinates corresponding to a characteristic coordinate $s = s_p$. The motion of disturbances along the flame are then given by:

$$\frac{\left(\bar{U}_\theta - s_L \vec{e}_n \cdot \vec{e}_\theta \right)}{\left(\bar{U}_r - s_L \vec{e}_n \cdot \vec{e}_r \right)} d \ln r = d\theta \tag{15}$$

Equation (15) shows the spiral flame surface wrinkle motion, whose specific trajectory depends on the local mean tangential velocity vector. The surface wrinkle motion is critically important in controlling the flame response to helical disturbances, as discussed further later.

The frequency domain representation of Eq. (11) is:

$$i2\pi St\hat{\xi}' + \left[\left(\overline{U}_r - s_L \vec{e}_n \cdot \vec{e}_r \right) \frac{\partial \hat{\xi}'}{\partial r} + \left(\overline{U}_\theta - s_L \vec{e}_n \cdot \vec{e}_\theta \right) \frac{1}{r} \frac{\partial \hat{\xi}'}{\partial \theta} \right] = \left(\hat{u}'_z - \hat{u}'_r \frac{\partial \overline{\xi}}{\partial r} - \hat{u}'_\theta \frac{1}{r} \frac{\partial \overline{\xi}}{\partial \theta} \right) \tag{16}$$

where the 'overhats' denote corresponding quantities in frequency domain. By substituting Eq.(1) for the velocity disturbance field, the solution to Eq.(16) can be obtained using characteristic transformation as:

$$\begin{aligned} &\hat{\xi}'(s_p) e^{i2\pi St s_p(r_p,\theta_p)} \\ &= \sum_{m=-\infty}^{\infty} \int_{s=0}^{s=s_p(r_p,\theta_p)} \left\{ e^{im\theta(r_p,\theta_p,s)+i2\pi Sts} \begin{bmatrix} \hat{B}_{z,m}\left(r(r_p,\theta_p,s), \overline{\xi}\left(r(r_p,\theta_p,s), \theta(r_p,\theta_p,s) \right), St \right) \\ -\dfrac{\partial \overline{\xi}}{\partial r} \hat{B}_{r,m}\left(r(r_p,\theta_p,s), \overline{\xi}\left(r(r_p,\theta_p,s), \theta(r_p,\theta_p,s) \right), St \right) \\ -\dfrac{1}{r}\dfrac{\partial \overline{\xi}}{\partial \theta} \hat{B}_{\theta,m}\left(r(r_p,\theta_p,s), \overline{\xi}\left(r(r_p,\theta_p,s), \theta(r_p,\theta_p,s) \right), St \right) \end{bmatrix} \right\} ds \end{aligned} \tag{17}$$

where $\hat{\xi}'(s_p) \equiv \hat{\xi}'(r_p, \theta_p)$. The flame response can be decomposed azimuthally as:

$$\hat{\xi}'(r, \theta, St) = \sum_{j=-\infty}^{\infty} e^{ij\theta} \hat{\xi}'_j(r, St) \tag{18}$$

Note that even within this linear framework, helical modes associated with the fluctuating flow-field do not necessarily translate to a corresponding azimuthal mode in the flame response for a general non-axisymmetric mean flow, i.e. a mode m in the flow field leads to a mode $j \neq m$ for the flame. For example, in a non-axisymmetric flame, an axisymmetric disturbance, $m = 0$, excites non-axisymmetric flame wrinkles.

The unsteady heat release per unit area of a premixed flame is given by $q = \rho s_L h_R$, where ρ is the fluid density, s_L is the laminar consumption speed and h_R is the heat of reaction. Thus, in a flame consuming homogeneous reactants and with a constant burning velocity, s_L, the heat release is directly proportional to the local surface area. Stretch sensitive flames that are wrinkled also introduce additional heat release fluctuations through flame speed oscillations[58]. This effect becomes significant when the radius of wrinkling and/or scale of the velocity gradient is of the same order of magnitude as the Markstein length and is not considered further in this study. The differential surface area is given by:

$$dA = r d\theta dr \sqrt{1 + \left(\frac{\partial \xi}{\partial r} \right)^2 + \left(\frac{1}{r} \frac{\partial \xi}{\partial \theta} \right)^2} \tag{19}$$

The global flame surface area, directly proportional to global heat release for constant burning velocity flames, is given by:

$$A = \iint_{r,\theta} r d\theta dr \sqrt{1 + \left(\frac{\partial \xi}{\partial r}\right)^2 + \left(\frac{1}{r}\frac{\partial \xi}{\partial \theta}\right)^2} \tag{20}$$

Recall from the discussion in the Introduction that the global heat release has a special significance for combustion noise and thermo-acoustic instability problems where the flame region is acoustically compact. Linearization of this equation yields the following decomposition for the global flame area:

$$\begin{aligned} \overline{A} &= \iint_{r,\theta} r dr d\theta \sqrt{1 + \left(\overline{\xi}_r\right)^2 + \left(\overline{\xi}_\theta / r\right)^2} \\ \hat{A}' &= \iint_{r,\theta} \left\{ r d\theta dr \frac{\left(\overline{\xi}_r \hat{\xi}'_r + \frac{1}{r^2}\overline{\xi}_\theta \hat{\xi}'_\theta\right)}{\sqrt{1 + \left(\overline{\xi}_r\right)^2 + \left(\overline{\xi}_\theta / r\right)^2}} \right\} \end{aligned} \tag{21}$$

where ξ_r and ξ_θ denote derivatives with respect to r and θ respectively. Thus, the fluctuations in local and global heat release can be calculated for a given problem by substituting the solutions for flame position in Eq.(17) into Eq.(21).

For axisymmetric mean flames, the global flame surface area can be simplified from Eq.(21), which leads to:

$$\begin{aligned} \overline{A} &= 2\pi \int_r r dr \frac{1}{\sin\psi(r)} \\ \hat{A}' &= \sum_{m=-\infty}^{\infty} \int_{\theta=0}^{\theta=2\pi} e^{im\theta} d\theta \int_r r dr \cos\psi(r) \frac{\partial \hat{\xi}'_m(r, St)}{\partial r} \end{aligned} \tag{22}$$

We can derive a very significant result for a general, axisymmetric flame shape from this expression. For non-axisymmetric modes ($m \neq 0$), the integral over θ is zero, which implies that only the axisymmetric $m = 0$ mode contributes to the global flame area. This also implies that the global flame area is independent of the swirl parameter St_Ω. The fluctuating flame area is then given by:

$$\hat{A}'_{m=0} = 2\pi \int_r \left\{ r \cos\psi(r) \frac{\partial}{\partial r} \left[e^{-i2\pi St s_p(r)} \int_{s=0}^{s=s_p(r)} \left\{ e^{i2\pi St s} \begin{bmatrix} \hat{B}_{z,0}(r, St, s) \\ -\frac{\partial \overline{\xi}}{\partial r} \hat{B}_{r,0}(r, St, s) \end{bmatrix} \right\} ds \right] \right\} dr \tag{23}$$

An important implication of these results is that helical modes, while introducing substantial wrinkling of the flame front, actually lead to no fluctuations in flame surface area in axisymmetric flows, a result that has also been experimentally verified[38].

For the case of non-axisymmetries in the mean flame/flow, first consider the case of weak non-axisymmetries. This weak non-axisymmetry is controlled by the small parameter η. We can decompose the flow-field and flame position as:

$$u_i\left(t,r,\theta\right)=\overline{U}_i(r)+\eta U_{\eta,i}(r,\theta)+\varepsilon u_i'\left(r,\theta,t\right) \tag{24}$$

$$\xi\left(r,\theta\right)=\overline{\xi}_0(r)+\eta\overline{\xi}_\eta(r,\theta)+\varepsilon\xi'(r,\theta,t) \tag{25}$$

The flame position fluctuations (in frequency domain) are then decomposed as:

$$\hat{\xi}'\left(\omega,r,\theta\right)=\hat{\xi}_0'\left(\omega,r,\theta\right)+\eta\hat{\xi}_\eta'\left(\omega,r,\theta\right) \tag{26}$$

Note that the axial coordinate *z* is not included in Eq.(24) since it is considered at the flame location given by $z=\xi(r,\theta)$. The strictly axisymmetric mean flame surface is governed by the equation:

$$\begin{aligned}\overline{U}_z-\overline{U}_r\frac{d\overline{\xi}_0}{dr}&=s_L\sqrt{1+\left(\frac{d\overline{\xi}_0}{dr}\right)^2}\\ \frac{d\overline{\xi}_0(r)}{dr}&=\cot\left(\psi\left(r\right)\right)\end{aligned} \tag{27}$$

The non-axisymmetric correction to the mean flame is governed by:

$$\left(\vec{\overline{U}}_t\cdot\vec{\nabla}\right)\overline{\xi}_\eta=U_{\eta,z}-U_{\eta,r}\frac{\partial\overline{\xi}_0\left(r\right)}{\partial r}=\frac{U_{\eta,n}\left(r,\theta\right)}{\sin\psi(r)} \tag{28}$$

where the subscript *n* corresponds to the normal component to the axisymmetric mean flame. This equation indicates that the asymmetries in the mean flame surface are governed by the normal component of the asymmetric part of the mean flow. Similarly, the flame wrinkling can be decomposed into its respective governing equations as:

$$i2\pi St\hat{\xi}_0'+\left(\vec{\overline{U}}_t\cdot\vec{\nabla}\right)\hat{\xi}_0'=\hat{u}_z'-\hat{u}_r'\frac{\partial\overline{\xi}_0\left(r\right)}{\partial r}=\frac{\hat{u}_n'}{\sin\left(\psi\left(r\right)\right)} \tag{29}$$

$$i2\pi St\hat{\xi}_\eta'+\left(\vec{\overline{U}}_t\cdot\vec{\nabla}\right)\hat{\xi}_\eta'=-\left(\vec{\hat{u}}'\cdot\vec{\nabla}\right)\overline{\xi}_\eta-\left(\vec{U}_\eta\cdot\vec{\nabla}\right)\hat{\xi}_0'-s_L\sin\left(\psi\left(r\right)\right)\left[\vec{\nabla}\overline{\xi}_\eta\cdot\vec{\nabla}\hat{\xi}_0'\right] \tag{30}$$

Equation (29) indicates that the leading order flame wrinkling is generated by the normal component of the flow fluctuations. However, in the case of Eq.(30) there are multiple sources of disturbances in the RHS. The first term on the right hand side indicates the interaction of mean flame asymmetries with flow disturbances. The second term indicates the interaction of mean flow asymmetries with the leading order local flame wrinkling. The third term is due to normal

propagation at the mean flame asymmetries interacting with the leading order local flame wrinkling. Note that all three terms contribute to the interaction of helical modes in the disturbance flow with the asymmetries in the mean flame. This is better explained using an example problem presented later.

For the case of strong non-axisymmetries in the mean flame/flow, the general solution to Eq.(6) is required. This requires the use of numerical methods. The spatial derivatives are discretized using a Weighted Essentially Non-Oscillatory (WENO)[59] scheme designed for Hamilton-Jacobi equations. This scheme is uniformly fifth order accurate in regions where the spatial gradients are smooth and third order accurate in discontinuous regions. Derivatives at the boundary nodes are calculated using fifth order accurate upwind-differencing schemes so that only the nodes inside the computational domain were utilized. A Total Variation Diminishing (TVD) Runge-Kutta scheme[60], up to third order accurate, was used for time integration and Local Lax-Friedrich (LLF) scheme, was used for improved stability [59].

The spatial grid is chosen based on resolving $1/100^{th}$ of the smallest length scale and the time-step is chosen to capture at least $1/1000^{th}$ of the forcing frequency. Note that the spatial grid is two-dimensional with both the radial and azimuthal directions. A typical grid (radial x azimuthal) ranges between 500x1000 to 1000x1000 grid points. The numerical solver was developed in the C language using OpenMP for parallel computing.

Now, we present calculations of *FTF* for example non-axisymmetric mean flames. Consider the following non-axisymmetric flow field:

$$\begin{aligned} \bar{U}_r &= 0 \\ \bar{U}_\theta &= 2\pi St(\Omega/\omega)r = 2\pi St\sigma r \\ \bar{U}_z &= 1+\eta U_{\eta,z}\left(\theta\right) \end{aligned} \tag{31}$$

Here, the mean flow asymmetries are considered only in the axial flow for illustration purposes. This mean flow asymmetry can be expressed in terms of its asymmetric modes as:

$$U_{\eta,z}\left(r,\theta\right) = A^u_{\eta,z,0}(r) + \sum_{n\geq 0} A^u_{\eta,z,n}(r)\cos n\theta + B^u_{\eta,z,n}(r)\sin n\theta \tag{32}$$

From Eq.(27), we have:

$$\bar{\xi}_0(r) = \left(r-R\right)\cot\psi = \tilde{r} \tag{33}$$

Using Eq.(28), the governing equation for the mean flame asymmetry is given by:

$$s_L\cos\psi\frac{\partial\bar{\xi}_\eta}{\partial r} + St_\Omega\frac{\partial\bar{\xi}_\eta}{\partial\theta} = U_{\eta,z}\left(r,\theta\right) \tag{34}$$

The solution is given by:

$$\overline{\xi}_{\eta}\left(\tilde{r},\theta\right)=A^{\xi}_{\eta,z,0}(\tilde{r})+\sum_{n\geq 0}A^{\xi}_{\eta,z,n}(\tilde{r})\cos n\theta+B^{\xi}_{\eta,z,n}(\tilde{r})\sin n\theta \tag{35}$$

where

$$\begin{aligned}
A^{\xi}_{\eta,z,0}(\tilde{r})&=\frac{1}{\cos^2\psi_0}\int_{s=0}^{s=\tilde{r}}A^{u}_{\eta,z,0}(R+s\tan\psi_0)ds\\
A^{\xi}_{\eta,z,n}(\tilde{r})&=\frac{1}{\cos^2\psi_0}\int_{s=0}^{s=\tilde{r}}\left[\begin{array}{l}A^{u}_{\eta,z,n}(R+s\tan\psi_0)\cos(nSt_{\Omega,2}(s-\tilde{r}))\\+B^{u}_{\eta,z,n}(R+s\tan\psi_0)\sin(nSt_{\Omega,2}(s-\tilde{r}))\end{array}\right]ds\\
B^{\xi}_{\eta,z,n}(\tilde{r})&=\frac{1}{\cos^2\psi_0}\int_{s=0}^{s=\tilde{r}}\left[\begin{array}{l}B^{u}_{\eta,z,n}(R+s\tan\psi_0)\cos(nSt_{\Omega,2}(s-\tilde{r}))\\-A^{u}_{\eta,z,n}(R+s\tan\psi_0)\sin(nSt_{\Omega,2}(s-\tilde{r}))\end{array}\right]ds
\end{aligned} \tag{36}$$

and $St_{\Omega,2}=St_{\Omega}\big/\cos^2\psi_0$. Now consider the axial velocity fluctuation given by:

$$\hat{u}'_{z,m}(\tilde{r},\theta)\big|_{flame}=\exp\left(-\frac{i2\pi\mathrm{St}}{k_c}\tilde{r}+im\theta\right) \tag{37}$$

where $\tilde{r}=\cot\psi\left(r-R\right)$. The leading order local flame wrinkling solution for Eq.(29) is given by:

$$\hat{\xi}'_{0,m}(\tilde{r},\theta)=\frac{1}{\cos^2\psi}\left[\frac{\sin\left(\pi\chi_L\tilde{r}\right)}{\left(\pi\chi_L\right)}\right]e^{-i2\pi St_2\tilde{r}-i2\pi mSt_{\Omega,2}\tilde{r}+i\pi\chi_L\tilde{r}} \tag{38}$$

where

$$\begin{aligned}
\chi_L&=St_2\left(\frac{1}{k_{c,L}}-m\sigma-1\right)=St_c-St_2-mSt_{\Omega,2}\\
St_2&=\frac{St}{\cos^2\psi}=\frac{fL_f}{U_0\cos^2\psi}=\frac{fL_f}{\overline{U}_{t,z}}\\
2\pi St_{\Omega,2}&=St_{\Omega}\big/\cos^2\psi=\Omega L_f\big/\overline{U}_{t,z}
\end{aligned} \tag{39}$$

In order to determine the correction to the leading order flame wrinkling behavior, Eq.(30) must be solved using Eqs.(36)-(38) as inputs. First the forcing function in the RHS needs to be determined. The three terms in the RHS need to be evaluated individually before the total forcing function is calculated. For the first term:

$$\begin{aligned}
&\hat{u}'_z\neq 0;\hat{u}'_r=\hat{u}'_\theta=0\\
&\overline{\xi}_{\eta}=\overline{\xi}_{\eta}(r,\theta)\\
&\Rightarrow-\left(\vec{\hat{u}}'\cdot\vec{\nabla}\right)\overline{\xi}_{\eta}=0
\end{aligned} \tag{40}$$

For the second term:

$$\begin{aligned} &U_{\eta,z} \neq 0; U_{\eta,r} = U_{\eta,\theta} = 0 \\ &\hat{\xi}_0' = \hat{\xi}_0'(St, r, \theta) \\ &\Rightarrow -\left(\vec{U}_\eta \cdot \vec{\nabla}\right)\hat{\xi}_0' = 0 \end{aligned} \tag{41}$$

For the third term:

$$-s_L \sin\left(\psi(r)\right)\left[\vec{\nabla}\overline{\xi}_\eta \cdot \vec{\nabla}\hat{\xi}_0'\right] = -\sin^2\psi\left[\frac{\partial\overline{\xi}_\eta}{\partial r}\frac{\partial\hat{\xi}_0'}{\partial r} + \frac{1}{r^2}\frac{\partial\overline{\xi}_\eta}{\partial\theta}\frac{\partial\hat{\xi}_0'}{\partial\theta}\right] \tag{42}$$

In order to evaluate the third term above, consider only the *n*-th mode asymmetry in the mean flame shape (Eq.(35)) and the *m*-th mode flame response in the leading order flame wrinkling (Eq.(38)). We shall denote this interaction by $RHS_{n,m}$. We can rewrite Eq.(35), in the form:

$$\overline{\xi}_\eta\left(\tilde{r},\theta\right) = A^{\xi}_{\eta,z,0}(r) + \frac{1}{2}\sum_{n\neq 0}\left[A^{\xi}_{\eta,z,n}(r) + sign(n) iB^{\xi}_{\eta,z,n}(r)\right]e^{in\theta} \tag{43}$$

Using this, we have:

$$RHS_{n,m} = -e^{i(n+m)\theta}\sin^2\psi_0\begin{pmatrix}\frac{d}{dr}\left[\left(A^{\xi}_{\eta,z,n}(r) - iB^{\xi}_{\eta,z,n}(r)\right)\right]\frac{d}{dr}\left[\hat{\xi}_{0,m}'(\tilde{r})\right] + \\ \frac{1}{r^2}\left[-nm\left(A^{\xi}_{\eta,z,n}(r) - iB^{\xi}_{\eta,z,n}(r)\right)\hat{\xi}_{0,m}'(\tilde{r})\right]\end{pmatrix} \tag{44}$$

The resulting flame response correction due to this forcing function can be expressed as $\hat{\xi}'_{\eta,n,m}$, where (from Eq.(30)):

$$i2\pi St\hat{\xi}'_{\eta,n,m} + \left(\vec{\vec{U}}_t(r)\cdot\vec{\nabla}\right)\hat{\xi}'_{\eta,n,m} = RHS_{n,m} \tag{45}$$

Note that this corresponds to a system where the forcing function has a combined azimuthal mode $(n+m)$. Note that Eq.(29), Eq.(30) and Eq.(45) are similar in their operators in their respective LHS. Hence, their mathematical behavior for their respective RHS would also be similar for the same forcing function. We have seen earlier that only the symmetric mode of the forcing function contributes finitely to the global flame response. Hence for cases where $n+m=0$, the global response is finite. This implies that the asymmetries in the mean flow ($n\neq 0$) can interact with helical modes in the disturbance field ($m\neq 0$) leading to changes in the global flame response. Thus, for asymmetric mean flames, helical modes are important from a global flame response

perspective. The importance of a particular helical mode is dictated by the presence of a corresponding mode of opposite sign in the asymmetric mean flame/flow.

For the purposes of illustration, consider an example flow field where:

$$\begin{aligned} A^{u}_{\eta,z,0} &= 0 \\ A^{u}_{\eta,z,n} &= B^{u}_{\eta,z,n} = 1 \end{aligned} \tag{46}$$

From a global flame response perspective, only the cases where $n+m=0$ are considered. Hence, we first consider the asymmetric modes $n=-m$ in Eq.(36):

$$\begin{aligned} A^{\xi}_{\eta,z,-m}(\tilde{r}) &= \frac{1+\sqrt{2}\sin\left(mSt_{\Omega,2}\tilde{r}-\pi/4\right)}{mSt_{\Omega}} \\ B^{\xi}_{\eta,z,-m}(\tilde{r}) &= \frac{\sqrt{2}\sin\left(mSt_{\Omega,2}\tilde{r}+\pi/4\right)-1}{mSt_{\Omega}} \end{aligned} \tag{47}$$

Using Eq.(38), Eq.(44) and Eq.(47) in Eq.(45), we have the solution:

$$e^{i2\pi St_2\tilde{r}}\hat{\xi}'_{\eta,-m,m}\left(\tilde{r}\right) = I_1 + I_2 + \frac{im\tan^2\psi_0}{4\pi St_{\Omega}\chi_L}\left(I_3+I_4+I_5+I_6\right) \tag{48}$$

The integrals are defined as:

$$I_1 = -\int_0^{\tilde{r}/\cos^2\psi_0} \frac{1}{2}\left(1-\frac{St_2(1+m\sigma)}{\chi_L}\right)e^{i\alpha_1 s}ds = \frac{1}{2i\alpha_1}\left(1-\frac{St_2(1+m\sigma)}{\chi_L}\right)\left(1-e^{i\alpha_1\tilde{r}/\cos^2\psi_0}\right) \tag{49}$$

$$I_2 = \int_0^{\tilde{r}/\cos^2\psi_0} \frac{1}{2}\left(\frac{St_2(1+m\sigma)}{\chi_L}\right)e^{i\alpha_2 s}ds = \frac{1}{2i\alpha_2}\left(\frac{St_2(1+m\sigma)}{\chi_L}\right)\left(e^{i\alpha_1\tilde{r}/\cos^2\psi_0}-1\right) \tag{50}$$

$$I_3 = \int_0^{\tilde{r}/\cos^2\psi_0}\left[\frac{e^{i(\alpha_3+\alpha_4+\alpha_5)s}}{\left(R+s\cos\psi_0\sin\psi_0\right)^2}\right]ds \tag{51}$$

$$I_4 = -\int_0^{\tilde{r}/\cos^2\psi_0}\left[\frac{e^{i(\alpha_5+\alpha_3-\alpha_4)s}}{\left(R+s\cos\psi_0\sin\psi_0\right)^2}\right]ds \tag{52}$$

$$I_5 = -\int_0^{\tilde{r}/\cos^2\psi_0}\left[\frac{e^{i(\alpha_5-\alpha_3+\alpha_4)s}}{\left(R+s\cos\psi_0\sin\psi_0\right)^2}\right]ds \tag{53}$$

$$I_6 = \int_0^{\tilde{r}/\cos^2\psi_0} \left[\frac{e^{i(\alpha_5-\alpha_3+\alpha_4)s}}{\left(R + s\cos\psi_0 \sin\psi_0\right)^2} \right] ds \tag{54}$$

where

$$\begin{aligned}
\alpha_0 &= -2\pi St_2(1+m\sigma) + 2\pi St\sigma m \\
\alpha_1 &= \left(2\pi\chi_L \cos^2\psi_0 + \alpha_0 \cos^2\psi_0 + 2\pi St\right) \\
\alpha_2 &= \left(\alpha_0 \cos^2\psi_0 + 2\pi St\right) \\
\alpha_3 &= 2\pi St\sigma m \cos^2\psi_0 \\
\alpha_4 &= \pi\chi_L \cos^2\psi_0 \\
\alpha_5 &= \alpha_0 \cos^2\psi_0 - \pi mSt\sigma \cos^2\psi_0 + \pi\chi_L \cos^2\psi_0
\end{aligned} \tag{55}$$

and

$$\int_0^{\tilde{r}/\cos^2\psi_0} \left[\frac{\cos\psi_0 \sin\psi_0 e^{i\beta s}}{\left(R + s\cos\psi_0 \sin\psi_0\right)^2} \right] ds = \left\{ \left[\frac{1}{R} - \frac{e^{i\beta\,\tilde{r}/\cos^2\psi_0}}{r} \right] + i\beta e^{\frac{i\beta R}{\cos\psi_0 \sin\psi_0}} \left[\begin{array}{l} Ei\left(\dfrac{i\beta r}{\cos\psi_0 \sin\psi_0} \right) \\ -Ei\left(\dfrac{i\beta R}{\cos\psi_0 \sin\psi_0} \right) \end{array} \right] \right\}$$

$$Ei(x) = -\int_{-x}^{\infty} \frac{e^{-s}}{s} ds$$

(56)

Using these solutions for weak asymmetries, we apply them to example flames shapes that have: (i) Elliptic cross-section and (ii) Square cross-section. These are performed using a numerical solver, detailed in Appendix B, where the numerical methods and the parallel system used for its computations are detailed.

The effects of mean flame asymmetry are understood by comparing the Flame Transfer Function (*FTF*) which in these examples is defined as:

$$FTF = \frac{\hat{A}'/\bar{A}}{\varepsilon} \tag{57}$$

A. Elliptic cross-section

Single flames in axisymmetric geometries are axisymmetric. However, when such a flame is confined in a non-axisymmetric combustor, like those with rectangular cross-sections, flame asymmetries are possible. Specifically if the confinement is significant in one direction compared to the other, the single flame shapes can deviate from a circular cross-section to that of an ellipse. The asymmetric mean flame for this example is given by:

$$\overline{\xi}(\tilde{r},\theta) = \overline{\xi}_0(\tilde{r})\sqrt{1-\eta\cos^2\theta} \tag{58}$$

Here, $\overline{\xi}_0(\tilde{r}) = \tilde{r}$ from Eq.(33). The azimuthal variation in position is shown in Figure 4 for different values of the asymmetry parameter η. Note that for $\eta = 0$ we retrieve the axisymmetric mean flame given by Eq.(33). As this value is increased, the cross-section eccentricity increases. Note that the elliptic cross-section is valid only for $0 < \eta \leq 0.5$. For $0.5 < \eta \leq 1.0$, the flame shape is akin to that of two interacting flames. In this analysis, we shall focus on $\eta < 0.5$.

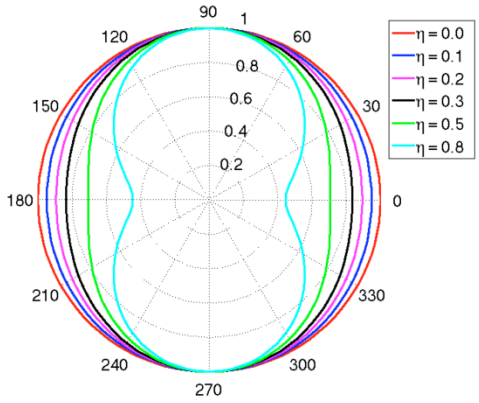

Figure 4 - Elliptic flame cross-section denoted by $\overline{\xi}(\tilde{r},\theta)/\overline{\xi}_0(\tilde{r})$ for varying η.

For the case of weak asymmetries, the mean flame shape correction can be expressed as (using Taylor expansion to first order):

$$\overline{\xi}_\eta(r,\theta) = \tilde{r}\left(-\frac{1}{4} - \frac{1}{4}\cos 2\theta\right) \tag{59}$$

Hence, we have:

$$\begin{aligned} A^{\xi}_{\eta,z,0}(\tilde{r}) &= A^{\xi}_{\eta,z,n=2}(\tilde{r}) = -\frac{1}{4}\tilde{r} \\ A^{\xi}_{\eta,z,n\neq 0,2}(\tilde{r}) &= B^{\xi}_{\eta,z,n}(\tilde{r}) = 0 \qquad \forall n \geq 0 \end{aligned} \tag{60}$$

Since we are specifying the mean flame shape here, the mean flow field can be obtained using Eq.(34):

$$U_{\eta,z}(r,\theta) = -\left(\frac{\cos^2\psi}{4}\right) - \left(\frac{\cos^2\psi}{4}\right)\cos 2\theta + St_\Omega\left(\frac{\tilde{r}}{2}\right)\sin 2\theta \tag{61}$$

This results in the following asymmetric mode coefficients:

$$A^u_{\eta,z,0}(\tilde{r}) = A^u_{\eta,z,n=2}(\tilde{r}) = -\left(\frac{\cos^2\psi}{4}\right)$$

$$B^u_{\eta,z,n=2}(\tilde{r}) = St_\Omega \frac{\tilde{r}}{2} \tag{62}$$

$$A^u_{\eta,z,n\neq 0,2}(\tilde{r}) = B^u_{\eta,z,n\neq 2}(\tilde{r}) = 0 \qquad \forall n \geq 0$$

These equations show that for a weakly asymmetry flame with an elliptic cross-section, there exists only the asymmetric modes: $n = 0, \pm 2$. For a symmetric mode $m = 0$ in the disturbance field, the global flame response is corrected due to the $n = 0$ mode in the mean non-axisymmetry. The $n = \pm 2$ mode in the mean flow/flame asymmetry interacts with the helical modes $m = \mp 2$ in the flow disturbance, leading to a finite global flame response. For the example calculations presented next, we consider three cases: (i) Effect of η on the *FTF* amplitude, (ii) Effect of swirl (St_Ω) on the *FTF* amplitude and (iii) Effect of Flame angle on the *FTF* amplitude.

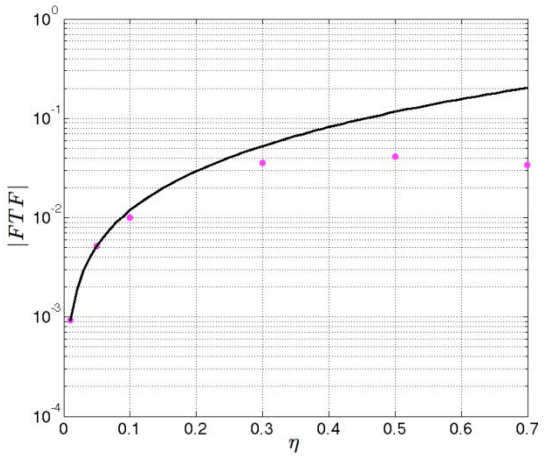

Figure 5 - Comparison of *FTF* amplitude for an elliptic flame computed using analytical solution in Eq.(48) (black curve) and numerical solver (pink circles) for increasing values of η. Flow disturbance contains the $m = 2$ mode with $St_2 = 2.0$ and $k_c = 0.8$. Note that $St_2 = fL_f / U_0 \cos^2\psi$.

First consider the effect of η on the *FTF* as shown in Figure 5. The flow disturbance comprises of a helical mode of $m = 2$. As seen in the figure, for low values of η, the *FTF* amplitude is low as expected and increases with increasing value of η. For values of $\eta < 0.1$, there is a reasonable match between the *FTF* obtained using the numerical solver and that obtained using the asymptotic solution shown in Eq.(48).

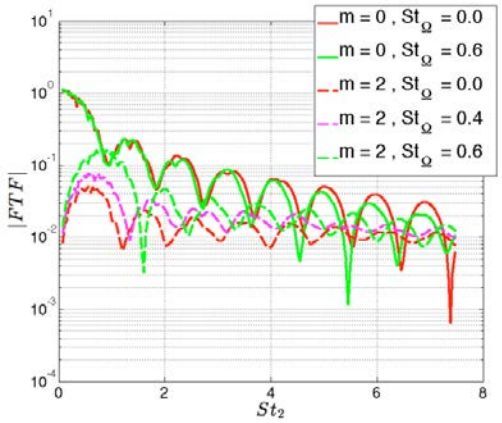

Figure 6 - Comparison of *FTF* amplitude for an elliptic flame, for different values of St_Ω for an elliptic flame with $\eta = 0.5, \psi = 15^o$, in response to a flow disturbance helical mode of $m = 2$ and $k_c = 0.8$. Note that $St_2 = fL_f / U_0 \cos^2 \psi$.

Next, consider the effect of swirl number on the FTF amplitude. This is shown in Figure 6 for the elliptic flame of $\eta = 0.5$. The solid curves denote the response of this asymmetric flame to a symmetric flow disturbance (*m*=0). Note that the low Strouhal number transfer function begins from unity and then decreases with increasing Strouhal number. In the case of perfectly axisymmetric mean flames, the swirl component had no effect on the global *FTF* amplitude. However, for the case of asymmetric mean flames, this is not true. This is shown by the comparison of the *FTF* amplitude for two different values of St_Ω. The non-swirling case is indicated by the solid red curve and the swirling case ($St_\Omega = 0.6$) is indicated by the solid green curve. As the value of St_2 is increased, the *FTF* amplitudes deviate from each. This deviation indicates both a change in the interference Strouhal numbers and also a change in the amplitude. This can be attributed to the change in interference effects introduced by the transport of wrinkles on the asymmetric flame surface by the swirling flow. Finally, the effect of flame angle on the results is shown in Figure 7.

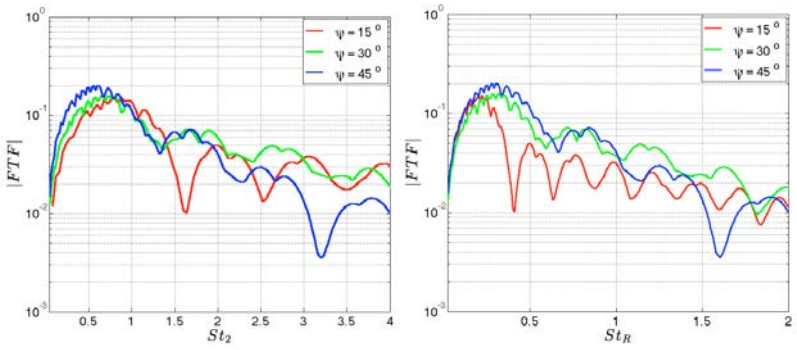

(a) **(b)**

Figure 7 - **Effect of Flame angle on the *FTF* amplitude variation for an elliptic flame with** $\psi = 15^o, St_\Omega = 0.5, \eta = 0.5, m = 2$ **and** $k_c = 0.8$**. (a) Variation with** $St_2 = fL_f / U_0 \cos^2 \psi$ **and (b) Variation with** $St_R = fR/U_0$**.**

B. Square cross-section

In this sub-section, we consider example calculations for a flame with a square cross-section. Such an asymmetry is possible in the case of flame-flame interactions, such as shown earlier in Figure 2. The asymmetric mean flame for this example is given by:

$$\overline{\xi}(\tilde{r},\theta) = \overline{\xi}_0(\tilde{r})\left[\left(\cos\theta\right)^{2+2\eta} + \left(\sin\theta\right)^{2+2\eta}\right]^{1/(2+2\eta)} \tag{63}$$

Here, $\overline{\xi}_0(\tilde{r}) = \tilde{r}$ from Eq.(33). Note that η must be an integer for the expression to be valid. Hence, unlike the elliptic flame case, a weak asymmetry analysis cannot be performed for this flame due to the analytical nature of Eq.(63). A representative asymmetric mean flame shape is shown in Figure 8 for $\eta = 1$.

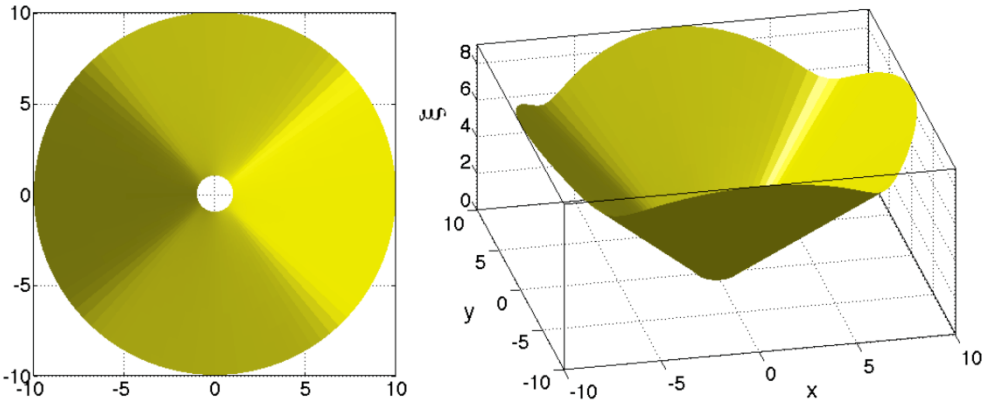

(a) **(b)**

Figure 8 - Flame surface for $\eta = 1$, showing (a) view along the axial flow direction and (b) isometric view from the side, with surface shading indicating the asymmetry of the mean flame surface. The hole in the center corresponds to the centerbody rim. The outer radial extent of the domain is 10 times the centerbody radius.

The azimuthal variation is shown in Figure 9(a). Note that the periodicity is of order $n = 4$. This is also reflected in Figure 9(b) which shows the modal coefficients. Note that modes that are multiples of $n = 4$ have dominant amplitudes compared to the other modes.

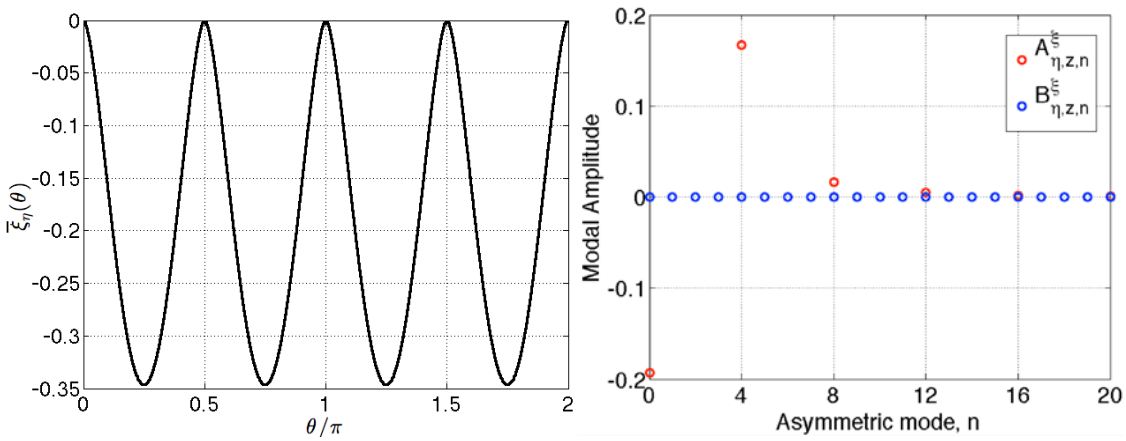

(a) **(b)**

Figure 9 - Square flame with $\eta = 1$ showing (a) Azimuthal variation of the mean flame shape and (b) Asymmetric modal coefficients.

The modal coefficients are given by:

$$A^{\xi}_{\eta,z,n=0}(\tilde{r}) = -0.1931\tilde{r} \qquad A^{\xi}_{\eta,z,n=4}(\tilde{r}) = 0.1667\tilde{r} \qquad A^{\xi}_{\eta,z,n=8}(\tilde{r}) = 0.0167\tilde{r}$$
$$B^{\xi}_{\eta,z,n}(\tilde{r}) \approx 0.0 \tag{64}$$

Note that only the $n = 0$ and $n = 4$ modes are significant and all other modes are an order of magnitude lower or more.

For a symmetric mode $m = 0$ in the disturbance field, the global flame response is corrected due to the $n = 0$ mode in the mean non-axisymmetry. The $n = \pm 4$ modes in the mean flow/flame asymmetry interacts with the helical modes $m = \mp 4$ (and its multiples respectively) in the flow disturbance, leading to a finite global flame response. In the example calculations we consider only the $\eta = 1.0; m = 0, 4$ modes.

Figure 10 shows the effect of swirl on the *FTF* amplitude for an axisymmetric flow disturbance (*m*=0). As the value of St_Ω is increased, the *FTF* amplitude shows little difference. However, in comparison with the reference case, the asymmetric mean flame case shows a shift in the interference location. This change is attributed directly to the asymmetry of the mean flame interacting with the swirl transport of wrinkles.

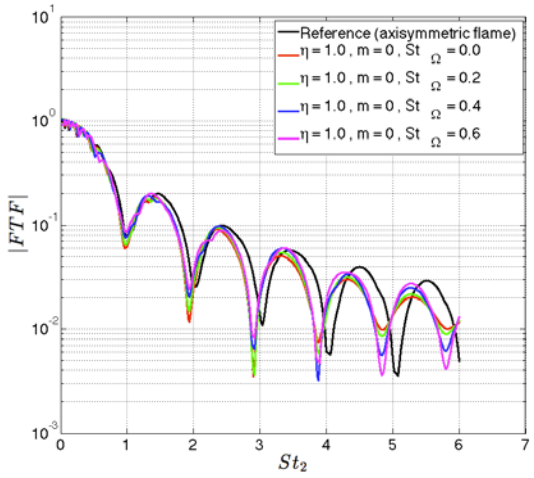

Figure 10 - Comparison of *FTF* amplitudes for a square flame responding to a symmetric flow disturbance, for different values of swirl parameter St_Ω and $k_c = 0.8$. Note that $St_2 = fL_f / U_0 \cos^2 \psi$.

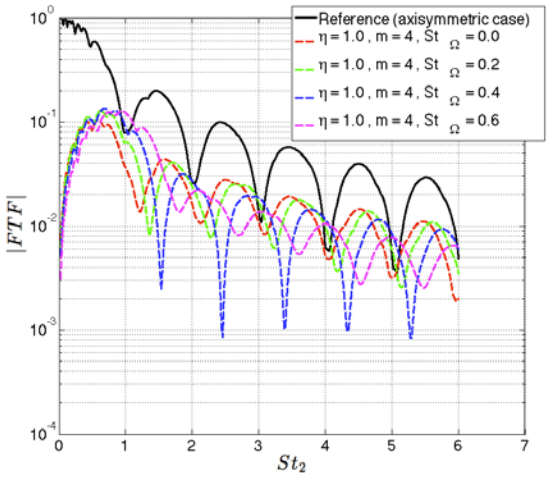

Figure 11 - Comparison of *FTF* amplitudes for a square flame responding to helical flow disturbance of mode *m*=4, for different values of swirl parameter St_Ω and $k_c = 0.8$. Note that $St_2 = fL_f / U_0 \cos^2 \psi$.

In contrast, consider the comparison shown in Figure 11. This figure shows the *FTF* amplitude under the presence of a helical flow disturbance ($m = 4$). As mentioned in earlier chapters, the asymmetric mode helical flow disturbance has no finite *FTF* amplitude for axisymmetric flames. However, the plots clearly show the finite *FTF* amplitudes. As the swirl number is increased, the interference pattern in Strouhal space is changed. Specifically there is a shift in the curves to the left and a decrease in amplitude. Depending upon the Strouhal number in question, the *FTF* amplitude is comparable to the reference case, indicating the importance of helical modes in controlling global *FTF* of asymmetric mean flames. Finally, the effect of flame angle on the results is shown in Figure 12.

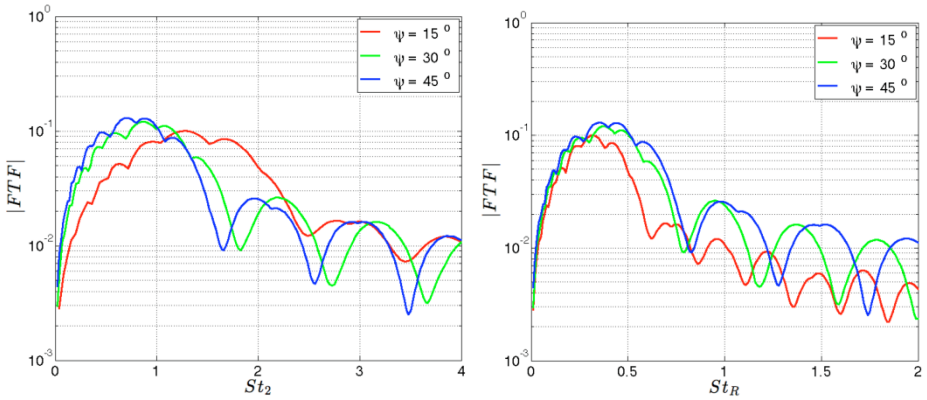

(a) **(b)**

Figure 12 - Effect of flame angle of a square flame on the *FTF* amplitude variation for $St_\Omega = 0.5,\ \eta = 1,\ m = 4$ and $k_c = 0.8$. Note that $St_2 = fL_f / U_0 \cos^2 \psi$. (a) Variation with $St_2 = fL_f / U_0 \cos^2 \psi$ and (b) Variation with $St_R = fR/U_0$.

These results clearly indicate the variation of the *FTF* amplitude due to different helical modes in the disturbance field for different control parameters. For low Strouhal number, the symmetric contribution to the *FTF* is dominant and the contribution from the asymmetric helical modes is negligible. However for intermediate Strouhal numbers, these asymmetric helical modes in the flow disturbance lead to significant *FTF* that are comparable to that due to the symmetric flow disturbance. Additionally, the *FTF* interference patterns are affected by the extent of swirl in the mean flow.

4.0 Turbulent Local Consumption Speed Analysis

The overall goal of this portion of work done during the reporting period was to determine the effect of flame curvature (due to harmonic forcing) on the turbulent local consumption speed, S_C. The local consumption speed is a definition of flame speed based on the rate at which reactants are consumed. In the wrinkled flamelet regime, the consumption speed can be defined as:

$$S_L \cdot A_{\text{Instantaneous}} = S_C \cdot \bar{A} \tag{65}$$

where $\bar{A}$ is a suitable reference area.

To investigate these effects, work has focused on analysis of data from pre-mixed flame modeling based on the G-equation, performed by Dong-Hyuk Shin. However, there is some ambiguity regarding the definition of $\bar{A}$, based on this computational data, as shown in Figure 13.

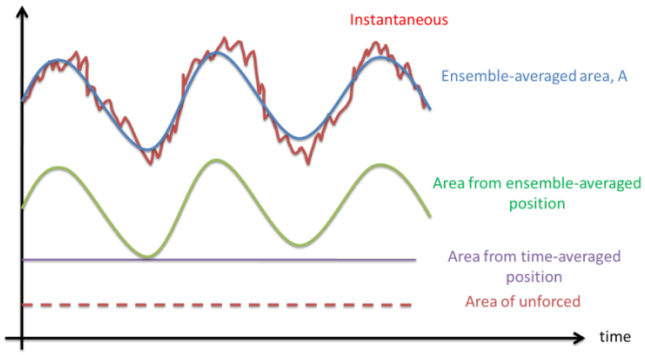

Figure 13 - Illustration of different definitions of $\overline{A}$.

Using these different definitions, S_C was calculated. A comparison of the different methods is shown in Figure 14.

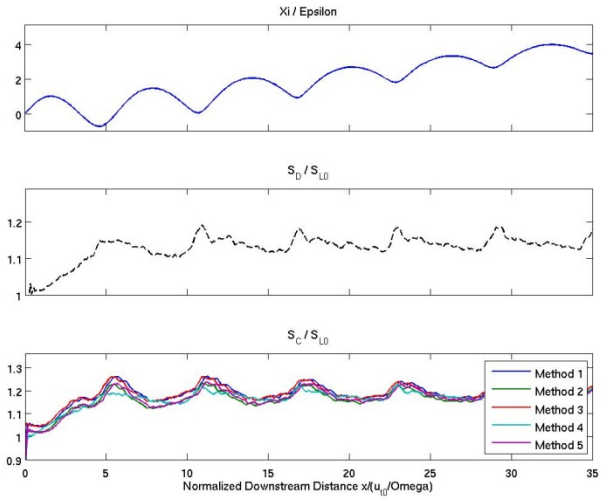

Figure 14 - Flame position, normalized displacement speed and normalized consumption speed from a representative data set

Method four (calculated as shown in Eqn.(66)) was found to provide the most useful normalization:

$$A_0(s,t) = \sqrt{1 + \left(\frac{\partial \langle \xi \rangle}{\partial s} \right)^2}\, ds \cdot dz \tag{66}$$

The computationally calculated turbulent consumption speed was then compared to the computationally determined displacement speed, as shown in Figure 15.

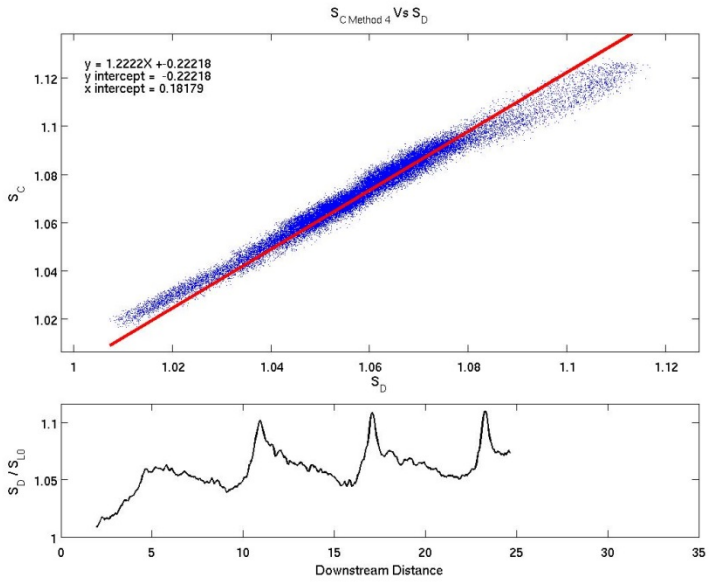

Figure 15 - Turbulent consumption speed versus displacement speed and ratio of displacement speed to consumption speed for a representative data set.

By determining the slope of the regression line between consumption and displacement speed, we are able to relate the turbulent displacement speed directly to the consumption speed. This allows us to determine the computational, ensemble averaged heat release, as follows:

$$\left\langle dq(s,t)\right\rangle = \left\langle \rho_u h_R S_L dA\right\rangle \tag{67}$$

$$S_L\left\langle dA(s,t)\right\rangle = S_C(s,t)\sqrt{1+\left(\frac{\partial\langle\xi\rangle}{\partial s}\right)^2}\,ds \tag{68}$$

$$\left(\frac{S_C(s,t)}{S_L}-1\right) = C\left(\frac{S_{T,eff}(s,t)}{S_L}-1\right) \tag{69}$$

where C is the slope of the regression line between S_c and S_d.

$$S_C(s,t) = S_L\left[C\left(\frac{S_{T,eff}(s,t)}{S_L}-1\right)+1\right] \tag{70}$$

$$\left\langle dq(s,t)\right\rangle = \rho_u h_R S_L\left\{C\left(\frac{S_{T,eff}(s,t)}{S_L}-1\right)+1\right\}\sqrt{1+\left(\frac{\partial\langle\xi\rangle}{\partial s}\right)^2}\,ds \tag{71}$$

Eqn. (71) thus gives an expression for the local, ensemble averaged heat release, which may then be extended to determine a computational flame transfer function.

Following this initial inquiry, the focus of this work shifted to determining analytical flame transfer functions. This was done using the G-equation, and the derived ξ-equation. Principally, this work focused on reconciling differences in the analytical, laminar, linear flame transfer function derived with bulk forcing in three different coordinate systems for a two-dimensional, bluff body-anchored flame: A laboratory-oriented coordinate system (system 1), with the flame position a function of the transverse coordinate, a laboratory-oriented coordinate system with the flame position a function of the axial coordinate (system 2), and a mean flame-oriented coordinate system with the flame position a function of the flame coordinate (system 3), shown in Figure 16.

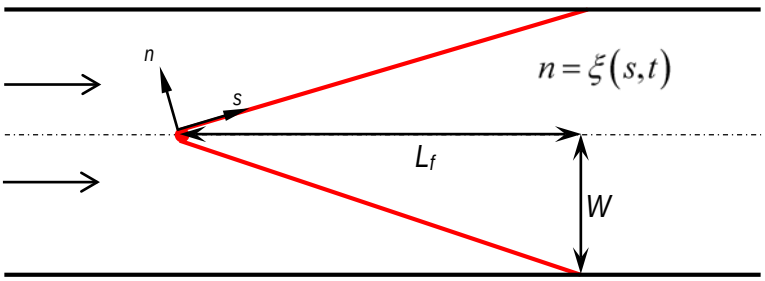

Figure 16 - Schematic of the flame-oriented coordinate system.

Although the flame transfer function should be independent of the coordinate system under which it derived, it is found that, in the flame-oriented system, the linear transfer function is 0, while in the laboratory coordinate system it varies depending on the orientation of the flame position function. Eqn. (72) shows the flame transfer function for the laboratory system, with flame position oriented axially:

$$FTF_{axial,LC}=\frac{2}{St}\frac{\beta^2}{\left(\beta^2+1\right)}\sin\left(\frac{St}{2}\frac{\beta^2+1}{\beta^2}\right)e^{i\frac{St}{2}\frac{\beta^2+1}{\beta^2}} \tag{72}$$

where $\beta=L_f/W$, is the flame aspect ratio and *St* is the Strouhal number. Similarly, Eqn.(73) gives the flame transfer function for the laboratory-oriented coordinate system, with transversely oriented flame position function:

$$FTF_{\text{trans},LC}=-\frac{2}{St}\frac{1}{\left(\beta^2+1\right)}\sin\left(\frac{St}{2}\frac{\beta^2+1}{\beta^2}\right)e^{i\frac{St}{2}\frac{\beta^2+1}{\beta^2}} \tag{73}$$

In order to reconcile the differences in these three systems, work during this reporting period focused on identifying a correction factor necessary to account for the fact that the flame tip moves periodically. In systems where the flame position function is not oriented parallel to the wall, this flame movement causes the limit of integration to change when determining the spatially integrated heat release. Whereas, in systems with the flame position function oriented parallel to the wall, and normal to the direction of integration, integration to the wall accounts for flame tip fluctuations.

After reconciling the laminar flame transfer functions, work returned to identifying a flame transfer function in the turbulent case. Understanding the correction factor from the laminar cases is important and can be extended to the turbulent case, with a mean-flame oriented coordinate system. For the turbulent flame transfer function, the flame position will be based on the following equation:

$$\frac{\partial\langle\xi\rangle}{\partial t}+\langle u_s\rangle\frac{\partial\langle\xi\rangle}{\partial s}-\langle u_n\rangle+\langle u_z\rangle\frac{\partial\langle\xi\rangle}{\partial z}=S_{T,eff}\left[1+\left(\frac{\partial\langle\xi\rangle}{\partial s}\right)^2+\left(\frac{\partial\langle\xi\rangle}{\partial z}\right)^2\right]^{1/2} \tag{74}$$

The effective flame speed will be modeled as:

$$S_{T,eff}=S_{T,0}\left(1-\sigma_T\langle c\rangle\right) \tag{75}$$

where

$$\langle c\rangle=\frac{\partial^2\langle\xi(s,t)\rangle/\partial s^2}{\left[1+\left(\partial\langle\xi(s,t)\rangle/\partial s\right)^2\right]^{3/2}} \tag{76}$$

and σ_T is the 'turbulent Markstein length'. Once a linearized solution to this problem was, a flame transfer function could be determined and compared with the computational results discussed previously.

As mentioned previously, this portion of our work describes the influence of coordinate systems and integration limits on global flame transfer functions (FTF). The front tracking approach forms the basis of the flame response modeling used here, where the flame position is the zero contour of the implicit function, $G(\vec{x},t)$,whose dynamics are described by the familiar G-equation.

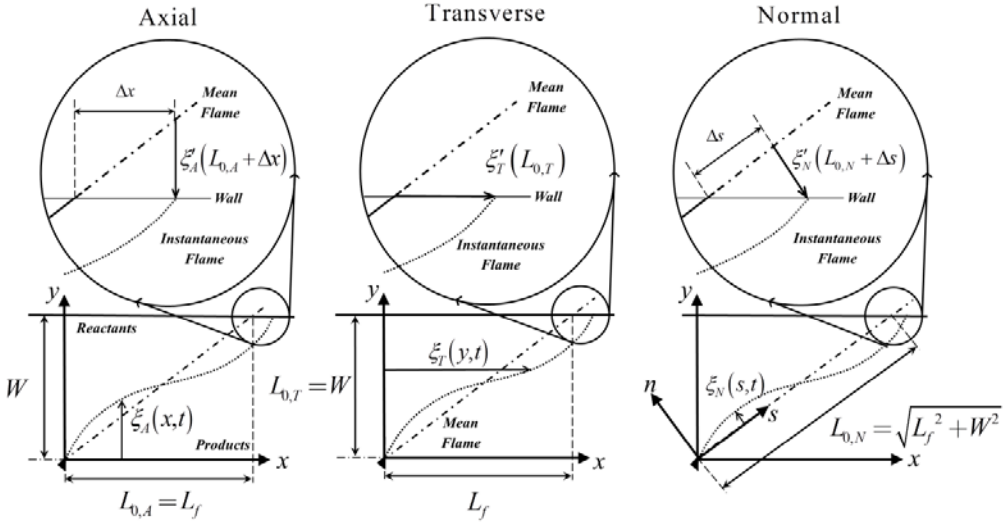

Figure 17 - Schematic of coordinate systems showing end correction factor.

As shown in Figure 17, $G(\vec{x},t)$ can be written as an explicit flame position, ξ, by defining the location of the instantaneous flame sheet with respect to some coordinate system. Previous studies have defined the flame position with respect to the axial coordinate, transverse coordinate, or in a coordinate system normal to the time averaged flame position. For example, the resulting expression written in the axial coordinate system is:

$$\frac{\partial \xi_A}{\partial t} + u_x \frac{\partial \xi_A}{\partial x} - u_y + u_z \frac{\partial \xi_A}{\partial z} = s_f \left[\left(\frac{\partial \xi_A}{\partial x} \right)^2 + \left(\frac{\partial \xi_A}{\partial z} \right)^2 + 1 \right]^{1/2} \tag{77}$$

Here, $\xi_A \equiv \xi_A(x,z,t)$. The reasons for using different coordinate systems depend upon the particular focus of the study. The majority of studies have used a transverse coordinate system. However, some have used the normal coordinate system for their discussion of the local space-time dynamics of the flame sheet, as they are most naturally evident in that coordinate system. The axial coordinate system has been used for other studies, where the position of shallow angle flames remains a single valued function of the coordinate for much larger amplitudes in that coordinate system.

Focusing on linearized flame area dynamics, the flame area transfer function is defined as:

$$G(\omega) = \frac{\hat{A}'(\omega)/A_0}{\hat{u}'_{ref}/u_0} \tag{78}$$

The instantaneous flame area is given by:

$$A(t) = \int_0^{L(t)} dA(t) \tag{79}$$

Equation (79) can be expanded as follows to show the individual contributing terms:

$$A(t) = \underbrace{\int_0^{L_0} dA_0}_{\text{Unperturbed Area}} + \underbrace{\int_{L_0}^{L(t)} dA_0}_{\text{Length fluctuation of mean flame due to oscillating end correction}} + \underbrace{\int_0^{L_0} dA'}_{\text{Area fluctuation due to wrinkling on mean flame}} + \underbrace{\int_{L_0}^{L(t)} dA'}_{\text{Area fluctuation of oscillating end correction}} \tag{80}$$

Note that the last term in eqn. (80) is second order in disturbance amplitude. Therefore, the leading order perturbation to this flame area is given by:

$$A'(t) = A(t) - A_0 = \underbrace{\int_{L_0}^{L(t)} dA_0}_{\text{Length fluctuation of mean flame}} + \underbrace{\int_0^{L_0} dA'}_{\text{Area fluctuation due to wrinkling on mean flame}} \tag{81}$$

where A_0 is the area of the unperturbed flame, and the integral containing dA_0 is the area increment associated with extending or shortening the mean flame to intersect with the integration limit. The frequency domain equivalent for a two dimensional configuration in the different coordinate systems is:

$$\hat{A}'_{Axial}(\omega) = \underbrace{\left[\frac{1}{\beta^2}+1\right]^{1/2}\Delta\hat{x}}_{\substack{\text{Length fluctuation}\\ \text{of mean flame}}} + \underbrace{\left[1+\beta^2\right]^{-1/2}\int_0^{L_{0,A}}\frac{\partial\hat{\xi}'_A}{\partial x}dx}_{\substack{\text{Area fluctuation due to}\\ \text{wrinkling on mean flame}}} \tag{82}$$

$$\hat{A}'_{Transverse}(\omega) = \underbrace{\frac{\beta}{\sqrt{\beta^2+1}}\int_0^{L_{0,T}}\frac{\partial\hat{\xi}'_T}{\partial y}dy}_{\substack{\text{Area fluctuation due to}\\ \text{wrinkling on mean flame}}} \tag{83}$$

$$\hat{A}'_{Normal}(\omega) = \underbrace{\Delta\hat{s}}_{\substack{\text{Length fluctuation}\\ \text{of mean flame}}} \tag{84}$$

where $b = L_f/W$, and Δx and Δs are shown in Figure 1. Equations (82), (83), and (84) show that first order area fluctuations manifest themselves in three different ways in the different coordinate systems. In the axial coordinate system, first order area fluctuations occur over the length of the mean flame and in the oscillating integration limit. In the transverse coordinate system, there is no variation in integration limit; first order area fluctuations manifest entirely as wrinkles along the mean flame. In the normal coordinate system there is no variation in the mean flame position with downstream coordinate. That is, $\partial\xi_{N,0}/\partial s = 0$, eliminating leading order area fluctuation due to flame wrinkling; area fluctuations arise completely in the oscillating integration limit.

It seems intuitive that a global quantity such as flame area should be invariant of the coordinate system, **however**, the solution to these expressions are completely different, depending upon integration limits. For example, if the integration limits are assumed to be constants, and equal to a fixed axial distance, L_f (the flame height), transverse distance, W (flame width), or flame length, $\sqrt{L_f^2+W^2}$, then three different answers are obtained for G. To illustrate, consider the solution of eqn. (78) using these fixed integration limits for a two dimensional geometry, and the excitation of the flame by bulk axial forcing, a problem originally solved in the transverse coordinate system:

Fixed Axial Distance FTF:
$$G_{Axial} = -\frac{2}{St}\frac{1}{\left(\beta^2+1\right)}\sin\left(\frac{St}{2}\frac{\beta^2+1}{\beta^2}\right)e^{i\frac{St}{2}\frac{\beta^2+1}{\beta^2}} \tag{85}$$

Fixed width FTF:
$$G_{Transverse} = \frac{2}{St}\frac{\beta^2}{\left(\beta^2+1\right)}\sin\left(\frac{St}{2}\frac{\beta^2+1}{\beta^2}\right)e^{i\frac{St}{2}\frac{\beta^2+1}{\beta^2}} \tag{86}$$

Fixed length FTF:
$$G_{Normal} = 0 \tag{87}$$

where $St = \omega L_f / u_0$, ω is the angular forcing frequency, and u_0 is the mean axial velocity. Note that the transverse and axial FTF's differ by a factor of $(-b^2)$, while the fixed length FTF is identically zero for the normal coordinate system (the area contribution arising at higher order). For this reason, previous researchers have worked in a normal coordinate system when analyzing the local space time flame dynamics, but reverted to a transverse coordinate system for finding the flame area.

It is important to recognize that all of these solutions are correct within the approximations of the fixed integration limits; the fact that they are different arises from the fact that they are all solutions to different problems. For example, a problem where the transverse integration limit is fixed necessarily involves an oscillatory flame length in the other two integration limits, as shown in Figure 17.

Probably the most physically relevant problem for confined flame problems is the situation where the integration limit is transversely fixed. This represents a problem where an oscillatory flame spreads to the wall and the edge of the approach flow reactants, with an oscillatory flame height and length. In order to analyze this case in the normal or axial coordinate systems requires the solution of Eqn.(78) with a time varying integration limit. The time varying integration limit corrections for the axial and normal coordinate systems are determined by expanding the frequency domain fluctuating flame position functions to first order in a Taylor series and solving for the end correction using the geometric relations shown in Figure 1. These end corrections for the bulk forcing problem are given by:

$$\Delta\hat{x} = 2\frac{u'_{ref}}{\omega_0}\sin\left(\frac{St}{2}\frac{\beta^2+1}{\beta^2}\right)e^{i\frac{St}{2}\frac{\beta^2+1}{\beta^2}} \tag{88}$$

$$\Delta\hat{s} = 2\frac{u'_{ref}}{\omega_0}\frac{\beta}{\sqrt{1+\beta^2}}\sin\left(\frac{St}{2}\frac{\beta^2+1}{\beta}\right)e^{i\frac{St}{2}\frac{\beta^2+1}{\beta}} \tag{89}$$

Substituting Eqns. (88) and (89) respectively into Eqns. (82) and (84) yields the area fluctuations with the fixed width boundary condition. The flame transfer functions given by Eqn. (78) now become identical to the fixed width FTF expression shown in Eqn.(86) for all three coordinate systems, as must be the case.

5.0 Helical Mode Decomposition of a Transversely Forced, Swirl Stabilized Combustor

Another large part of the work done for this reporting period was focussed on the experimental investigation of a transversely forced, swirl stabilized combustor. The experimental data was previously acquired and the main intent of the work performed in this year was to process this data into a form from which meaningful conclusions could be drawn and to publish these conclusions. To that end a draft of a paper was submitted to The ASME Turbo Expo 2014: Turbine Technical Conference and Exposition and is currently undergoing peer review.

The experimental facility shown in

Figure 18 was designed to simulate acoustic fluctuations in annular combustion chambers with an "unwrapped" sector of an annular combustor with dimensions 1.14m **x** 0.10m **x** 0.34m. A rectangular window made of quartz, having dimensions of 0.2m x 0.09m is provided at the top of the combustor and provides optical access, while exhaust gases can pass through 0.08m diameter ports on either side of the optical window. Optical access to the flow field is through two large quartz windows, which have dimensions of 0.27m x 0.27m. The exit velocity, U_0, of this experimental setup is 25 m/s, corresponding to a Re=30,600. The flow can be excited using three 100 W speakers provided on each wall of the combustor. These speakers can be driven independently and can be driven so as to generate standing or traveling waves. If the speakers are driven at the same phase they are said to be "in-phase" or else they are said to be "out-of -phase". The data was acquired through the main optical access area using particle image velocimetry.

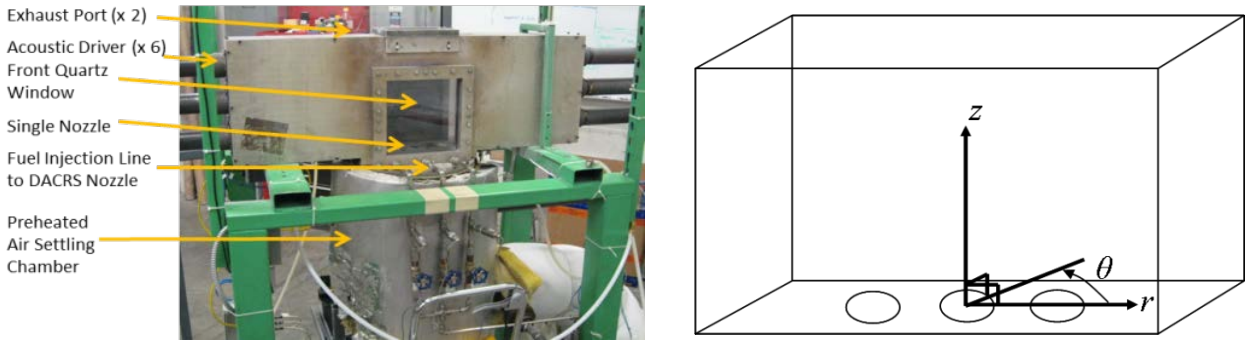

Figure 18 - Experimental setup of transverse forcing test facility (left) and polar coordinate system utilized overlaid on transverse forcing test facility

Data was acquired on each of two different measurement planes, in separate experiments. For measurements captured on the r-z plane, the sheet entered the combustor box through its top, passed along the z-axis (see
Figure 18), and its plane was parallel to the main window planes. For measurements on the r-θ plane, the laser sheet entered the combustor box through one of its main windows, and its plane was parallel to the dump plane. Experiments captured on the r-θ plane were repeated at five different axial positions (see Figure 19). Figure 19 also illustrates the time averaged, unforced flow field, where the colorized vector plot depicts the velocity field and the colorized contour plot illustrates the azimuthal vorticity field. Spatial coordinates are nondimensionalized by the nozzle exit diameter, *D*, and velocities are normalized by the nominal velocity, U_0 = 25 m/s.

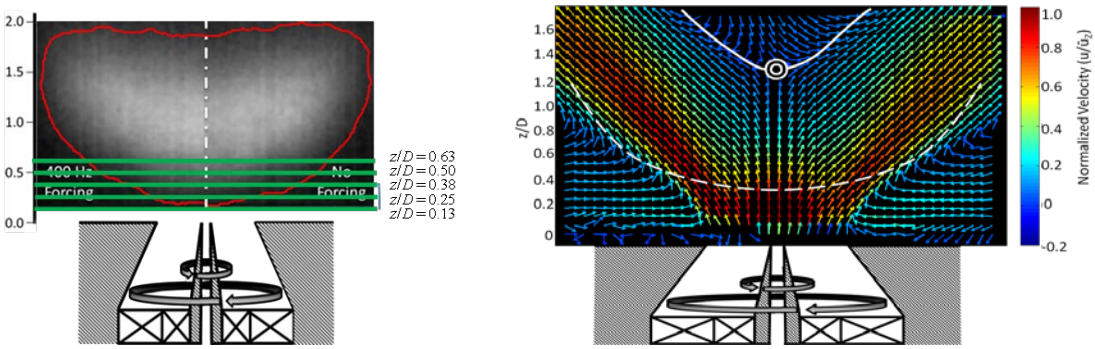

Figure 19 – Single nozzle configuration images of (left) line of sight, time averaged chemiluminescence images, showing the r-θ measurement planes and (right) time averaged velocity vectors measured on r-z measurement planes where solid white lines indicate zero axial velocity, the dashed line denotes the time averaged flame position, and the bullseye represents centerline axial stagnation point.

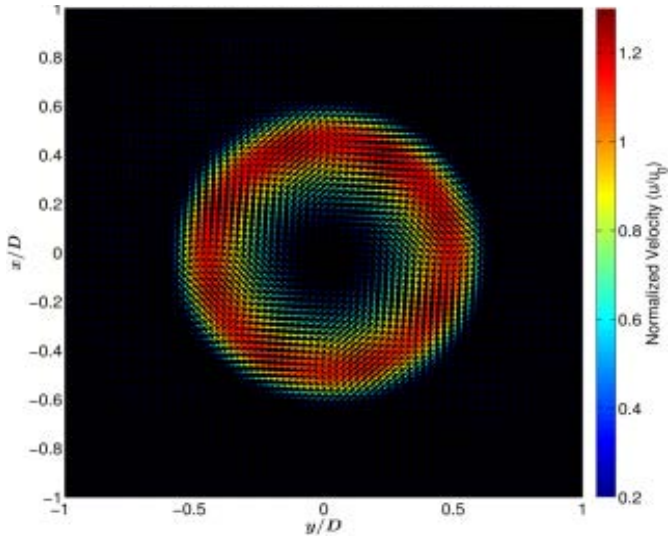

Figure 20 - Unforced velocity vector field measured on r-θ plane for single nozzle configuration at a representative, z/D of 0.13.

Figure 20 shows a typical time averaged avelocity field acquired on an *r-θ* measurement plane. Figure 21 shows the radial dependence of the azimuthal and radial velocities for the triple nozzle rig overlaid on those for the single nozzle rig. We can infer from Figure 21 that the time averaged flow field of the single nozzle setup is more axisymmetric than the corresponding Triple Nozzle flow field. This assertion is backed up by the plots in Figure 22 which show the plots of radial and azimuthal velocity in polar co-ordinates on *r-θ* planes. Also we can see from Figure 22 that the flow in the triple nozzle setup has a tendency to be squeezed between the walls and the neighboring nozzles.

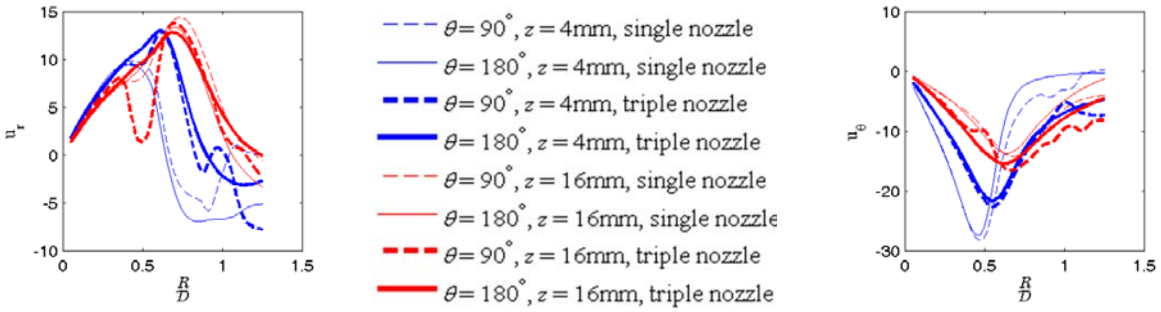

Figure 21 - Radial dependence of mean velocity showing $u_r(r)$ and $u_\theta(r)$.

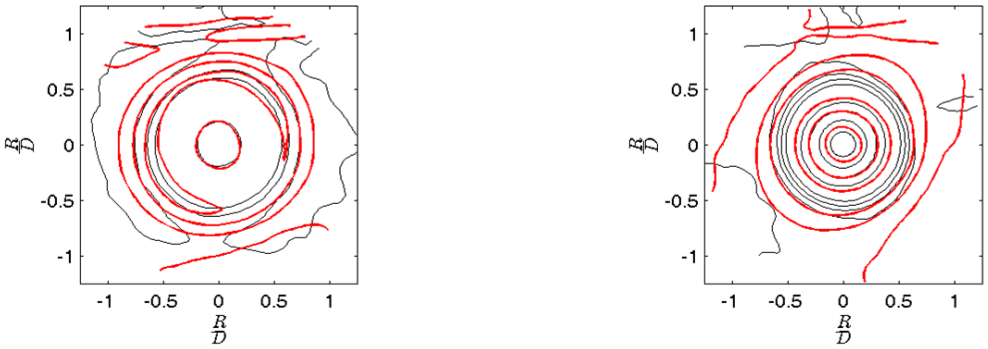

Figure 22 - Contours of $u_r(r,\theta)$ [left] and $u_\theta(r,\theta)$ [right]. Black lines indicate single nozzle, and red lines triple nozzle.

The instantaneous flow field exhibits a substantially more complicated structure than its time average, as shown by the sequence of images in Figure 23. The grayscale contours depict the magnitude of the axial velocity where the lighter contours indicate higher velocity. Velocity vectors with high axial velocity pointed downstream are colored black, and those with low or reversed axial velocity are colored white. In the figures, the bullseye marks the time averaged stagnation point (due to vortex breakdown), which is nominally about 1.3 diameters downstream of the dump plane. The star indicates the instantaneous stagnation point, which travels around the combustor and significantly varies its position from its time average. Visual inspection of a sequence of these images reveals some hints about the vortex breakdown bubble motion. For example, apparent movement of the stagnation point in and out of plane, coupled with its reappearance on the opposite side of the flow centerline, indicates precession of the recirculating flow region about the flow centerline. These images call attention to the complexity of the instantaneous flame and flow structure, and motivate the use of the helical mode decomposition to better understand the spatial and temporal flame/flow dynamics.

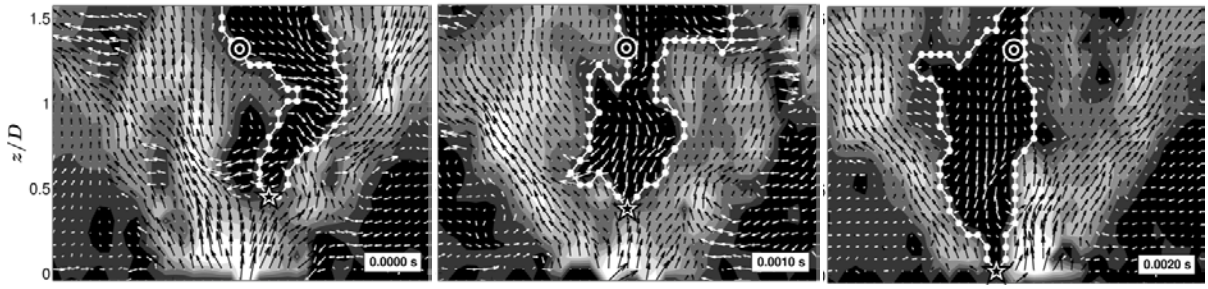

Figure 23 - Sequence of instantaneous velocity vector fields for unforced reacting flow. Dotted contour denotes line of zero axial velocity and star indicates leading velocity stagnation point. Bullseye indicates the time average stagnation point at the centerline

Another major part of the work done was on the helical mode decomposition (HMD) performed on the time resolved velocity fields. The helical mode decomposition is performed by first changing the velocity data from the Cartesian to the polar co-ordinate system and then obtaining the Fourier Transform of the fluctuating velocity components at each spatial location. The velocity components, after the transformation, are represented as:

$$\hat{u}_j'(r,\theta,z,\omega) = \sum_{m=-\infty}^{\infty} \hat{B}_{j,m}(r,z,\omega) e^{im\theta} \tag{90}$$

where $\hat{B}_{j,m}$ is referred to as the helical mode coefficient. The helical mode decomposition is performed by solving for the HMD coefficients, by numerically spatially integrating the velocity field according to:

$$\hat{B}_{j,m}(r,z,\omega) = \frac{1}{2\pi} \int_0^{2\pi} e^{-im\theta} \hat{u}_j'(r,\theta,z,\omega)\, d\theta \tag{91}$$

The HMD coefficients, $\hat{B}_{j,m}$, are representative of the spatial pattern of the azimuthal (j=r) or radial component of the fluctuating velocity (j=θ). The mode numbers denote the number of periods in the flow field. Figure 24 shows contours of $\mathrm{Re}\left\{\hat{B}_{\theta,1}(r, z = 12 \text{ mm}, 400 \text{ Hz}) \exp(i\theta)\right\}$, which is an instantaneous picture of the m=1 azimuthal velocity mode at a radial distance of 12mm and a forcing frequency of 400Hz.

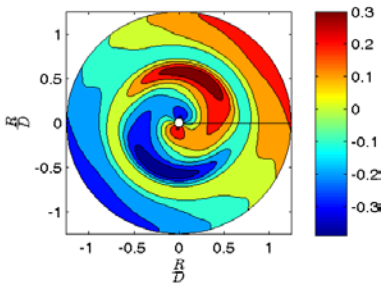

Figure 24 - Contour of m=1 azimuthal mode.

A repeatability analysis, shown in Figure 25, was performed using this dataset and an older one which was taken under mostly similar experimental conditions. The repeatability study performed shows good agreement between the old and new data especially qualitatively if not quantitatively.

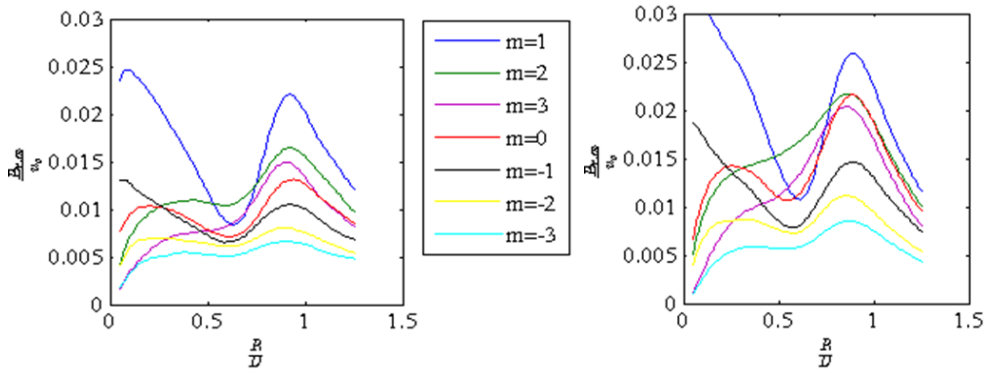

Figure 25 - Repeatability comparison of two datasets obtained under similar conditions.

We know that the helical mode coefficients are functions of frequency, radial position, axial position, mode number, and velocity component. For better analysis and comparison we try to reduce these dependencies as much as possible. One way of doing this is by measuring the magnitude only at the forcing frequency for forced cases. For unforced cases the energy is spread over a number of frequencies and the spectrum of this is plotted in Figure 26 which shows the ensemble averaged power spectrum for an unforced case.

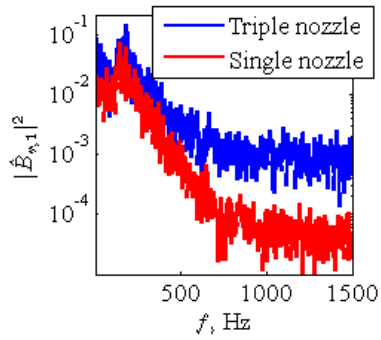

Figure 26 - Ensemble averaged power spectrum of unforced flow.

The radial dependence of the helical mode coefficients is removed by integrating the magnitude squared of the helical mode coefficients across the radial dimension:

$$C_{j,m} = \int_r \left| B_{j,m} \right|^2 rdr \tag{92}$$

These radially independent coefficients are the plotted along the axial direction and are shown in Figure 27.

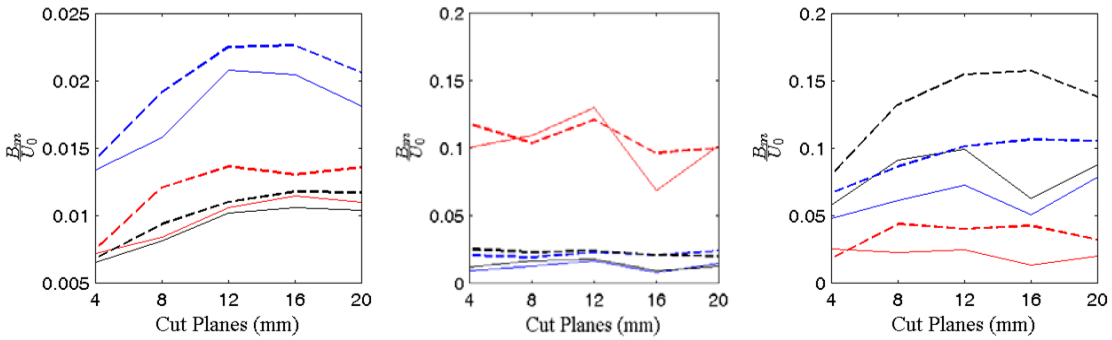

Figure 27 - Axial dependence of $\hat{B}_{r,m}$, integrated over radial position, for m=0, ±1.

There are two conclusions we can draw from these plots. First, the dominant mode in unforced, in-phase and out-of-phase forcing conditions are m=0, m=1 and m=-1 respectively. This shows that in-phase forcing elicits an axisymmetric response while out of phase forcing elicits a helical response. Second, the dominant mode and qualitative behavior of the modes with axial distance does not change with a switch from single to triple nozzle. Thus there is no key difference in the different modal energies from single to triple nozzle.
As discussed previously, a portion of work done for this period was the development of theoretical models to explain the behaviour of the flow fields obtained from the experimental data described above. From the experimental data obtained it was observed that the behaviour of the stagnation point varied drastically between the instantaneous and the time-averaged flow field. An assumption was made that the stagnation point dynamics get washed out by simple averaging and thus the picture presented by the time-averaged image could be misleading in some cases. Thus a theoretical model was developed to quantitatively explain this behaviour.

To allow comparison with experimental data, we calculate the probability that the flow is negative. This comparison is independent of magnitude of positive vs. reverse flow velocity magnitude. The switch from negative to positive marks the boundary of the Vortex Breakdown Bubble. We binarize the instantaneous velocity field based on positive/negative velocity and compute average binarized field which is shown below.

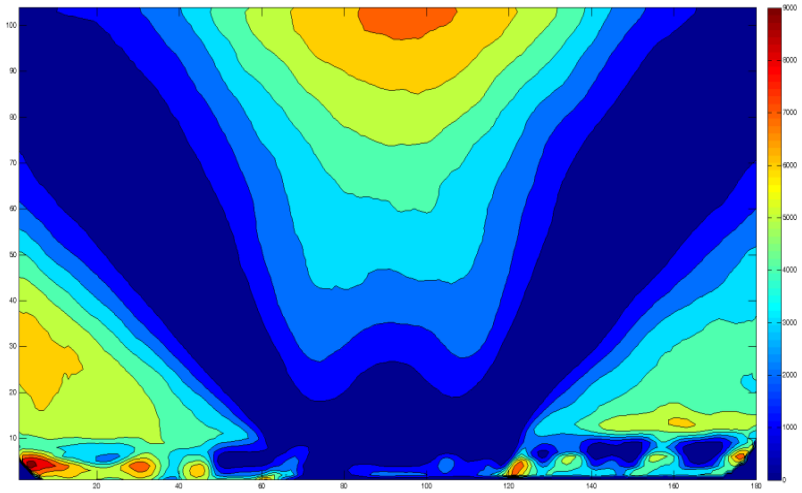

Figure 28 – Experimental average binarized positive/negative velocity field.

From this result we see that the closest geometric shape to the vortex breakdown bubble is a paraboloid. Thus we have decided to theoretically model this problem based on the assumption that the VBB is a paraboloid. We describe the procedure undertaken in this effort below.

We use Cartesian coordinates: +x is up, +y is right, and +z into plane. We will model the U_x=0 contour ie., the vortex breakdown bubble boundary as a parabola of revolution, with its vertex precessing around geometric center axis at a radius R, with an angular frequency ω_0.

We start with the equation for a parabola of revolution with its vertex at (x=Cnst.,a,b) in an x=Cnst. plane in 3D space:

$$\frac{x}{R_1} = \frac{2(y-b)}{R_2} + \frac{2(z-c)}{R_3} \tag{93}$$

We then simulate precession by varying the vertex in time sinusoidally by setting b=R*sin(ω_0t) and c=R*cos(ω_0t). Now we interrogate along the x-y plane by setting z=0. This simulates planar PIV measurements.

In order to more closely match the experimental results velocity biasing was added to each time instant in which the velocity at all points inside the simulated VBB was assumed to have a constant reverse flow velocity u_{rev} and all points outside the simulated VBB were assumed to have a constant forward mean flow velocity u_{mean} and these instantaneous flow fields were then time averaged to give the progress variable field.

The projection of the paraboloid on the x-y plane is calculated at each time instant by looping through the time vector. Then a loop runs through the grid running through the vertical axis first then stepping along the horizontal axis. At each grid point it is determined if the point is within or without the projection of the paraboloid. If the point is inside the projection ie., inside the VBB then the assumed negative/reverse velocity is assigned to that point. Else the forward flow velocity is assigned to it. These instantaneous snapshots are then averaged over the whole time period to get the time averaged progress variable field. From this model using he method detailed above we obtain the progress variable field as shown below where probability of reverse flow ranges from 0-1.

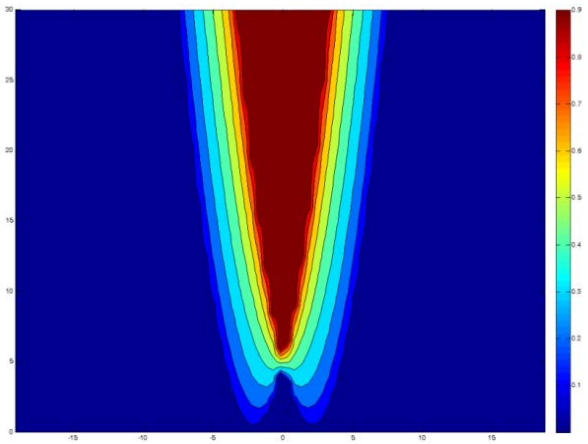

Figure 29 – Theoretically calculated progress variable field with simple simulated dynamics.

This result looks similar to the experimental result but to even more closely match the experimental data, the simple model was made more complex by adding periodic motion in the horizontal and vertical directions to further improve the accuracy of the model.

In order to add noise to the motion in the longitudinal direction the radius of precession ‘r’ was divided into a mean component R and a fluctuating component r’=Ksin(sin(ω0t)) where K is constant. Thus the total time dependant radius of precession becomes r=R+r’. The top view of the paraboloid showing the time variant motion in the y-z plane is shown below.

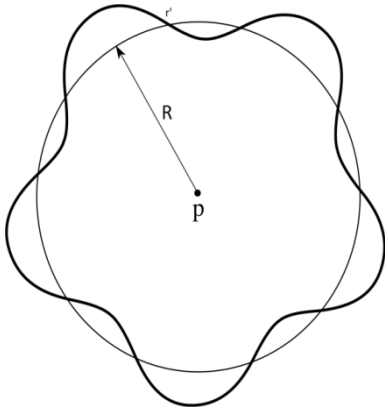

Figure 30 – Diagram of paraboloid showing the time variant motion in the y-z plane.

The progress variable field is obtained as before and is shown below. As we can see, this is closer to the experimentally obtained field than our original model.

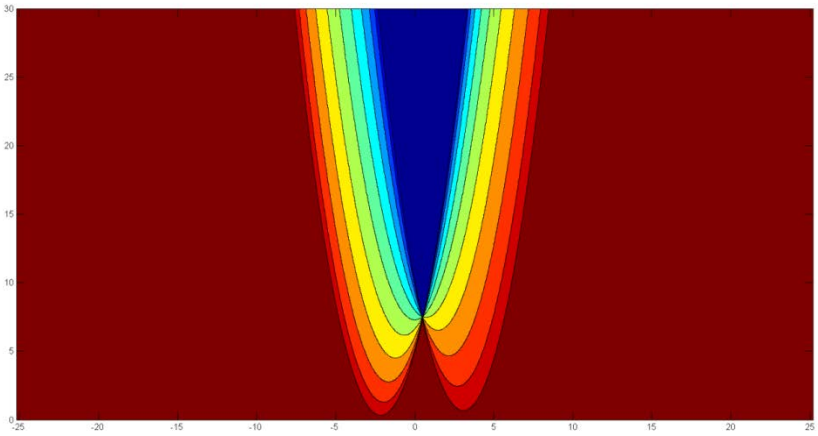

Figure 31 - Theoretically calculated progress variable field with advanced simulated dynamics including radial fluctuations.

In order to further investigate the effects of noise we assumed that the paraboloid is moving up and down on the vertical (x) axis sinusoidally as it is revolving about the same axis. Thus the equation for the projection becomes:

$$\frac{\left(x - a\sin\left[\omega_0 t\right]\right)}{R_1} = \frac{2\left(y-b\right)}{R_2} + \frac{2\left(z-c\right)}{R_3} \tag{94}$$

where b and c are the same constants as before and aSin(ω_0t) represents the time variant fluctuation in the vertical direction. The results of simulation with both types of noise added in is shown below.

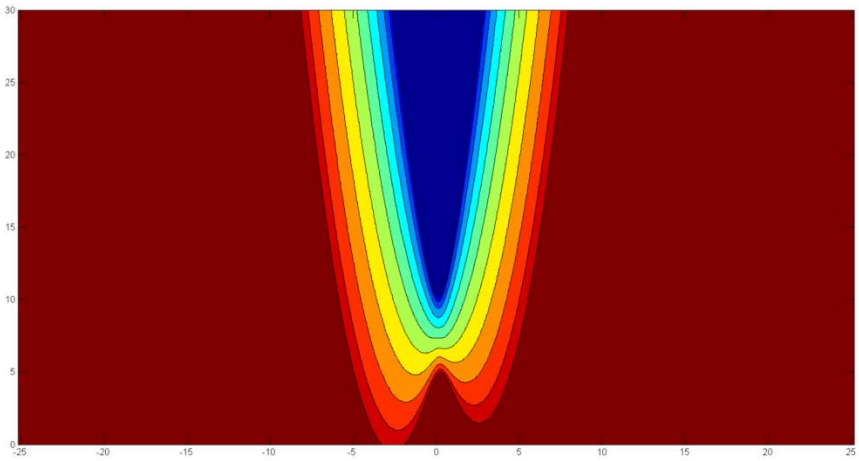

Figure 32 - Theoretically calculated progress variable field with advanced simulated dynamics including radial and axial fluctuations.

6.0 RESPONSE OF AZIMUTHAL FLOW FLUCTUATIONS IN THE ANNULAR NOZZLE OF A SWIRLER

Both axial vortical disturbances, and not only the familiar azimuthal vortical disturbances associated with vortex roll-up of the shear layers, have significant influences on the flame response. However, there is a fundamental difference between axial and azimuthal vorticity disturbances in terms of the flow oscillations they induce on the flame.

In order to better understand this, consider the disturbance pathways shown in Figure 33, which show how an acoustic disturbance leads to heat release oscillations. The familiar azimuthal vortical disturbances due to vortex roll-up are shown in pathway (2a). These then cause axial and radial flow fluctuations in the combustor via pathway (2b). The presence of the swirler causes axial vorticity fluctuations (path 1a) which then induce azimuthal flow fluctuations (path 1b) *only*. These azimuthal flow fluctuations indirectly excite axial and radial velocity fluctuations, due to bending/rotation of the axial vortex tube (1c). For example, the oscillatory azimuthal flow in the injector nozzle induces an oscillatory radial flow component at the rapid expansion point where the swirling nozzle flow enters the combustor. This differentiation between azimuthal flow disturbances on one hand, and radial/axial disturbances on the other, is significant because the flame itself is disturbed only by the velocity component normal to it (3a). This implies that axisymmetric mean flames are not directly affected by azimuthal flow fluctuations, since they are tangential to it. Thus, it is the indirect azimuthal to radial/axial mechanism (1c) that controls the strength of the flow oscillations normal to the flame that lead to heat release oscillations in axisymmetric flames, as indicated by pathways (1a-1b-1c-3a), which is boxed in red in the figure under the heading of "I". This coupling process is not easily amenable to analytical calculations and, as such, we report here a computational study of the role of these different flow fluctuations on the flame response in an axisymmetric framework.

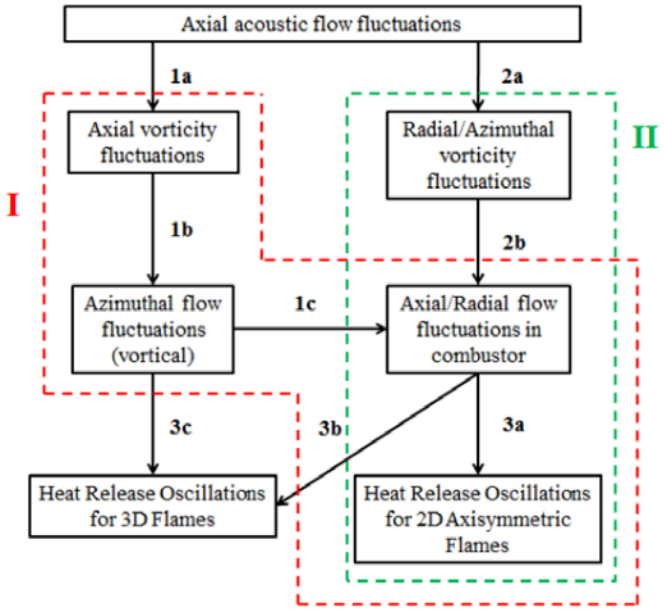

Figure 33 – Disturbance pathways leading to heat release oscillations.

The model combustor configuration used in this work is shown in Figure 34. It consists of an annular flow passage with a 45 degree, 8 vane swirler, connected to a larger combustor. The dimensions of this geometry are detailed in Table 1.

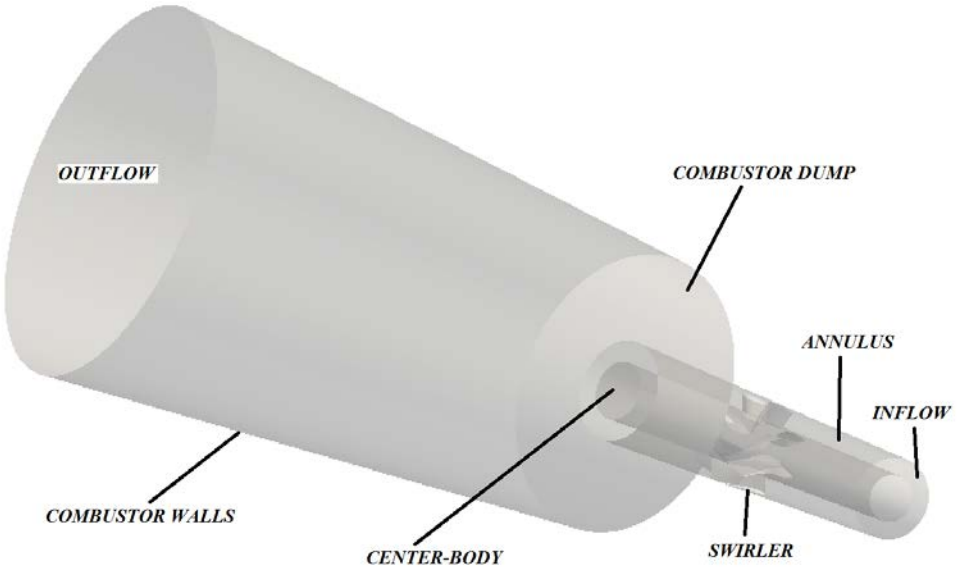

Figure 34 – Schematic of complete model combustor.

Table 1 – Dimensions of the model combustor shown in Figure 34.

Detail	Dimension
Outer diameter of nozzle	*D*
Inner diameter of nozzle	0.57 *D*
Outer diameter of combustor dump	2.75 *D*
Combustor Length	11.0 *D*
Swirler location upstream of dump	2.84 *D*
Length of nozzle	6.25 *D*

An unsteady RANS approach was used, implemented with the C++ toolbox OpenFOAM (Open-Field-Operations-and-Manipulations). This toolbox is an open-source collection of finite volume solvers and numerical methods tailored for CFD simulations. The non-reacting steady state flow fields are computed using the simpleFoam solver which uses the SIMPLE pressure-coupling method in an incompressible framework. The forced unsteady simulations are performed using the pisoFoam solver which uses the PISO method for pressure-velocity coupling. For the flow forcing at the inlet, the “inlet velocity modulation” (IVM) technique is adopted. An SSG (Speziale-Sarkar-Gatski) closure model is used for turbulence closure. A second order backward

Euler scheme was used with a time-step that is 1/100th the time-period of acoustic forcing. The simulations were run for a total of 1000 time-steps, corresponding to 10 acoustic time-periods. The spatial discretization is performed using a second order scheme. The Reynolds number for the flow, defined as $\mathrm{Re} = U_0 D/\nu$ is 87,000.

In order to understand the generation of azimuthal flow fluctuations at the swirler, we consider simulations of the non-reacting flow in the swirler-annulus section only for the geometry shown in Figure 34. The swirler annulus simulation was performed for an inlet axial velocity of 30 m/s. The swirler-annulus geometry is solved for a single blade passage, with rotational periodic boundary conditions. It is meshed into 1 million body-fitted hexagonal volume elements.

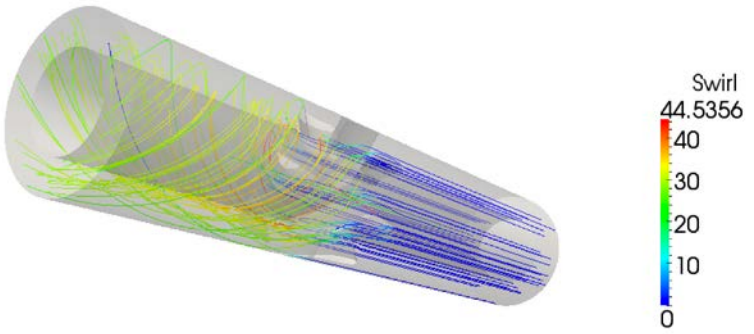

Figure 35 – Instantaneous streamline pattern in the Swirler-Annulus section of the combustor.

Typical streamlines are shown in Figure 35. The streamlines are colored by the swirl component of velocity. This figure clearly shows the change in flow direction across the swirler. The downstream evolution of the mean axial and tangential flow components are shown in Figure 36. Note that the flow is uniform upstream of the swirler and accelerates as the flow traverses the swirler vanes. This is due to the volume constriction created by the swirler vanes within the annulus cross-section. Since the swirler has 8 vanes, the immediate downstream region of the swirler is spatially periodic. However, this profile becomes uniform downstream, as indicated in the figure.

Next, consider the flow dynamics in the swirler annulus section when the axial flow at the inlet is forced. The axial forcing was performed with amplitude of 10% at frequencies 250Hz, 300Hz, 350Hz and 400Hz. The time-series of the axial and azimuthal flow at different locations downstream of the swirler is shown in Figure 37, for the 250Hz forcing case. Note that there is negligible phase difference across the different locations for the axial component, as shown in Figure 37(a). This is an artifact of incompressible simulations where the speed of the wave is infinite. However, notice the axial dependence of the azimuthal flow phase, as shown in Figure 37(b). The axial phase variation is shown in

Figure 37(c) from which an axial phase speed is extracted. Note that the mean axial flow velocity from this phase speed corresponds to that measured at the mid-annular location of $r = 0.39D$. Due to the acceleration of the flow in the annulus past the swirler, this velocity (~40 m/s) is higher than the uniform velocity (30 m/s) imposed at the upstream inlet. This plots clearly indicates how the swirler converts the axial, incompressible disturbance, into an azimuthal, convecting (vortical) flow disturbance.

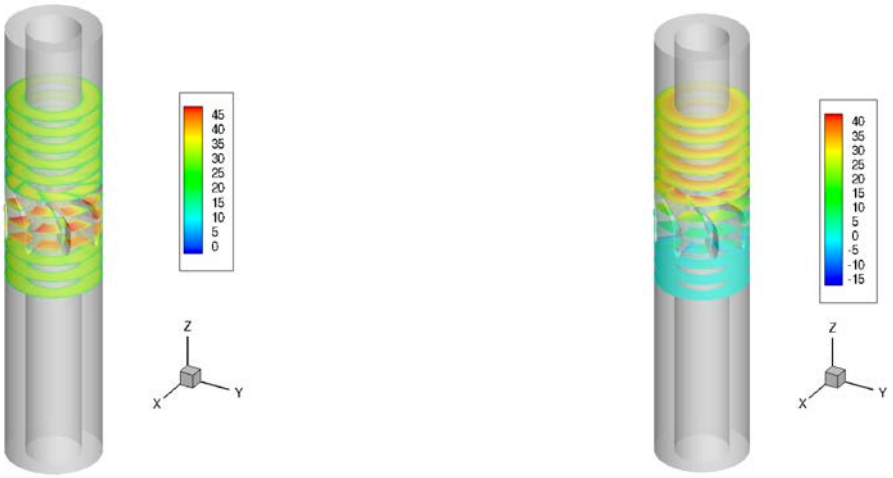

(a) **(b)**

Figure 36 – Downstream evolution of the (a) mean axial velocity and (b) mean azimuthal velocity, shown in transverse cut-planes perpendicular to the axial direction. The inlet axial mean flow is 30 m/s (from the bottom).

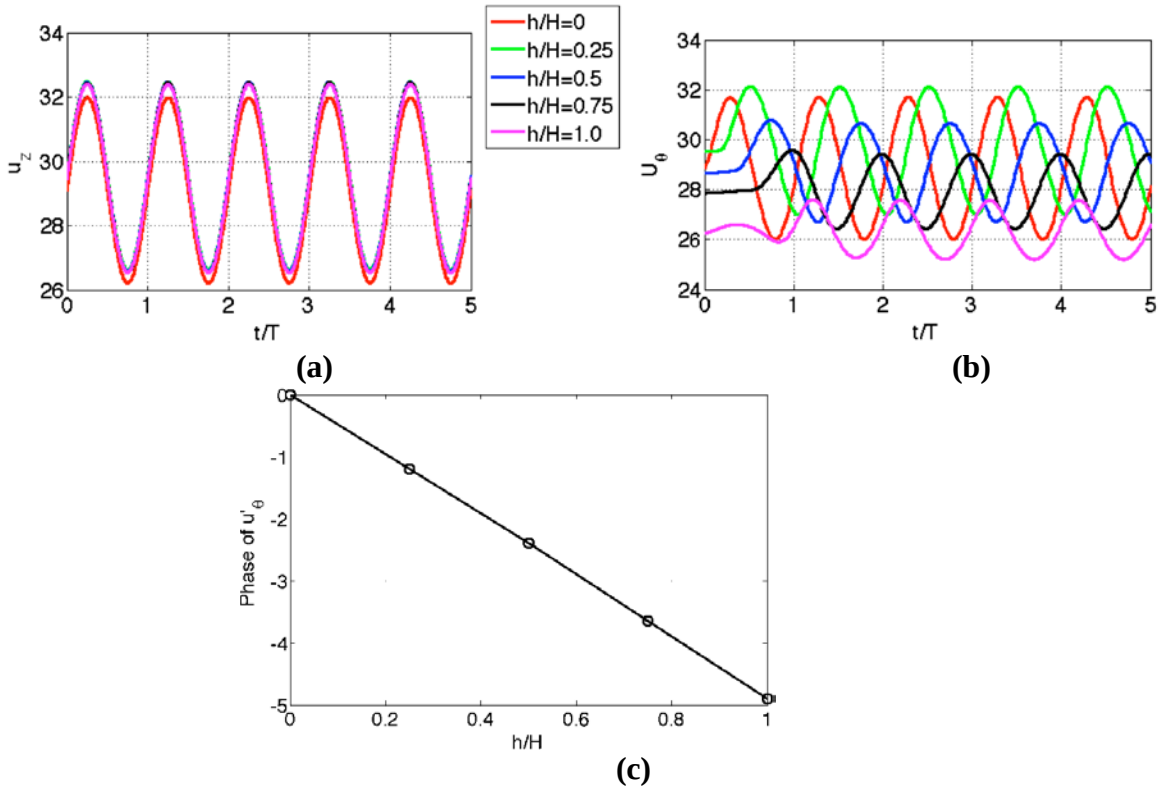

(a) **(b)**

(c)

Figure 37 – Time-series evolution of the mid-annular (r = 0.39D) (a) axial flow and (b) azimuthal flow components at different axial locations downstream of the swirler for the 250Hz forcing case. (c) Spatial phase variation of the azimuthal flow velocity fluctuation. H is the axial length of the annular section downstream of the swirler (= 2.84D), h is the location downstream of the swirler where the time-series is shown.

The differences in wave propagation speed of the axial and azimuthal components also imply that their relative phase difference evolves axially. In fact, these components of the flow fluctuations are not in phase at the exit of the swirler. This phase difference at the swirler exit is a function of the forcing frequency, as shown in Figure 38. The relative phase exhibits a monotonically increasing trend (roughly linear) with an increase in forcing frequency. This relative phasing is a very important parameter for the *FTF*.

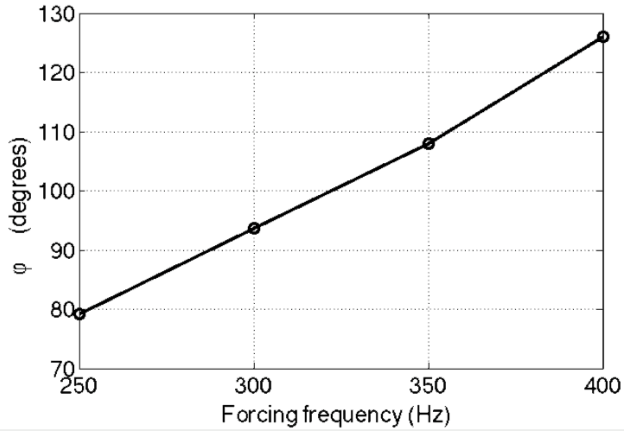

Figure 38 – Variation of relative phase between the axial and azimuthal flow fluctuations, with forcing frequency, at the exit of the swirler.

7.0 Conclusions

The work done on this project has yielded some important and significant results regarding the dynamics of harmonically forced premixed flames. A key finding from this work was that helical modes influence the FTF of axisymmetric and non-axisymmetric mean flames differently. In the case of axisymmetric mean flames, only the axisymmetric contribution of the flame wrinkling behavior contributes to the global fluctuating area. This stems from the simple mathematical fact that non-axisymmetric modes in the fluctuating flame response lead to area cancellation due to the 2π periodicity of these modes. Hence, only the axisymmetric, m=0 mode in the fluctuating flow field contributes to changes in global flame area. This implies that even if the dominant wrinkling flame response mode is non-axisymmetric, it does not contribute to the global unsteady heat release of axisymmetric flames. Thus significantly different sensitivities may be observed in single and multi-nozzle flames in otherwise identical hardware, due to the near axisymmetry in one case and the strong non-axisymmetry in the other.

In order to answer this question, analytical results were derived for weak asymmetries and a numerical solver was used to strong asymmetries in the mean flame/flow. Two example cases were considered: (i) Elliptic cross-section and (ii) Square cross-section. In both these cases, results showed that for a linear analysis, the asymmetry modes in the mean flame/flow interact with the same but opposite modes in the flow disturbance to lead to a finite global flame response. This effect is compounded especially when non-compact flames are considered, wherein, the global

unsteady heat release is not considered. In this case, the Rayleigh criterion requires the local unsteady heat release to be multiplied with the local unsteady pressure before the Rayleigh Index is calculated.

In addition, the slope of the regression line between consumption and displacement speed was determined, which allows us to relate the turbulent displacement speed directly to the consumption speed. This allows us to determine the computational, ensemble averaged heat release, which locally is given by Eqn.(71). This may then be extended to determine a computational flame transfer function! Also, the differences in the transfer functions derived from different coordinate systems was reconciled. It was determined that a correction factor was necessary to account for the fact that the flame tip moves periodically. In systems where the flame position function is not oriented parallel to the wall, this flame movement causes the limit of integration to change when determining the spatially integrated heat release. Whereas, in systems with the flame position function oriented parallel to the wall, and normal to the direction of integration, integration to the wall accounts for flame tip fluctuations. One key result is the significance of the integration limit when evaluating global FTF's – very different answers are obtained for different assumptions on the integration surface. It is important to recognize that all of these solutions are correct within the approximations of the fixed integration limits; the fact that they are different arises from the fact that they are all solutions to different problems.

Regarding the dynamics of harmonically forced premixed flames and their vortex breakdown bubble flow dynamics, a theoretical model was proposed to explain the interesting behavior and difference between the instantaneous and time averaged stagnation point behavior. The vortex breakdown bubble was modelled as a parabola of revolution, with its vertex precessing around geometric center axis at a radius R, with an angular frequency ω_0. In order to more closely match the experimental results velocity biasing was added to each time instant in which the velocity at all points inside the simulated VBB was assumed to have a constant reverse flow velocity urev and all points outside the simulated VBB were assumed to have a constant forward mean flow velocity umean and these instantaneous flow fields were then time averaged to give the progress variable field. Additional axial and azimuthal oscillations were added for increased comparison.

Lastly, our work presented velocity field measurements and analysis for a transversely forced, swirl stabilized combustor. The analysis compared single nozzle and multi-nozzle configurations. Previous studies of multiple jet flows indicate that neighboring jets experience a mutual interaction, upstream of the direct shear layer interaction, which can alter both the time averaged and dynamical flowfields. Therefore, this experimental study has probed the velocity field near the dump plane to see if such mutual interactions exist. Results show minor differences in the time averaged flows when switching from single nozzle to multi-nozzle flows. The most notable difference is a non-axisymmetric elongation of the jet cross section. The major axis of the elongation "tilts" to align itself away from the nearby combustor walls and nozzles. The direction of this tilting appears to be prescribed by the swirl direction of the neighboring nozzles.

8.0 REFERENCES

1] Syred, N., *A Review of Oscillation Mechanisms and the Role of the Precessing Vortex Core (Pvc) in Swirl Combustion Systems.* Progress in Energy and Combustion Science, 2006. **32**(2): p. 93-161.

[2] Cala, C.E., Fernandes, E.C., Heitor, M.V., and S.I., S., *Coherent Structures in Unsteady Swirling Jet Flow.* Experiments in Fluids, 2006. **40**(2): p. 267-276.

[3] Jochmann, P., Sinigersky, A., Hehle, M., Schafer, O., Koch, R., and Bauer, H.J., *Numerical Simulation of a Precessing Vortex Breakdown.* International Journal of Heat and Fluid Flow, 2006. **27**(2): p. 192-203.

[4] Fick, W., Griffiths, A.J., and O'Doherty, T., *Visualisation of the Precessing Vortex Core in an Unconfined Swirling Flow.* Optical Diagnostics in Engineering, 1997. **2**(1): p. 19-31.

[5] Shtork, S.I., Vieira, N.F., and Fernandes, E.C., *On the Identification of Helical Instabilities in a Reacting Swirling Flow.* Fuel, 2008. **87**(10-11): p. 2314-2321.

[6] Wang, S. and Rusak, Z., *The Dynamics of a Swirling Flow in a Pipe and Transition to Axisymmetric Vortex Breakdown.* Journal of Fluid Mechanics, 1997. **340**: p. 177-223.

[7] Lucca-Negro, O. and O'Doherty, T., *Vortex Breakdown: A Review.* Progress in Energy and Combustion Science, 2001. **27**(4): p. 431-481.

[8] Serre, E. and Bontoux, P., *Vortex Breakdown in a Three-Dimensional Swirling Flow.* Journal of Fluid Mechanics, 2002. **459**: p. 347-370.

[9] Lacarelle, A., Faustmann, T., Greenblatt, D., Paschereit, C. O., Lehmann, O., Luchtenburg, D. M., and Noack, B. R., *Spatiotemporal Characterization of a Conical Swirler Flow Field under Strong Forcing.* Journal of Engineering for Gas Turbines and Power, 2009. **131**: p. 031504.

[10] O'Connor, J. and Lieuwen, T., *Recirculation Zone Dynamics of a Transversely Excited Swirl Flow and Flame* Physics of Fluids, 2012. **24**(7): p. 075107.

[11] Dawson, J., Rodriguez-Martinez, V., Syred, N., and O'Doherty, T., *The Effect of Combustion Instability on Recirculation Zones in a Swirl Burner/Furnace* in *42nd AIAA Aerospace Sciences Meeting and Exhibit*2004: Reno, NV, USA.

[12] Kariuki, J. and Dawson, J., *Measurements in Turbulent Premixed Bluff Body Flames Close to Blow-Off.* Combustion and Flame, 2012. **159**(8): p. 2589-2607.

[13] Lieuwen, T., McDonell, V., Santavicca, D.A., and Sattelmayer, T., *Burner Development and Operability Issues Associated with Steady Flowing Syngas Fired Combustors.* Combustion Science and Technology, 2008. **180**(6): p. 1169-1192.

[14] Balachandran, R., Ayoola, B., Kaminski, C., Dowling, A., and Mastorakos, E., *Experimental Investigation of the Nonlinear Response of Turbulent Premixed Flames to Imposed Inlet Velocity Oscillations.* Combustion and Flame, 2005. **143**(1-2): p. 37-55.

[15] Armitage, C., Balachandran, R., Mastorakos, E., and Cant, R., *Investigation of the Nonlinear Response of Turbulent Premixed Flames to Imposed Inlet Velocity Oscillations.* Combustion and Flame, 2006. **146**(3): p. 419-436.

[16] Ducruix, S., Schuller, T., Durox, D., and Candel, S., *Combustion Dynamics and Instabilities: Elementary Coupling and Driving Mechanisms.* J. Propul. Power, 2003. **19**(5): p. 722-734.

[17] Dowling, A., *A Kinematic Model of a Ducted Flame.* Journal of Fluid Mechanics, 1999. **394**(-1): p. 51-72.

[18] Schuller, T., Durox, D., and Candel, S., *A Unified Model for the Prediction of Laminar Flame Transfer Functions Comparisons between Conical and V-Flame Dynamics.* Combust. Flame, 2003. **134**(1-2): p. 21-34.

[19] Preetham, Santosh, H., and Lieuwen, T., *Dynamics of Laminar Premixed Flames Forced by Harmonic Velocity Disturbances.* J. Propul. Power, 2008. **24**(6): p. 1390-1402.

[20] Palies, P., Schuller, T., Durox, D., and Candel, S., *Modeling of Premixed Swirling Flames Transfer Functions.* Proceedings of the Combustion Institute, 2011. **33**(2): p. 2967-2974.
[21] Fanaca, D., Alemela, P.R., Hirsch, C., and Sattelmayer, T., *Comparison of the Flow Field of a Swirl Stabilized Premixed Burner in an Annular and a Single Burner Combustion Chamber.* Journal of Engineering for Gas Turbines and Power, 2010. **132**(7): p. 071502.
[22] Komarek, T. and Polifke, W., *Impact of Swirl Fluctuations on the Flame Response of a Perfectly Premixed Swirl Burner.* Journal of Engineering for Gas Turbines and Power, 2010. **132**(6): p. 061503-1-061503-7.
[23] Garcia-Villalba, M., Frohlich, J., and Rodi, W., *Large Eddy Simulation of an Annular Swirling Jet with Pulsating Inflow*. in *Turbulence and Shear Flow Phenomena*. 2005. Williamsburg, VA.
[24] Straub, D. and Richards, G., *Effect of Axial Swirl Vane Location on Combustion Dynamics*, in *ASME Turbo Expo*1999: Indianpolis, IN.
[25] Dowling, A. and Stow, S., *Acoustic Analysis of Gas-Turbine Combustors*, in *Combustion Instabilities in Gas-Turbine Engines: Operational Experience, Fundamental Mechanisms and Modeling*, Lieuwen, T. and Yang, V., Editors. 2005, AIAA. p. 369-414.
[26] Acharya, V., Shreekrishna, Shin, D.H., and Lieuwen, T., *Swirl Effects on Harmonically Excited, Premixed Flame Kinematics.* Combustion and flame, 2012. **159**: p. 1139-1150.
[27] Huang, Y. and Yang, V., *Effect of Swirl on Combustion Dynamics in a Lean-Premixed Swirl-Stabilized Combustor.* Proceedings of the Combustion Institute, 2005. **30**(2): p. 1775-1782.
[28] Michalke, A. and Hermann, G., *On the Inviscid Instability of a Circular Jet with External Flow.* Journal of Fluid Mechanics, 1982. **114**: p. 343-359.
[29] Liepmann, D. and Gharib, M., *The Role of Streamwise Vorticity in the near-Field Entrainment of Round Jets.* Journal of Fluid Mechanics, 1992. **245**: p. 643-668.
[30] Yule, A., *Large-Scale Structure in the Mixing Layer of a Round Jet.* Journal of Fluid Mechanics, 1978. **89**(03): p. 413-432.
[31] Pier, B., *Local and Global Instabilities in the Wake of a Sphere.* Journal of Fluid Mechanics, 2008. **603**: p. 39-61.
[32] Monkewitz, P., *A Note on Vortex Shedding from Axisymmetric Bluff Bodies.* Journal of Fluid Mechanics, 1988. **192**: p. 561-575.
[33] Loiseleux, T., Chomaz, J., and Huerre, P., *The Effect of Swirl on Jets and Wakes: Linear Instability of the Rankine Vortex with Axial Flow.* Physics of Fluids, 1998. **10**: p. 1120.
[34] Rayleigh, J.S.W., *The Theory of Sound*. Vol. 2. 1894, London: McMillan.
[35] Paschereit, C.O., Gutmark, E., and Weisenstein, W., *Excitation of Thermoacoustic Instabilities by Interaction of Acoustics and Unstable Swirling Flow.* AIAA Journal, 2000. **38**(6): p. 1025-1034.
[36] Steinberg, A.M., Boxx, I., Stohr, M., Carter, C.D., and Meier, W., *Flow–Flame Interactions Causing Acoustically Coupled Heat Release Fluctuations in a Thermo-Acoustically Unstable Gas Turbine Model Combustor.* Combustion and Flame, 2010. **157**(12): p. 2250-2266.
[37] Stohr, M., Boxx, I., Carter, C.D., and Meier, W., *Experimental Study of Vortex-Flame Interaction in a Gas Turbine Model Combustor.* Combustion and Flame, 2012. **159**(8): p. 2636-2469.
[38] Moeck, J.P., Bourgouin, J.-F., Durox, D., Schuller, T., and Candel, S., *Nonlinear Interaction between a Precessing Vortex Core and Acoustic Oscillations in a Turbulent Swirling Flame.* Combustion and Flame, 2012. **159**(8): p. 2650-2668.
[39] O'Connor, J. and Lieuwen, T., *Disturbance Field Characteristics of a Transversely Excited Burner.* Combustion Science and Technology, 2011. **183**(5): p. 427-443.

[40] Bellows, B., Bobba, M., Forte, A., Seitzman, J., and Lieuwen, T., *Flame Transfer Function Saturation Mechanisms in a Swirl-Stabilized Combustor.* Proceedings of the Combustion Institute, 2007. **31**(2): p. 3181-3188.
[41] Thumuluru, S.K. and Lieuwen, T., *Characterization of Acoustically Forced Swirl Flame Dynamics.* Proceedings of the Combustion Institute, 2009. **32**(2): p. 2893-2900.
[42] Bellows, B., Neumeier, Y., and Lieuwen, T., *Forced Response of a Swirling, Premixed Flame to Flow Disturbances.* J. Propul. Power, 2006. **22**(5): p. 1075.
[43] Worth, N. and Dawson, J., *Self-Excited Circumferential Instabilities in a Model Annular Gas Turbine Combustor: Global Flame Dynamics.* Proceedings of the Combustion Institute, 2013. **34**: p. In Press.
[44] Samarasinghe, J., Peluso, S., Szedlmayer, M., DeRosa, A., Quay, B., and Santavicca, D., *3-D Chemiluminescence Imaging of Unforced and Forced Swirl-Stabilized Flames in a Lean Premixed Multi-Nozzle Can Combustor*. in *ASME Turbo Expo*. 2013. San Antonio, TX, USA: ASME.
[45] Worth, N. and Dawson, J., *Self-Excited Circumferential Instabilities in a Model Annular Gas Turbine Combustor: Global Flame Dynamics.* Proceedings of the Combustion Institute, 2013. **34**(2): p. 3127-3134.
[46] Fleifil, M., Annaswamy, A.M., Ghoneim, Z.A., and Ghoniem, A.F., *Response of a Laminar Premixed Flame to Flow Oscillations: A Kinematic Model and Thermoacoustic Instability Results.* Combustion and Flame, 1996. **106**(4): p. 487-510.
[47] Markstein, G.H., *Nonsteady Flame Propagation*1964: Pergamon.
[48] Matalon, M. and Matkowsky, B., *Flames as Gasdynamic Discontinuities.* Journal of Fluid Mechanics, 2006. **124**: p. 239-259.
[49] Boyer, L. and Quinard, J., *On the Dynamics of Anchored Flames.* Combustion and Flame, 1990. **82**(1): p. 51-65.
[50] Williams, F., *Turbulent Combustion.* the Mathematics of combustion, 1985: p. 97-131.
[51] Lee, D.H. and Lieuwen, T.C., *Premixed Flame Kinematics in a Longitudinal Acoustic Field.* Journal of Propulsion and Power, 2003. **19**(5): p. 837-846.
[52] Kuramoto, Y. and Tsuzuki, T., *Persistent Propagation of Concentration Waves in Dissipative Media Far from Thermal Equilibrium.* Prog. Theor. Phys, 1976. **55**(2): p. 356-369.
[53] Sivashinsky, G.I., *Nonlinear Analysis of Hydrodynamic Instability in Laminar Flames—I. Derivation of Basic Equations.* Acta Astronautica, 1977. **4**(11–12): p. 1177-1206.
[54] Matalon, M. and Matkowsky, B.J., *Flames as Gas-Dynamic Discontinuities.* Journal of Fluid Mechanics, 1982. **124**(Nov): p. 239-259.
[55] Creta, F., Fogla, N., and Matalon, M., *Turbulent Propagation of Premixed Flames in the Presence of Darrieus-Landau Instability.* Combustion Theory and Modelling, 2011. **15**(2): p. 267-298.
[56] Searby, G. and Rochwerger, D., *A Parametric Acoustic Instability in Premixed Flames.* Journal of Fluid Mechanics, 1991. **231**: p. 529-543.
[57] Preetham, Thumuluru, S.K., Santosh, H., and Lieuwen, T., *Linear Response of Laminar Premixed Flames to Flow Oscillations: Unsteady Stretch Effects.* Journal of Propulsion and Power, 2010. **26**(3): p. 524-532.
[58] Wang, H.Y., Law, C.K., and Lieuwen, T., *Linear Response of Stretch-Affected Premixed Flames to Flow Oscillations.* Combustion and Flame, 2009. **156**(4): p. 889-895.
[59] Jiang, G. and Peng, D., *Weighted Eno Schemes for Hamilton-Jacobi Equations.* SIAM Journal on Scientific Computing, 2000. **21**(6): p. 2126-2143.
[60] Gottlieb, S. and Shu, C., *Total Variation Diminishing Runge-Kutta Schemes.* Mathematics of Computation, 1998. **67**(221): p. 73-85.